~~Explicit~~Process-level simulation of chemical composition, size distribution and cloud condensation nuclei of secondary organic aerosol from α-pinene ozonolysis

Zhen Song[1,2,3,4], Chenqi Zhang[1], Hongru Shen[1,†], Hao Ma[1], Iida Pullinen[6,‡], Defeng Zhao[1,3,4,5]

[1]Department of Atmospheric and Oceanic Sciences & Institute of Atmospheric Sciences, Fudan University, Shanghai, China

[2]Shanghai Frontiers Science Center of Atmosphere-Ocean Interaction, Fudan University, Shanghai, 200438, China

[3]Shanghai Key Laboratory of Ocean-land-atmosphere Boundary Dynamics and Climate Change, Fudan University, Shanghai, 200438, China

[4]National Observations and Research Station for Wetland Ecosystems of the Yangtze Estuary, Fudan University, Shanghai, 200438, China

[5]Institute of Eco-Chongming (IEC), 1050 Baozhen, Lühua Town, Chongming District, Shanghai 202151, China

[6]Institute of Energy and Climate Research, IEK-8: Troposphere, Forschungszentrum Jülich, Jülich, Germany

[†]Present address: Department of Chemical Engineering and Applied Chemistry/Department of Chemistry, University of Toronto, Toronto, Ontario M5S 3E5, Canada

[‡] Present address: Department of Applied Physics, University of Eastern Finland, Kuopio, 70210, Finland

Correspondence to: Defeng Zhao (dfzhao@fudan.edu.cn)

Abstract. Secondary organic aerosols (SOA) contribute significantly to cloud condensation nuclei (CCN), which depend on particle size distribution~~, (PSD),~~ chemical composition and the hygroscopicity parameter (κ). ~~However, how well current understanding of~~Simulating SOA ~~formation can reproduce~~ and CCN ~~concentrations and the influence these factors on modelled CCN uncertainties are still unclear. In~~in chemical transport models~~, it is difficult~~ relies on parameterizations, which need to ~~address the issue due to model complexity~~ be evaluated and ~~oversimplified representation of chemical mechanisms, particle size and κ.~~improved against process-level models as a benchmark. Here, we ~~explicitly~~ simulated ~~CCN concentrations of~~ SOA ~~from~~concentration, chemical composition, PSD, κ, and CCN in α-pinene ozonolysis, a ~~bench mark~~classical system for SOA studies, using a process-level box model ~~(~~PyCHAM~~). Using state of the art treatment of~~ with near-explicit chemical mechanisms~~, aerosol size and κ, we~~. We assessed how CCN ~~as well as,~~ chemical composition, ~~aerosol size~~PSD and κ can be modelled against ~~measurement~~measurements and evaluated the influence of these factors on CCN simulation. The model well simulated SOA mass concentration but overestimated O:C and H:C ratios, suggesting a possible lack of particle-phase chemistry. Highly oxygenated molecules (HOMs) contributed substantially to SOA mass ~~and thus CCN. Modeled~~. Simulated κ closely ~~aligned~~agreed with measurements at moderate supersaturation (0.37%) but ~~overestimate κ (by 19%)~~was overestimated at low supersaturation ~~(~~(0.19%) and ~~underestimate κ (by 21%)~~underestimated at high supersaturation (0.55% and 0.73%). ~~The model well~~Particle growth and number concentrations were reasonably reproduced ~~particle growth, but exhibited wider~~, though the simulated PSD was broader and flatter ~~size distribution compared with~~than measurement. ~~The simulated~~Simulated CCN concentrations agreed well with ~~measurement~~measurements at moderate to high ~~SS~~supersaturation (0.37–0.73%) but ~~had a significant bias~~were overestimated at low ~~SS.~~supersaturation (0.19%). Sensitivity analysis highlights the importance of ~~accurate representation of~~accurately representing both ~~size distribution~~PSD and κ for reliable CCN prediction, especially at ~~lower SS (<~~supersaturation < 0.4~~%).~~%. This study also highlights that HOM formation, finer PSD resolution and improved κ parameterizations are warranted in future chemical transport models, and evaluates the ability and limitations of this benchmark model.

1 Introduction

Secondary organic aerosol (SOA), formed through the oxidation of volatile organic compounds (VOCs) and gas-particle partitioning, constitutes a significant fraction of atmospheric submicron aerosol mass (Jimenez et al., 2009; Huang et al., 2014; Shrivastava et al., 2017). As a result, SOA contributes significantly to global cloud condensation nuclei (CCN), influencing aerosol indirect effects (aerosol-cloud interaction) and radiative forcing (IPCC, 2021).

Despite numerous research efforts, uncertainties persist in assessing indirect effects of SOA on climate. These uncertainties are closely linked to inaccuracies in simulated CCN number concentrations within chemical transport models (IPCC, 2021). The contribution of SOA to CCN concentrations depends on the SOA concentration (Liu and Wang, 2010; Mei et al., 2013) and CCN activity of SOA, which is determined by their particle size distribution (PSD) and hygroscopicity (Farmer et al., 2015; Seinfeld and Pandis, 2016). Therefore, uncertainties in modeled CCN levels are strongly influenced by these parameters~~, which are often oversimplified in~~ (McFiggans et al., 2006). In current chemical transport models~~. For example, chemical transport models often employ simplified chemical mechanisms, such as CBM (Carbon Bond Mechanism), RACM (Regional Atmospheric Chemistry Mechanism), and SAPRC (Statewide Air Pollution Research Center),~~ to enhance computational efficiency and numerical stability~~. Regarding the size distribution, the sectional approach is widely used to simulate aerosol size distributions (Topping and Bane, 2022). However, limited bin resolution compromises the accuracy of~~, SOA and CCN formation relies on simplified parameterizations which have been developed and optimized based on laboratory measurements or ambient data (Hodzic and Jimenez, 2011). For example, lumped species and reactions are usually adopted for gas-phase chemical mechanisms. Limited aerosol size bin resolution is typically used to represent size distribution and number concentration ~~simulations~~ (Kanakidou et al., 2005; Yu and Luo, 2009; Luo and Yu, 2011~~). Additionally, ~~; Topping and Bane, 2022). The volatility bases set (VBS) and its derivatives are often used to represent chemical composition of SOA via gas-particle partitioning (Donahue et al., 2006). Moreover,~~ the hygroscopicity parameter (κ), derived from Köhler theory (Petters and Kreidenweis, 2007), is ~~often simplified in chemical transport models,~~ parameterized either ~~by assuming~~as a uniform ~~κ~~value for organic aerosols (OA) in most global models (Fanourgakis et al., 2019) or ~~various~~as several constant ~~κ~~values for different OA types ~~of OA~~ in regional models (Wang et al., 2019; Kuang et al., 2020). ~~These~~While these parameterizations or simplifications ~~introduce uncertainties in CCN simulations. However, in chemical transport models, it is difficult to assess the influence of these parameters on the uncertainties of CCN from SOA due to the mixing of SOA with other aerosol components, lack of direct observation constraints on all these parameters and complex factors influencing these parameters. Moreover, even without these simplifications, it is still not clear how well we can~~ provide useful and efficient approaches to model ~~CCN concentration of~~ SOA~~. Therefore, it is imperative~~ composition, concentrations, and CCN concentrations, it is necessary to ~~assess how well current understanding~~evaluate them against process-level models as a benchmark. Such process-level models can provide a mechanistic representation of SOA ~~formation, i.e.,~~chemistry and corresponding CCN formation by incorporating explicit or near-explicit chemical mechanisms ~~can reproduce the~~and physicochemical processes such as detailed chemistry, gas-particle partitioning, fine particle size bin, and explicit treatment of κ. Such models are suitable for simulating SOA ~~size distribution,~~and CCN in chamber or laboratory studies and for developing more detailed bottom-up parameterizations applicable to chemical transport models. Moreover, such models can be used to improve chemical transport models, potentially through training artificial intelligence (AI)-based models capable of learning detailed parameterizations (Xia et al., 2025). In addition, this process-level approach enables the assessment of factors controlling SOA-derived CCN based on explicit chemical composition ~~and κ. Such an assessment can only be achieved by comprehensive modelling of SOA formed in laboratory studies, where SOA precursors and formation conditions are well known and comprehensive measurements of SOA (mass, size distribution and CCN) are available~~(which determines κ) and PSD simulations.

Over the past two decades, based on comprehensive explicit or near-explicit gas-phase chemical mechanisms, numerous studies have modeled SOA formation by oxidation of biogenic VOCs (Jenkin, 2004; Xia et al., 2008; Capouet et al., 2008;

Ceulemans et al., 2010; Chen et al., 2011; Valorso et al., 2011; Zuend and Seinfeld, 2012; Gatzsche et al., 2017; Galeazzo et al., 2021) or anthropogenic VOCs (Johnson et al., 2004, 2005; Hu et al., 2007; Camredon et al., 2007; Kelly et al., 2010; Xu, 2014; La et al., 2016; Lannuque et al., 2023) under different conditions in chamber environment. The MCM (Master Chemical Mechanism), comprising 143 VOCs species and approximately 17,000 reactions, is the most widely used near-explicit mechanism (Jenkin et al., 1997, 2003; Saunders et al., 2003). Similar near-explicit or quasi-explicit chemical mechanisms include CACM (Caltech Atmosphere Chemistry Mechanism) (Griffin et al., 2002), GECKO-A (Generator for Explicit Chemistry and Kinetics of Organics in the Atmosphere) (Aumont et al., 2005; Camredon et al., 2007), PRAM (Peroxy Radical Autoxidation Mechanism) for the production of gas-phase Highly Oxygenated organic Molecules (HOMs) (Roldin et al., 2019), and other diversified VOCs oxidation mechanisms constructed by different studies (Peeters et al., 2001; Capouet et al., 2004, 2008; Hu et al., 2007; Ceulemans et al., 2010). HOMs, a group of VOCsVOC oxidation products formed through rapid autoxidation, play a critical role in SOA formation due to their low volatility and high oxygen content (Ehn et al., 2014; Bianchi et al., 2019). Modeling studies have demonstrated the importance of HOMs in SOA production from α-pinene and Δ^3-carene ozonolysis reactions (Roldin et al., 2019; Xu, 2021; Luo et al., 2024; Thomsen et al., 2024). In the models simulating SOA formation, gas-particle partitioning has been modeled based on thermodynamic absorption equilibrium partitioning theory (Pankow, 1994) or dynamic gas-particle mass transfer following Raoult's lawpartitioning (Seinfeld and Pandis, 2016). Besides gas-phase reaction and gas-particle partitioning, particle-phase reactions, such as oligomerization and polymerization, have also been shown to significantly affect SOA speciationaffect SOA composition in the model simulation, although their importance varies across environmental conditions and reaction systems (Jenkin, 2004; Johnson et al., 2004, 2005; Xu, 2014; Hu et al., 2007; Chen et al., 2011; Galeazzo et al., 2021; Jia and Xu, 2021). For example, Hu; Zhao et al. (2007) demonstrated that up to 70% of SOA mass from toluene photooxidation originated from oligomers and polymers, underscoring the importance of particle-phase chemistry., 2023; Lopez et al., 2025). Additionally, model studies have also indicateddiscussed the importanceinfluence of non-ideality mixing and vapor pressure estimation methods inon SOA simulations (Ceulemans et al., 2010; Kelly et al., 2010; Valorso et al., 2011; Zuend and Seinfeld, 2012).

Despite advancements in chemical mechanisms and gas-particle partitioning models, SOA simulations still have limits.exhibit limitations. Most SOA modeling studies have focusedfocus on SOA mass concentration and SOA yield, whileconcentrations or yields, whereas far fewer studies have simulated the chemical composition, particle size distributionPSD and CCN concentrations (Jenkin, 2004; Johnson et al., 2004, 2005; Hu et al., 2007; Xia et al., 2008; Capouet et al., 2008; Chen et al., 2011; Xu, 2014). In general, the simulation of SOASimulated chemical composition is relatively poorsubstantial discrepancies relative to measurements. For example, the average oxygen-to-carbon ratio (O:C) and hydrogen-to-carbon ratio (H:C) of simulated SOA showed significant gaps compared with measured SOA in different VOCs oxidation reactions (Chen et al., 2011). Roldin et al. (2019) reproduces SOA mass from α-pinene ozonolysis based on reasonable HOM simulation but overestimates H:C, while O:C shows smaller bias at the average level. Pichelstorfer et al. (2024) captures the mass distribution of gas-phase HOMs and the monomer/dimer ratio, and achieves good agreement with SOA yield under low-NO_x conditions, but underestimates SOA formation under high-NO_x conditions. Moreover, few studies have simulated the particle size, which is crucial to SOA physical properties. Jia and Xu (2021) developed the CSVA (Core-Shell box model for Viscosity dependent SOA) model, which simulates SOA size distribution to simulate PSD evolution using a core-shell structure to account forconsidering viscosity effects in the gas particle mass transfer.. O'Meara et al. (2021) developed a pythonthe PyCHAM box model PyCHAM (CHemistry with Aerosol Microphysics in Python) for simulating), which includes aerosol chambers, which microphysics and can also simulate particle size distribution. By using PyCHAM,PSD. Xu (2021) modeled SOA size distribution used PyCHAM to simulate PSD evolution of SOA from α-pinene ozonolysis and showed a good envelope between the simulated and measured particle size evolution, though in the simulation it was shifted to a later position, meaning the , capturing overall growth but with a delayed particle growth peak compared to measurement.

~~Furthermore, up to now, there is still a lack of~~ To date, simulation ~~for~~of SOA hygroscopicity ~~of SOA~~ and CCN number ~~concentration based on~~ concentrations using near-explicit chemical mechanisms remain limited.

In this study, we simulated ~~mass~~the concentration~~,~~ and chemical composition~~, size distribution and CCN concentrations~~ of SOA formed ~~in~~from α-pinene ozonolysis, a ~~bench-mark~~benchmark system in SOA studies, and CCN concentrations using PyCHAM~~. We integrated MCM and PRAM mechanisms and consider gas particle partitioning, gas wall partitioning, nucleation, coagulation, and particle wall loss to investigate SOA formation and growth.~~ model. Simulated SOA mass, number ~~concentration~~concentrations, chemical composition, size distribution, κ, and CCN number ~~concentration are compared with measurement.~~concentrations were evaluated against measurements. We further investigated the impact of SOA κ and PSD representation on CCN. This ~~analysis~~study aims to ~~identify key chemical processes influencing~~evaluate the capability and limitations of process-level modeling of SOA ~~mass and~~ concentrations, chemical composition, PSD, and CCN using a bottom-up approach as a potential benchmark model. In the future, once validated and improved such a benchmark model for SOA and ~~highlights the importance of accurate~~CCN simulation ~~of κ and particle size distribution in CCN simulations~~can be used for assessing SOA and CCN parameterizations in chemical transport models and may be used to improve chemical transport models, potentially through training AI-based models capable of learning detailed parameterizations.

2 Methods

2.1 SAPHIR ~~Chamber~~chamber and ~~Experiment~~experiment

The α-pinene ozonolysis experiment was conducted in the SAPHIR (Simulation of Atmospheric PHotochemistry In a large Reaction) chamber at Forschungszentrum Jülich, Germany. SAPHIR is a 270 m^3 double-walled cylindrical Teflon chamber with a surface-to-volume ratio of ~1 m^2 m^{-3}, as previously described (Rohrer et al., 2005; Zhao et al., 2015a, b). The chamber utilizes natural sunlight for illumination and features a louvre system to switch between light and dark conditions. For this study, the experiment was performed in the dark with the louvres closed. Prior to the experiment, the chamber was flushed with high-purity synthetic air (purity > 99.9999% O_2 and N_2). The experiment was conducted at a relative humidity (RH) of 37–79% and a temperature range of 291.2–299.1 K (Fig. S1). A total of 20 ppbv of α-pinene was introduced into the chamber, followed by the addition of 50 ppbv O_3 after 30 ~~minutes~~min to initiate organic chemistry. The experiment lasted approximately 8.5 ~~hours~~h, and no seed aerosols were used.

Temperature and RH were monitored continuously throughout the experiment. A ~~Scanning Mobility Particle Sizer~~scanning mobility particle sizer (SMPS~~) coupled with a Condensation Particle Counter (CPC, TSI3785, TSI DMA3081/TSI CPC3785~~) measured SOA mass and number concentrations and size distributions~~.~~ over the range 9.82–429.4 nm. A ~~Cloud Condensation Nuclei Counter (CCNc~~cloud condensation nuclei counter (CCN100, Droplet Measurement Technique, USA) measured CCN number concentrations at four supersaturations (SS): 0.19%, 0.37%, 0.55%, and 0.73%. ~~The SS calibration and κ parameter calculations followed Zhang et al. (2023). An Aerosol Mass Spectrometer (AMS~~Based on parallel measurements of CCN and total particle number (cloud nuclei; CN) for each size bin in a continuous flow, the critical activation particle size (D_{crit}) at each SS was determined using the Scanning Mobility CCN Analysis (SMCA) method (Moore et al., 2010; Zhao et al., 2015a, 2016). Briefly, CN and CCN concentrations for each size bin were used to calculate the CCN activation fraction (CCN/CN). Before computing CCN/CN, the measured CCN and CN concentrations were corrected for multiple charged particles. Then, CCN/CN for each charge class was then fitted using a Gaussian error function, and the turning point of this function was taken as D_{crit} at the specific SS. For each SS, at least three full scans were performed, and the resulting D_{crit} were averaged. The SS calibration followed Zhao et al. (2016) and Zhang et al. (2023). Then κ parameter at four SS was derived from κ–Köhler equation given different SS and corresponding D_{crit} (Petters and Kreidenweis, 2007). The error bars for κ were estimated from the standard deviation of D_{crit} across three duplicate scans. A high-resolution time-of-flight aerosol mass spectrometer (HR-ToF-AMS, Aerodyne Research Inc., DeCarlo et al., 2006) provided SOA chemical

composition data, including O:C and H:C elemental ratios. O_3 concentrations were measured using a UV photometer O_3 analyzer (ANSYCO, model O341M). OH, HO_2, and RO_2 radical concentrations were quantified using a home-built laser-induced fluorescence system (LIF) (Fuchs et al., 2012). VOCs were ~~characterized~~measured using a ~~Proton Transfer Reaction Time~~proton transfer reaction time-of-~~Flight Mass Spectrometer~~flight mass spectrometer (PTR-ToF-MS, Ionicon Analytik, Austria). Gas-phase oxygenated ~~products from α-pinene ozonolysis~~organic molecules (OOMs) participating in gas-particle partitioning, including HOMs, were ~~analyzed~~measured using a ~~Chemical Ionization Atmospheric Pressure Interface Time~~chemical ionization atmospheric pressure interface time-of-~~Flight Mass Spectrometer~~flight mass spectrometer (CIMS, Tofwerk AG/Aerodyne Research, Inc.) with nitrate (NO_3^-) as the reagent ion (NO_3^--CIMS).

2.2 PyCHAM ~~Box Modeling~~box modeling

The α-pinene ozonolysis experiment was simulated using the PyCHAM (CHemistry with Aerosol Microphysics in Python) model (v5.5.9) (O'Meara et al., 2021). PyCHAM was developed with two precursor models as platforms: the Microphysical Aerosol Numerical model Incorporating Chemistry (MANIC) for multiphase processes (Lowe et al., 2009) and PyBox for Python-based parsing and automatic generation of chemical reaction modules (Topping et al., 2018). PyCHAM is designed to simulate aerosol chamber experiments, enabling comparisons between simulations and observations to improve process understanding for atmospheric applications.

PyCHAM solves coupled ordinary differential equations for gas-phase chemistry, gas-particle partitioning, and gas-wall partitioning following Jacobson (2005). Gas–particle partitioning follows the formulation of Zaveri et al. (2008):

$$\frac{dC_{i,g}}{dt} = -\sum_{j=1}^{N} k_{i,j}\left(C_{i,g} - x_{i,j}p_i^0 K_{v,j}\gamma_{i,j}\right), \quad (1)$$

$$\frac{dC_{i,j}}{dt} = k_{i,j}\left(C_{i,g} - x_{i,j}p_i^0 K_{v,j}\gamma_i\right), \quad (2)$$

where component i partitions into size bin j from the gas phase g, with N total size bins. Here, x is the particle-phase mole fraction, p^0 is the pure component liquid (sub-cooled if necessary) vapour pressure, K_v is the Kelvin factor and γ is the activity coefficient. Because no well-established data of γ were available for our experimental conditions, we only simulated the idealized conditions (i.e. γ for all components were set to 1). The first-order mass transfer coefficient $k_{i,j}$ for component i to size bin j incorporates the Fuchs-Sutugin transition regime correction (Fuchs and Sutugin, 1971) and can be adjusted based on ~~γ and~~mass accommodation coefficient (α_i) of individual component~~.~~:

$$k_{i,j} = 4\pi\overline{R_{p,j}}D_{g,i}N_j f\left(Kn_{i,j},\alpha_i\right), \quad (3)$$

where $\overline{R_{p,j}}$ (cm) is mean wet radius of particles in bin j; $D_{g,i}$ (cm^2 s^{-1}) is gas diffusivity of species i; N_j (cm^{-3}) is the number concentration of particles in bin j; α_i means the chance that component i can stick to a particle surface when collision happens. In our simulation, α_i for all components were set to 1. And $f(Kn_{i,j}, \alpha_i)$ is the transition regime correction factor to the Maxwellian flux as a function of the Knudsen Number:

$$f\left(Kn_{i,j},\alpha_i\right) = \frac{0.75\alpha_i\left(1+Kn_{i,j}\right)}{Kn_{i,j}\left(1+Kn_{i,j}\right)+0.283\alpha_i Kn_{i,j}+0.75\alpha_i}, \quad (4)$$

$$Kn_{i,j} = \frac{\lambda_i}{\overline{R_{p,j}}}, \quad (5)$$

where λ_i is the mean free path.

Gas–wall partitioning follows an analogous framework:

$$\frac{dC_{i,g}}{dt} = -k_w\left(C_{i,g} - \frac{C_{i,w}}{C_w}p_i^0\gamma_i\right), \quad (~~3~~6)$$

$$\frac{dC_{i,w}}{dt} = k_w\left(C_{i,g} - \frac{C_{i,w}}{C_w}p_i^0\gamma_i\right), \quad (~~4~~7)$$

where p_i^0 is the liquid (sub-cooled if necessary) saturation vapour pressure of component i and γ_i is its activity coefficient on the wall. k_w (s^{-1}) accounts for gas- and wall-phase diffusion, turbulence, accommodation coefficient, and chamber surface-area-to-volume ratio. k_w was set to 2.2×10^{-3} s^{-1} according to experimental measurement (Guo et al., 2022). Meanwhile, C_w (g

m^{-3}) represents wall adsorption/absorption properties, including effects of RH, surface area, diffusivity, and porosity. ~~We conducted a sensitivity analysis of SOA mass concentration to a series of C_w values (Fig. S2), and SOA mass concentration showed no apparent change when C_w increased by one magnitude from 1×10^{-7} to 1×10^{-6} g m^{-3}. Therefore, C_w was set to 1×10^{-6} g m^{-3}~~Neglecting the gas-wall partitioning of organic compounds in Teflon film chambers in the model can lead to a systematic overestimation of the yields of gaseous products and SOA (Matsunaga and Ziemann, 2010; Zhang et al., 2014). Therefore, we conducted a sensitivity analysis of SOA mass concentration by testing several different orders of magnitude for the C_w value (Fig. S2). When C_w = 0, the simulated SOA mass concentration was still underestimated, which indicated that the source of SOA mass was underestimated in current model setup. The result for $C_w = 1\times10^{-10}$ g m^{-3} was nearly identical to that for C_w = 0. However, to reflect the physical relevance of wall absorption in chamber studies, we used $C_w = 1\times10^{-6}$ g m^{-3} in our simulations, and the simulated SOA mass was reasonably reproduced. Increasing C_w by one order of magnitude to 1×10^{-5} g m^{-3} resulted in a larger deviation in SOA mass concentration, whereas decreasing it by one order of magnitude to 1×10^{-7} g m^{-3} led to only minimal changes in SOA mass concentration. Consequently, $C_w = 1\times10^{-6}$ g m^{-3} was finally selected for this study.

PyCHAM also simulates microphysical processes, including coagulation, nucleation, and particle wall loss, which influence particle number evolution. Using a semi-implicit equation, coagulation process accounts for Brownian diffusion, convective Brownian diffusion enhancement, gravitational collection, turbulent inertial motion, turbulent shear, and Vander Waals collisions (Jacobson, 2005), without adjustable parameters.

Nucleation is modeled using a tuned Gompertz function to fit measured particle number ~~size distributions~~concentrations during the initial reaction phase, without inferring mechanistic details:

$$P_1(t) = nuc_{v1}\left(\exp\left(nuc_{v2}\left(\exp\left(-\frac{t}{nuc_{v3}}\right)\right)\right)\right), \quad (~~5~~8)$$

where P_1 (no. cm^{-3}) is the number concentration of new particles after time t that enter the smallest size bin, and nuc_{vn} represents the user-defined parameters which allow the amplitude (nuc_{v1}), onset (nuc_{v2}) and duration (nuc_{v3}) of the curve to be adjusted. Note that Eq. (~~5~~8) is independent of chemistry. In this study, particle number concentrations were firstly fitted to CPC measurements during the initial 0.57 ~~hours~~h by setting nuc_{vn} (nuc_{v1} = 22403, nuc_{v2} = -17.66, nuc_{v3} = 317.88). Particle size range of formed SOA was set as ~~0~~ 1.8-500 nm, and the radius of newly nucleated particles was set as 10.9 nm according to lower limit of the size range of SMPS. PyCHAM employs a sectional approach, dividing particles into a number of size bins ~~(set as 128 in this study)~~ and simulating size ~~changes~~evolution using the moving-center or full-moving approaches (Jacobson, 2005~~); the latter was~~). As recommended by O'Meara et al. (2021) that a more detailed 128 size bins should be adopted ~~in this study~~when the number PSD is important, we set the bin number to 128 and employed the full-moving approach to simulate size evolution. In this way, the constrained and subsequently simulated number concentrations excluding coagulation agree well with CPC measurements (R^2 = 0.89; NMB = 0.29%; Fig. S3~~), nevertheless~~). However, the ~~particle size distribution simulation~~PSD during the early nucleation stage cannot be set in nucleation scheme, and the PSD deviates significantly from ~~measurement~~measurements (Fig. S4).

~~Therefore, to accurately simulate~~Because the accuracy of CCN ~~which~~number concentration depends on both ~~particle number and~~ the SOA size distribution and κ, any bias in the PSD directly affects the CCN simulation. To improve the representation of early growth, nucleation scheme was not used and the ~~particle~~initial number ~~size distribution~~PSD was instead constrained using ~~the particle size distribution measured by~~ SMPS measurement during the initial 0.6 ~~hours in the model~~h assuming the species $C_{20}H_{30}O_{17}$ to represent low-volatile HOMs dimers as seed particle. The vapor pressure of $C_{20}H_{30}O_{17}$ at normal temperature calculated by default method of Nannoolal et al. (2008) is 2.14×10^{-29} Pa, which is extremely low to act as a seed aerosol. The lower and upper boundaries and mean radii of each size ~~bins~~bin and bin number were ~~constrained~~set according to SMPS ~~measurements~~ (9.~~6-437.2~~82-429.4 nm~~) and~~ size ~~bin number was~~range and 106~~.~~ size bins). Under this configuration, the PSD performed better than that of nucleation scheme (Fig. S5). However, the simulated SOA mass concentration and chemical composition were significantly influenced by the presence of assumed seed particles~~.~~, increasing

the discrepancy with measurements (Fig. S6). Therefore, to balance the simulation of chemical composition and ~~particle size~~PSD, the ~~simulation of~~ SOA mass concentration and chemical composition ~~are based on~~were simulated using the ~~scheme of~~ nucleation~~, as in~~ scheme (Sect. 3.1~~. While as for~~). In contrast, the particle number concentration and ~~size distribution, the simulation adopts the scheme of constraining~~ PSD were simulated using the SMPS ~~size distribution and number concentration of~~ constrained approach (hereafter referred to as the seed ~~particles together, as in~~scheme; Sect. 3.2~~.~~). Subsequently, the κ ~~is~~values derived from the SOA chemical composition ~~of SOA displayed~~ in Sect. 3.1~~. This was~~ were combined with the ~~particle size distribution described~~PSD obtained in Sect. 3.2 to calculate CCN number concentrations~~, as in~~ (Sect. 3.3). The influence of individual schemes (nucleation or seed) on CCN predictions are in Sect. 3.4.

Particle wall deposition is simulated using either the McMurry and Rader (1985) model or a customized size-dependent deposition rate:

$$D_{\mathrm{p}} < D_{\mathrm{p,flec}}$$

$$\log_{10}\left(\beta(D_{\mathrm{p}})\right) = \log_{10}(D_{\mathrm{p,flec}}) - \log_{10}(D_{\mathrm{p}})\,\nabla_{\mathrm{pre}} + \beta_{\mathrm{flec}}, \quad (6)$$

$$D_{\mathrm{p}} \geq D_{\mathrm{p,flec}}$$

$$\log_{10}\left(\beta(D_{\mathrm{p}})\right) = \log_{10}(D_{\mathrm{p}}) - \log_{10}(D_{\mathrm{p,flec}})\,\nabla_{\mathrm{pro}} + \beta_{\mathrm{flec}}, \quad (7)$$

where $D_{p,flec}$ marks the inflection diameter for deposition rates, and β_{flec} gives the deposition rate (s^{-1}) at this inflection point. ∇_{pre} and ∇_{pro} represent the log-log slopes of deposition rate versus diameter before and after the inflection point. ~~This~~As the PSD size range varied by only a factor of ~2 during the period when it was not constrained by SMPS measurements, and no obvious deviation in peak diameter was observed within ~1 h after the experiment ended, this study used a uniformed value (β_{flec} = 2.37×10^{-5} s^{-1}) based on the measured particle loss rates without considering the size dependence.

Moreover, other parameters such as time series of temperature (291.2–299.1 K) and RH (37–79%), and dilution rate (9×10^{-6} s^{-1}) during the experiment were constrained according to measurements.

The gas-phase chemical mechanism for α-pinene we used in PyCHAM draw upon previous studies as MCM coupled with PRAM mechanisms (Roldin et al., 2019; O'Meara et al., 2021; Luo et al., 2024; Thomsen et al., 2024). PyCHAM currently lacks explicit treatment of particle-phase reactions and dissolution, which are hence not considered in our simulation. The simulated α-pinene concentrations agree with ~~measurement~~measurements (R^2 = 0.99) in this study (Fig. ~~S5),~~S7), and the temporal trends of gas-phase products HOMs (Fig. S8) are well captured, though there are some biases in the absolute concentrations, indicating the capability to describe gas-phase chemistry of α-pinene ozonolysis by PyCHAM with MCM ~~+ PRAM mechanism~~and PRAM mechanisms. The detailed chemical species formulas produced by MCM and PRAM mechanisms are shown in Table S1. And the input files including model variables setting and chemical mechanism files used in PyCHAM are supplied in Sect. Data availability.

2.3 Hygroscopicity ~~Parameter~~parameter (κ) and CCN ~~Concentration~~concentration

The hygroscopicity parameter (κ) of bulk SOA was calculated using the UManSysProp module (Topping et al., 2016), an open-source tool for predicting molecular and atmospheric aerosol properties ~~(https://github.com/loftytopping/UManSysProp_public/).~~. UManSysProp estimates pure component vapor pressures, critical properties, sub-cooled densities of organic molecules; activity coefficients for mixed inorganic-organic liquid systems; hygroscopic growth factors and CCN activation potential of mixed inorganic–organic aerosol particles with associated κ–Köhler values (Kreidenweis et al., 2005); and absorptive partitioning calculations with/without a treatment of non-ideality. Users input molecular information as SMILES (Simplified Molecular Input Line Entry System) strings, and UManSysProp automatically extracts relevant information for calculations.

In PyCHAM, UManSysProp predicts molecular weight, pure liquid density, and liquid saturation vapor pressure for individual components. Default methods include Girolami (1994) for liquid density and Nannoolal et al. (2008) for vapor

pressure estimation. Since PyCHAM does not currently include κ prediction, we further calculated the κ values for bulk SOA under ideal condition given molar concentrations, vapor pressures, densities, temperatures, dry particle sizes, and a surface tension of 72 mN m^{-1}. The critical activated dry particle size ($D_{p,dry}$) for CCN activation at different SS levels was derived from the κ–Köhler equation (Petters and Kreidenweis, 2007):

$$\frac{\mathrm{RH}}{100} = \frac{{D_{\mathrm{p,\,wet}}}^3 - {D_{\mathrm{p,\,dry}}}^3}{{D_{\mathrm{p,\,wet}}}^3 - (1-\kappa){D_{\mathrm{p,\,dry}}}^3} \exp\left(\frac{4\sigma_s M_w}{RT\rho_w D_{\mathrm{p,\,wet}}}\right), \quad (8\text{11})$$

where σ_s is the surface tension of the wet particle at the solution-air interface, M_w is the molecular weight of water, R is the ideal gas constant, T is temperature, ρ_w is the density of water, and $D_{p,wet}$ is the diameter of the wet particle.

Particles larger than $D_{p,dry}$ can act as CCN and $D_{p,dry}$ decreases with increasing SS. Then CCN number concentrations at different SS ($N_{CCN,SS}$) were calculated by integrating the simulated particle number size distribution *PNSD(D)* over size bins exceeding $D_{p,dry}$:

$$N_{CCN,SS} = \int_{D_{p,dry}}^{D_{max}} PNSD(D)dD, \quad (9\text{12})$$

where D is dry particle diameter, and D_{max} is the maximum D.

3 Results and ~~Discussion~~discussion

3.1 Simulation of ~~Particle Formation~~particle formation and ~~Chemical Composition~~chemical composition

Figure 1 shows the simulated and measured SOA mass concentrations. The simulated SOA mass concentration exhibited a high correlation (R^2 = 0.97) with measurements and the two showed similar temporal trends, characterized by a rapid increase within the first ~3 ~~hours~~h followed by a gradual decline. The simulated decline rate closely matched measurements (Fig. 1b), except for a faster decrease around ~6 ~~hours~~h. This discrepancy is likely ~~attribute~~attributed to a rapid temperature increase during this period (Fig. S1), as elevated temperature can cause organic compounds to evaporate from the particle phase, reducing SOA formation (Donahue et al., 2006; Xia et al., 2008; Ceulemans et al., 2010). Simulated particle-phase HOMs accounted for ~43% of total SOA mass concentration (Fig. 1a), highlighting the important contribution of HOMs to SOA and necessity of including ~~HOMs~~HOM formation in the chemical mechanisms as done here by coupling MCM with the PRAM mechanism. Without PRAM mechanism, the onset of SOA growth was significantly delayed and mass concentration was obviously lower. The significant contribution of HOMs to SOA is consistent with previous studies. For example, Roldin et al. (2019) found ~50% of SOA mass from α-pinene ozonolysis with ammonium sulfate seeds ~~originated~~originates from ~~HOMs~~HOM condensation. Gatzsche et al. (2017) reported HOMs ~~contributed~~contribute up to 65% of SOA mass during early-stage α-pinene ozonolysis and ~~accounted~~account for about 27% of the total SOA mass throughout the simulation.

Despite good correlation with measured SOA concentration, simulated SOA mass concentration was consistently underestimated (19.1% ± 10.4%). The underestimation can be attributed to incomplete description of gas-phase chemistry, gas-particle partitioning, and/or particle-phase chemistry. The gas-phase chemistry ~~such as~~, including the loss of α-pinene ~~losses~~ (Fig. ~~S5~~S7) and ~~HOMs~~the composition ~~are well~~of HOMs, is generally ~~simulated~~ well reproduced (Fig. ~~S6), showing~~ S9). The model reproduces the bimodal ~~distribution~~distributions of HOM monomers (m/z 230~~–~~-380) and dimers (m/z 400~~–~~-550~~).~~), although the concentration of monomers is underestimated, especially below m/z 300. It also reasonably captures the fractions of HOM monomers and dimers (Fig. S10), while showing a slight underestimation of dimers in the simulation. This also indicates the capability of PRAM mechanism to effectively ~~characterize~~describe gas-phase ~~HOMs~~HOM formation, as shown by Roldin et al. (2019).

The gas-particle partitioning ~~mass transfer~~ in the model, which can be adjusted by activity coefficient ~~in the model~~(γ), also influences SOA mass concentration. ~~PyCHAM allows adjustment of activity and accommodation coefficients~~The impact of non-ideal behavior on simulated gas-particle partitioning of SOA has been explored in previous studies (Zuend and Seinfeld, 2012; Lannuque et al., 2023). For example, Zuend and Seinfeld (2012) improved the accuracy of simulated mass and

composition of SOA formed from α-pinene ozonolysis by accounting for non-ideal mixing and liquid–liquid phase separation through the calculation of γ for components in the liquid mixture using AIOMFAC (Aerosol Inorganic-Organic Mixtures Functional groups Activity Coefficients). Lannuque et al. (2023) also accounted for non-ideality (i.e., interactions between organic molecules and inorganic ions in the aqueous phase) in their simulation of SOA gas-particle partitioning. They found that considering only ideal partitioning leads to ~~modify this parameter~~a substantial underestimation of SOA formation, particularly in the absence of a pre-existing organic phase. As no well-established data of γ were available for our experimental conditions, we only simulated the idealized conditions. Non-ideality was neglected, and γ for all species were set to 1. As shown in Equation (2), lower γ (corresponding to higher solubility) would lead to higher SOA concentrations and thus reduce the gap between simulated and measured SOA mass concentrations. However, the simulated SOA mass concentration rise rate closely matched measurements (Fig. 1b), indicating ~~that~~ the ~~mass transfer coefficient adequately represents~~appropriate representation of gas-particle partitioning. Therefore, the underestimation of SOA mass is ~~likely~~possibly attributed to missing particle-phase chemistry.

Particle-phase accretion reactions or oligomerization processes can produce larger, higher-molecular-weight species, increasing SOA mass concentration (Pun and Seigneur, 2007; Kroll and Seinfeld, 2008; Hallquist et al., 2009). The influence of particle-phase reaction on SOA mass concentration has been reported in previous studies. For example, Hu et al. (2007) attributed up to 70% of SOA mass to oligomers and polymers in toluene photooxidation, highlighting the importance of particle-phase reactions. By adjusting branching ratio for ~~HOMs~~HOM formation and gas-wall partitioning parameters, Xu (2021) performed a good consistency between simulated and measured SOA mass concentrations from α-pinene ozonolysis. However, the simulated SOA mass concentration ~~was~~is still underestimated from their data even after considering OH-initiated secondary autoxidation, which might be due to the lack of particle-phase reactions in their simulation. Particle-phase reactions, including heterogeneous reactions on aerosol surfaces and in particles of organic compounds, can also alter SOA properties, such as solubility, viscosity, hygroscopicity, and optical properties (Farmer et al., 2015; Shrivastava et al., 2017; Jia and Xu, 2021). For example, Galeazzo et al. (2021) found that missing autoxidation and particle-phase reactions in α-pinene ozonolysis simulations ~~led~~leads to underestimated SOA viscosity.

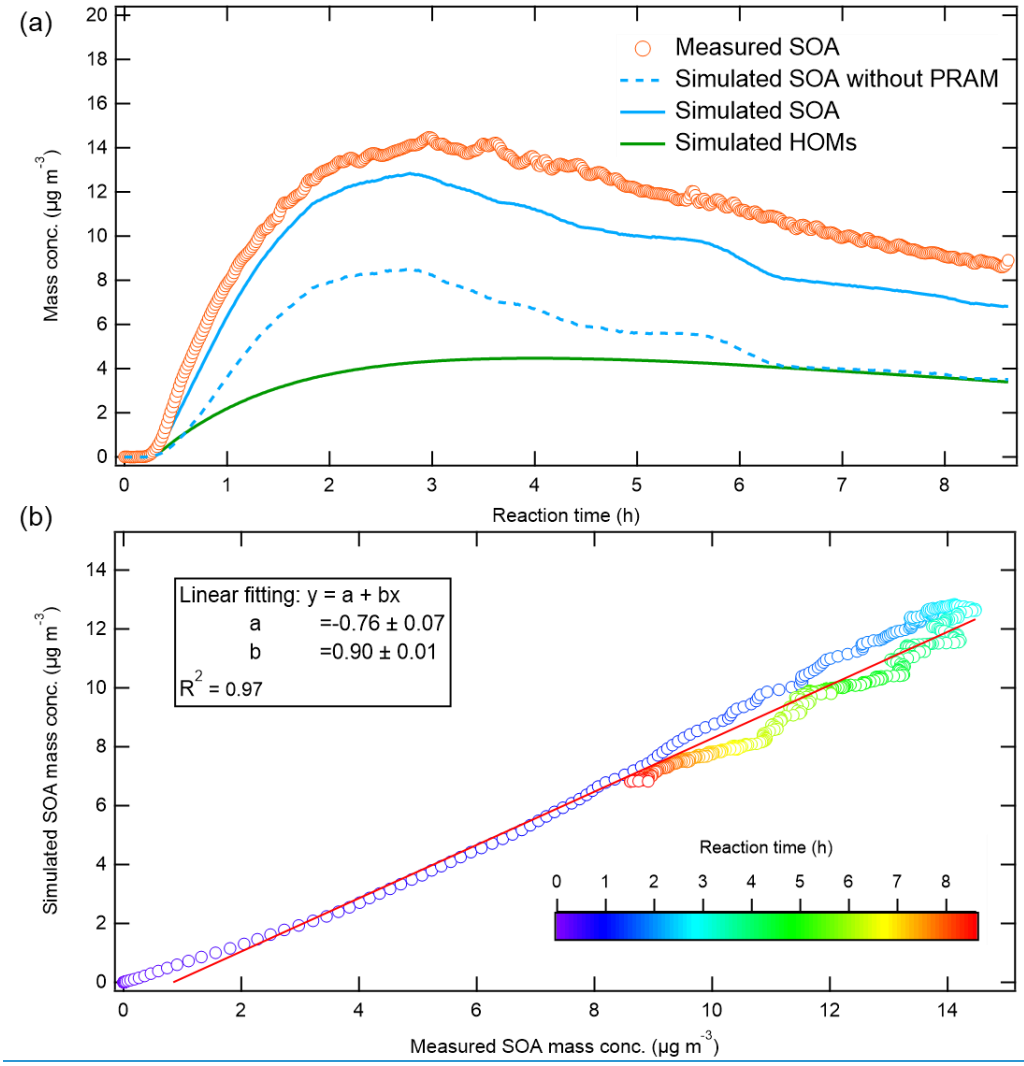

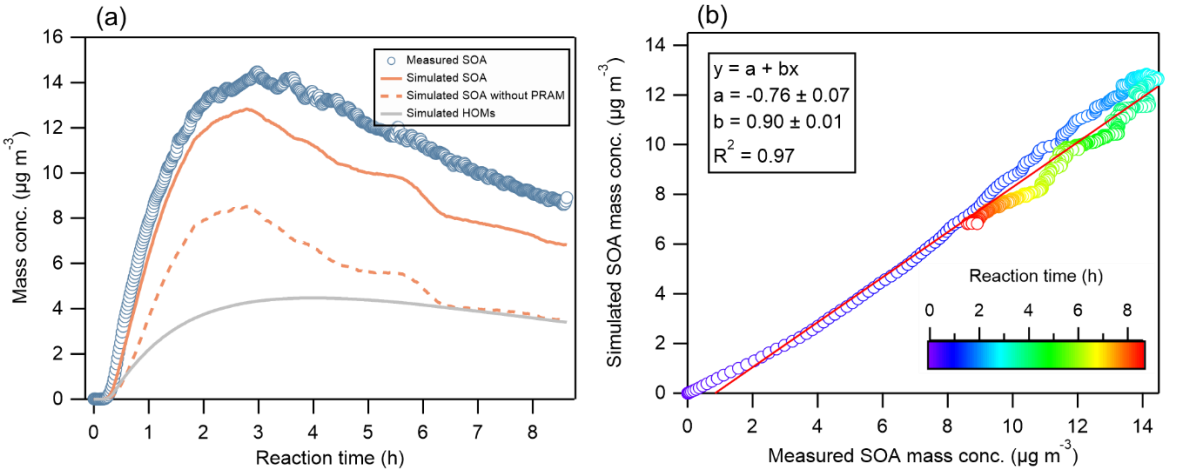

Figure 1: (a) Mass concentrations (µg m^{-3}) of simulated ~~(blue line)~~ and measured ~~(circles)~~ SOA, ~~alongside~~together with the simulated particle-phase HOMs mass concentration ~~(green line).~~. The ~~blue~~ dashed line refers to the simulated SOA ~~without considering~~ excluding the PRAM mechanism. (b) ~~Scatter plot~~Scatterplot of measured versus simulated SOA mass concentrations, with a linear regression fit (red line). The coefficients a and b ~~represent~~denote the intercept and slope, respectively, and R^2 ~~denotes~~is the correlation coefficient. Colors indicate the reaction time ~~of~~during the experiment.

Simulated O:C and H:C ratios of SOA were compared with measurements as AMS can only provide bulk O:C and H:C ratios of SOA rather than molecular chemical composition (Fig. 2). Compared to measured O:C (0.44 ± 0.03) and H:C (1.35 ± 0.02) ratios, the simulated average O:C (0.58 ± 0.03) and H:C (1.64 ± 0.00) ratios were overestimated. Without PRAM mechanism, the simulation showed lower O:C and higher H:C as a result of ~~less~~lacking gas-phase ~~HOMs~~HOM formation, while still overestimating the two ratios. ~~Overestimation~~ Figure S11 illustrates that the simulated O:C of gas-phase HOMs in

the first 10 min of reaction is consistent with measurements, while the H:C is moderately overestimated. These results imply that inaccuracies in the simulated gas-phase chemistry may contribute to the overestimation (21.2% ~~± 2~~ ± 2.1%) ~~and O:C~~ of the H:C in SOA, but exert only a minor influence on the O:C in SOA. The overestimation (32.4% ± 2.2%) ~~ratios~~of O:C is ~~likely~~possibly attributed to the absence of particle-phase reactions in our simulations as mentioned above, emphasizing the importance of particle-phase chemistry in determining SOA chemical composition. The difference between modelled and measured O:C and H:C has also been reported by previous studies. Using similar gas-phase chemical mechanism, Roldin et al. (2019) reported similar overestimations in modelled H:C ratios, while modelled O:C ratios agree with measurements at the average level in their studies. Chen et al. (2011) observed overestimated O:C and H:C ratios in α-pinene ozonolysis simulations. However, HOMs are not included in the mechanism of their study. They proposed a chemical mechanism involving particle-phase decomposition of organic hydroperoxides and subsequent oligomerization involving free radicals to explain the discrepancies. Although HOMs formation was included in our study, the lack of similar particle-phase reactions can still contribute the ~~overestimation~~discrepancies of H:C and O:C ratios.

Regarding the temporal changes, both the measured and simulated average O:C increased gradually over time before stabilizing, which is possibly attributed to the dilution of SOA concentration and/or the increasing fraction of particle-phase HOMs during the experiment (Fig. ~~S7~~S12). In contrast, the measured H:C decreased over time, while the simulated H:C showed no apparent variations. ~~Particle~~Oxidation of particle-phase ~~reactions, such as oligomerization,~~organics by atmospheric oxidants typically ~~generate high molecular weight compound and alter~~ leads to an increase in O:C ~~and H:C ratios~~ of organic matter by functionalization introducing oxygen-containing functional groups like -OH, -COOH, -ONO_2, -OOH, or leads to a decrease in O:C by fragmentation i.e. C-C bond breaking or peroxide photolysis (Kroll and Seinfeld, 2008; Hallquist et al., 2009), and their absence in simulations ~~likely contributed~~possibly contributes to the discrepancy between modelled and measured time series of O:C and corresponding H:C ratios.

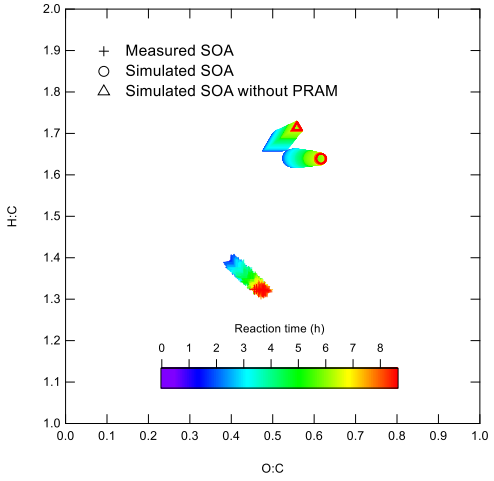

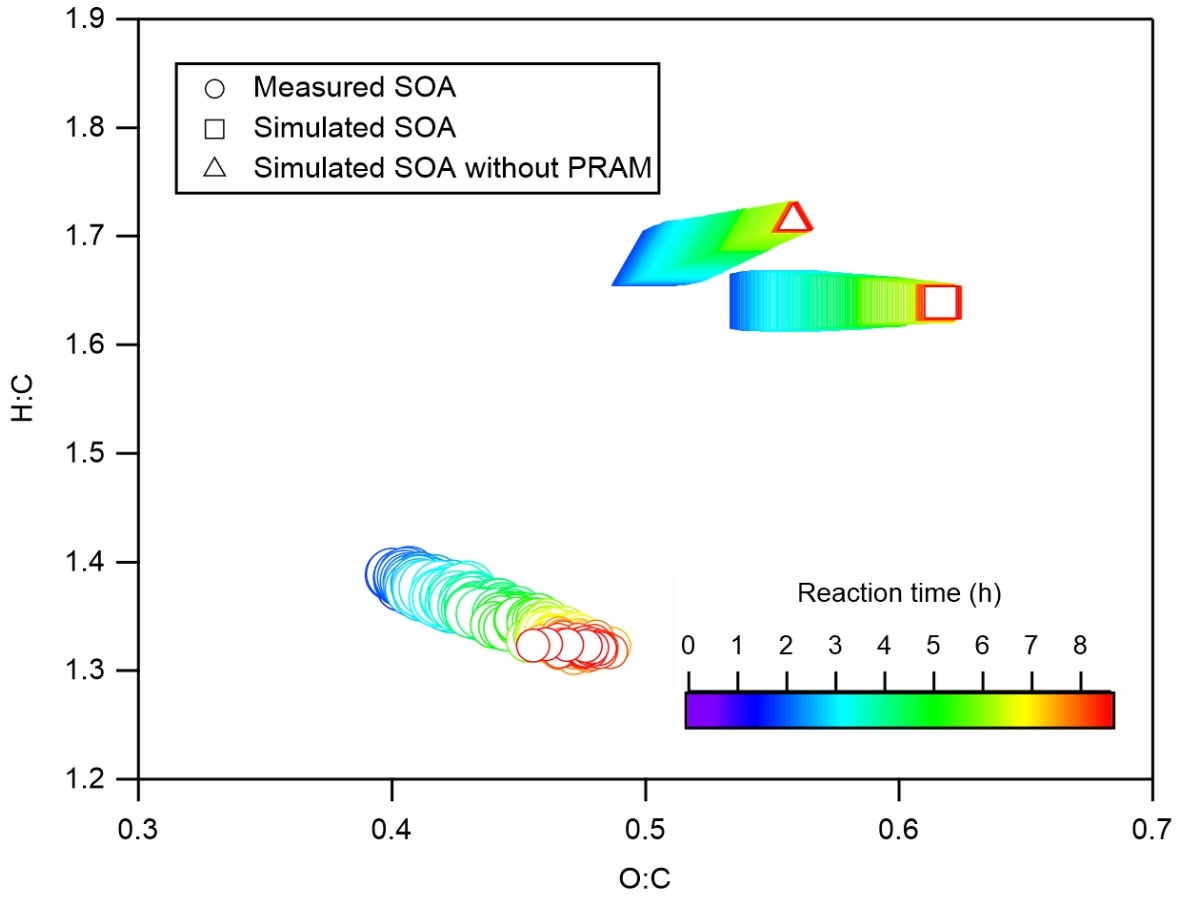

Figure 2: Chemical composition ~~represented by the~~ expressed as average O:C and H:C ratios ~~of~~for simulated (~~circles~~squares) and measured (~~crosses~~circles) SOA, ~~as well as~~along with simulated SOA ~~without considering~~ excluding the PRAM mechanism (triangles). ~~The symbol~~Symbol sizes ~~refer to~~indicate SOA mass concentrations. Valid SOA ~~measurement data~~measurements were available ~~from~~only after 0.45 ~~hours~~h due to ~~the~~ low SOA concentrations ~~before~~prior to that time.

3.2 Simulation of ~~Particle Number Concentrations~~particle number concentrations and ~~Size Distribution~~size distribution

Despite a slight underestimation (7.3% ± 2.8%) of the simulated number concentration ~~since~~as the model run freely following the constrained particle number size distribution ~~(an intercept of ~1657 # cm^{-3}),~~, the simulated particle number concentration showed good agreement with measurements (Fig. 3), with a linear fit yielding a slope of 1.04 and a correlation coefficient of R^2 = 0.99. Our result is similar to the report of Xu (2021) which also ~~exhibited~~exhibits an underestimation of particle number concentration when coagulation ~~was~~is included.

Particle number concentration is primarily influenced by microphysical processes such as nucleation, coagulation, and particle wall loss~~, and gas particle partitioning.~~. In our simulation for particle number, the initial phase of particle growth was constrained by ~~particle size distribution~~PSD of SMPS measurement instead of setting nucleation parameters, as detailed in Sect. 2.2. Besides, particle loss rate to wall was fully constrained by measurements~~, and gas particle partitioning showed good performance in simulated SOA mass concentration.~~. To explore the impact of coagulation on particle number concentration ~~and size distribution~~, we tested ~~including and~~ excluding coagulation in our simulation (Fig. ~~S8~~ ~~10~~S13). Coagulation, particularly among nanoparticles, increases collision probabilities, leading to the formation of larger particles and reduction in particle number concentration, and a shift in size distribution toward larger diameters (Jacobson, 2005; Seinfeld and Pandis, 2016). In this study, the simulated number concentration without coagulation declined more slowly than measurements throughout the whole simulation period (Fig. ~~S8~~S13), resulting in an overestimation of 14.4% ± 7.9%, which is much more deviated from measured than that when including coagulation. In spite of using a semi-implicit coagulation equation (Jacobson, 2005) without adjustable parameters, our result suggests that the rates of coagulation of particles are well represented in PyCHAM model.

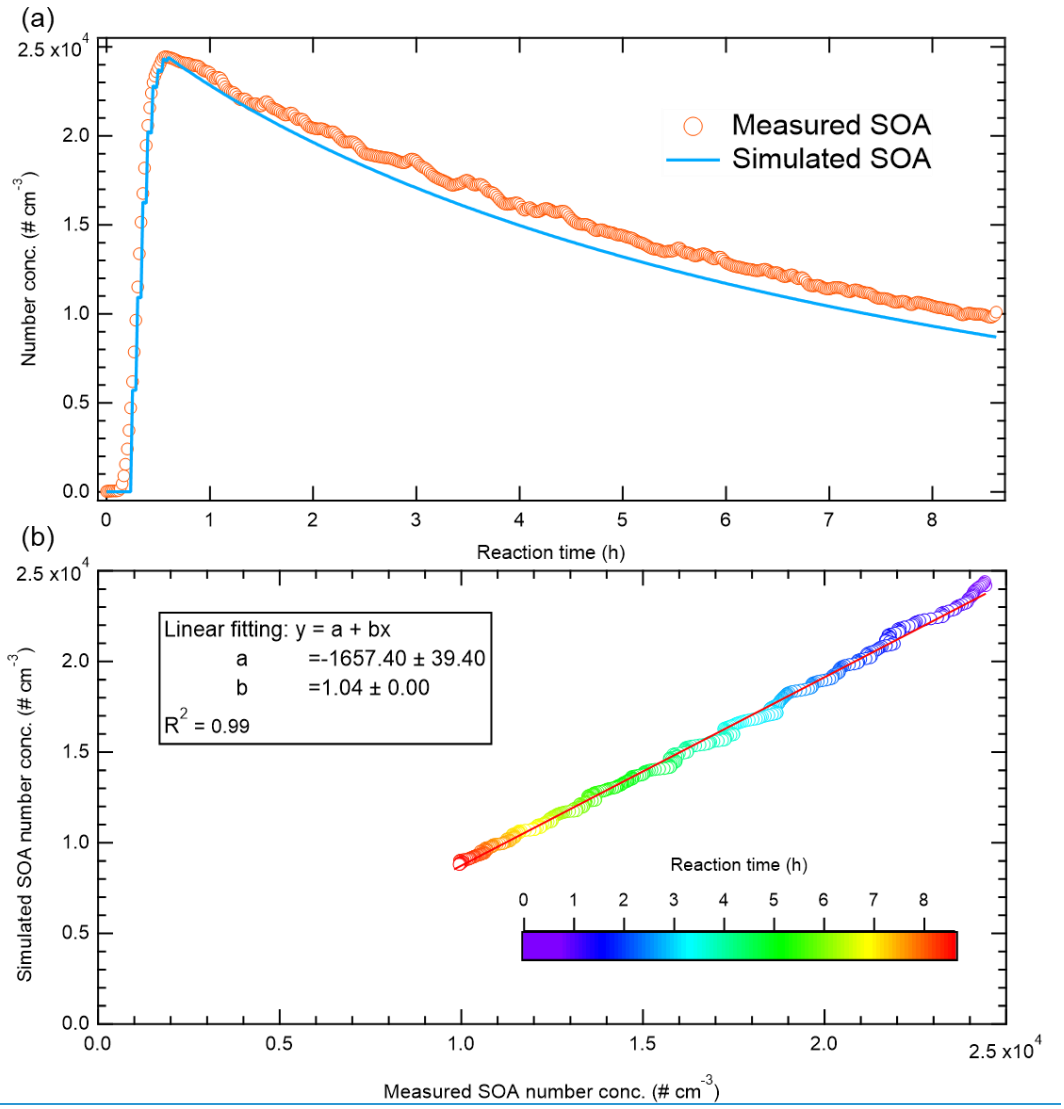

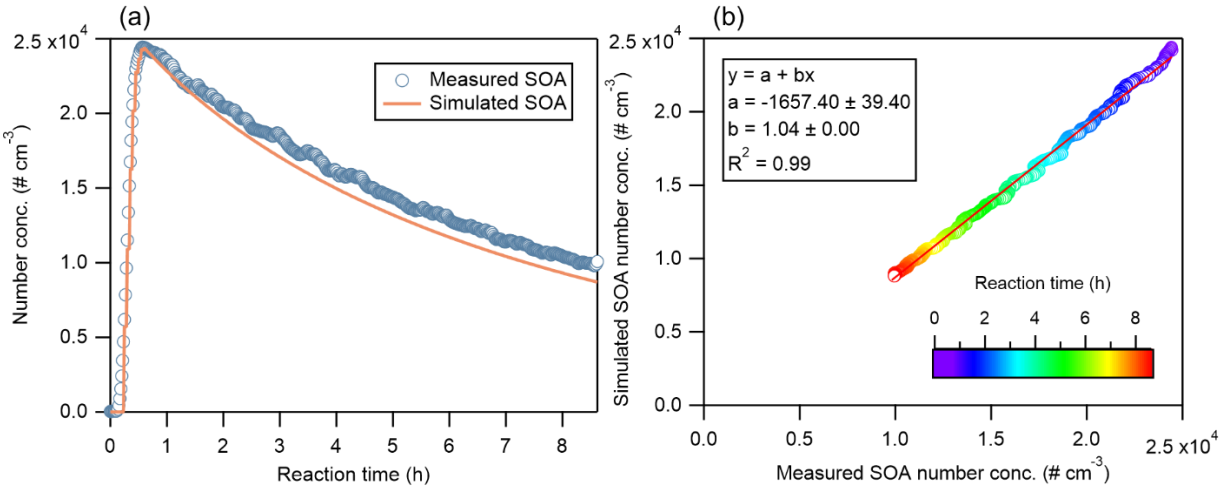

Figure 3: (a-b) Same as Fig. 1, but for SOA number concentration (# cm^{-3}). ~~Scatters~~Data points from the initial 0.6 ~~hours were~~h are excluded~~, as~~ from the scatterplot because the number concentration during this period was fitted to the SMPS measurements and therefore assumed to match the measurements ~~perfectly~~exactly. Note that ~~the~~ coagulation is included in the simulation.

To further evaluate simulation accuracy of particle size, the geometric mean diameter of simulated SOA was calculated (Fig. 4), which showed good agreement with measurements (R^2 = 0.96) and a slight underestimation of 1.9% ± 2.8%, indicating an excellent reproduction of the central position of size distribution. Without PRAM mechanism, the geometric mean diameter of SOA was lower due to the absent production of larger molecules. When coagulation was excluded, the geometric mean diameter was underestimated by 8.8% ± 1.1% (Fig. ~~S9~~S14), and was merely underestimated by 6.9% ± 2.9% compared to the

result including coagulation, suggesting that particle growth during the reaction was primarily driven by condensation, overweighing the influence of coagulation on the size distribution. As a result, the size distribution showed only minor changes due to coagulation, which is in contrast with the large changes in particle number concentrations (Fig. ~~S8~~S13).

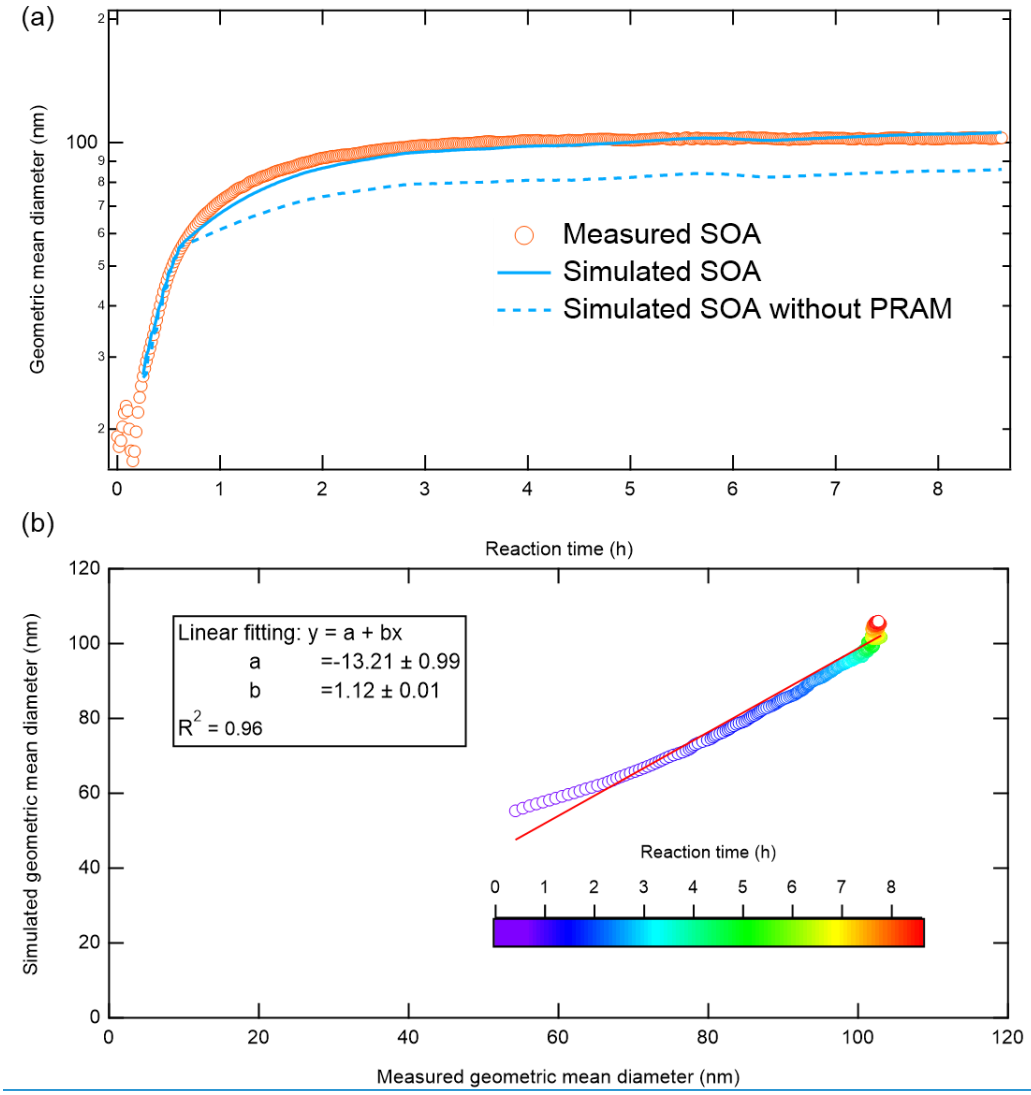

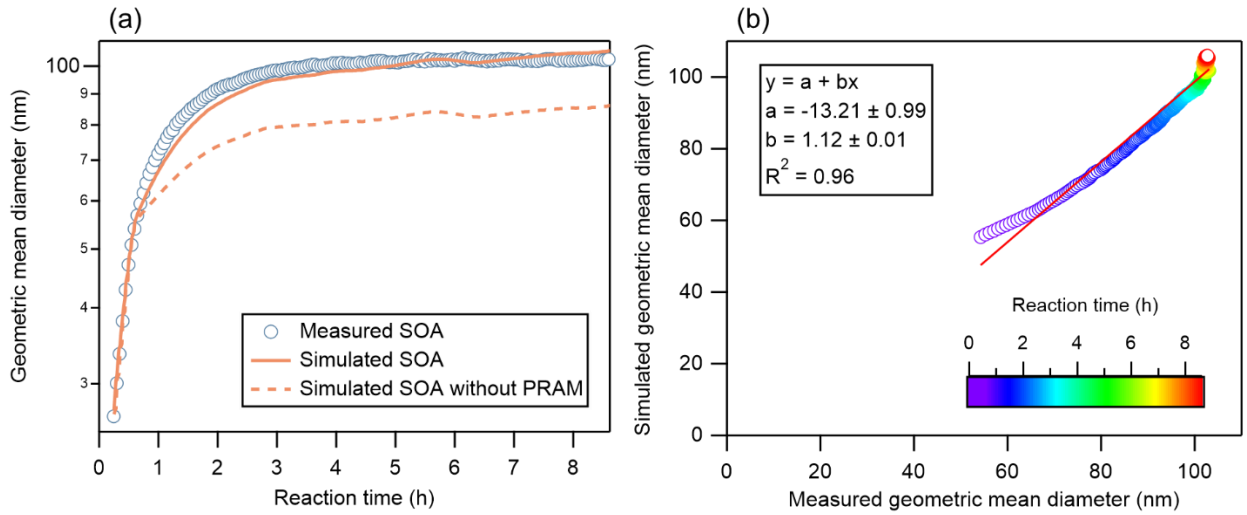

Figure 4: (a-b) Same as Fig. 1, but for the geometric mean diameter (nm) of SOA. ~~And blue~~The dashed line refers to the simulated SOA without ~~considering~~the PRAM mechanism. ~~Note that the coagulation~~Coagulation is included~~, and scatters~~ in the simulation. Data points from the initial 0.6 ~~hours were~~h are excluded ~~as particle size distribution~~from the scatterplot because the PSD during this period was fitted to the SMPS measurements.

Figure 5 compares the measured and simulated number size distributions of SOA, with shaded areas representing simulations and contour lines denoting measurements. The simulation effectively captured the trend of particle growth, and the simulated size range generally aligned with measurements. However, simulated ~~particle size distribution~~PSD showed flatter and ~~wider~~broader distribution patterns than measurement, even though ~~we~~it was constrained ~~them~~ by SMPS during the initial 0.6 ~~hours~~h. Figure S15 presents the $dN/dlog_{10}D_p$ versus PSD at 2, 4, 6, and 8 h of reaction time, clearly illustrating that the simulated PSDs were broader and flatter than measurement. When nucleation parameters were assigned to simulate initial particle growth in PyCHAM, instead of constraining the initial ~~particle size distribution~~PSD with SMPS ~~measurements~~measurement, the simulated size distribution exhibited greater deviation from measured data (Fig. S4-5). Xu (2021) assigned the nucleation parameters for the initial particle growth in PyCHAM, and ~~simulated~~found smaller particle ~~sizes~~size and a slower particle growth than ~~measurements~~measurement. These results indicate that no matter whether nucleation or seed particles are used to specify the initial number ~~particle size distribution~~PSD in PyCHAM, the model currently still ~~needs improvement to better represent~~ need improve representation of the evolution of particle size. Nevertheless, as the model has generally well reproduced the particle size and number ~~concentrations~~concentration, it can be used for subsequent CCN simulations. When coagulation was excluded in our study ~~(Fig. S10),~~, the simulated ~~particle size distribution~~PSD showed some odd spikes in the early stage and more deviation from the measurement especially in the subsequent growth stage~~,~~ (Fig. S16), demonstrating the reliable representation of coagulation in PyCHAM model.

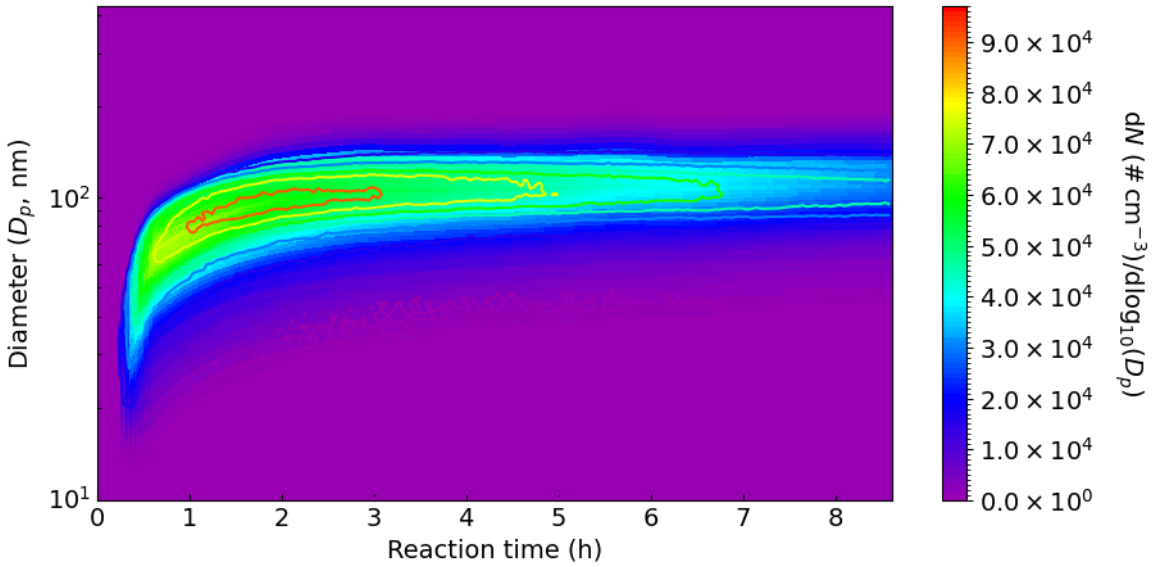

Figure 5: ~~The time~~Time evolution of the number size distributions ($dN/dlog_{10}D_p$) ~~of~~for measured (contour lines) and simulated (shaded areas) SOA. ~~Note that the coagulation~~Coagulation is included in the simulation.

3.3 Simulation of κ and CCN ~~Concentrations~~concentrations

We calculated the hygroscopicity parameter (κ) of bulk SOA under ideal condition using the UManSysProp and compared with measurement (Fig. 6). The measured κ generally increased with higher SS, which is possibly attributed to the size dependence of chemical composition, consistent with previous monoterpene oxidation studies (Zhao et al., 2015a; Zhang et al., 2023). In contrast, ~~the~~ simulated κ was independent of SS and did not show a significant size dependence. From 50.6 nm to 84.8 nm of particle size, the κ derived from the chemical composition corresponding to size only decreased by 0.002, indicating weak dependence of simulated chemical composition on particle size, which is different from the measurement (Table ~~S1).~~S2). The sudden decrease in κ measured at ~2 h of reaction is attributed to the decrease of the set SS from 0.73% to 0.19%. In contrast, the simulated κ was formula-based and did not correspond to specific SS. The simulated κ increased during the first hour before stabilizing at 0.172 ± 0.003. Compared to measurements, the simulated κ was underestimated by 20.7% ± 4.9% at higher SS levels (0.73% and 0.55%), overestimated by 18.6% ± 5.9% at SS = 0.19%, and showed the closest

agreement at SS = 0.37%, with an overestimation of 9.6% ± 8.5%. Overall, the simulated κ agreed well with measurements, particularly at ~~lower~~moderate SS ~~levels.~~(0.37%).

Field observation and laboratory studies have shown that κ of SOA decreases with increasing molecular weight under supersaturated conditions (Kuwata et al., 2013; Wang et al., 2019). We computed the average molecular weight of SOA (Fig. ~~S11~~S17) and found that the molecular weight decreased rapidly during the initial phase before stabilizing, explaining the measured and simulated increase in κ in the early stage in the experiment and its subsequent leveling off.

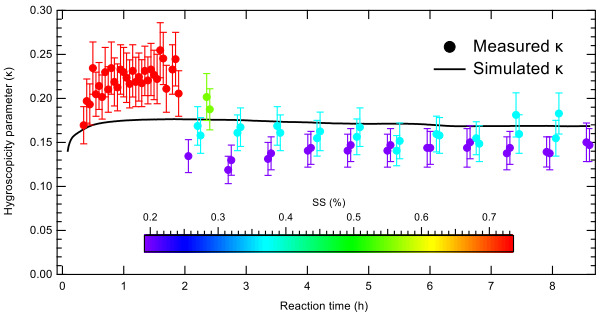

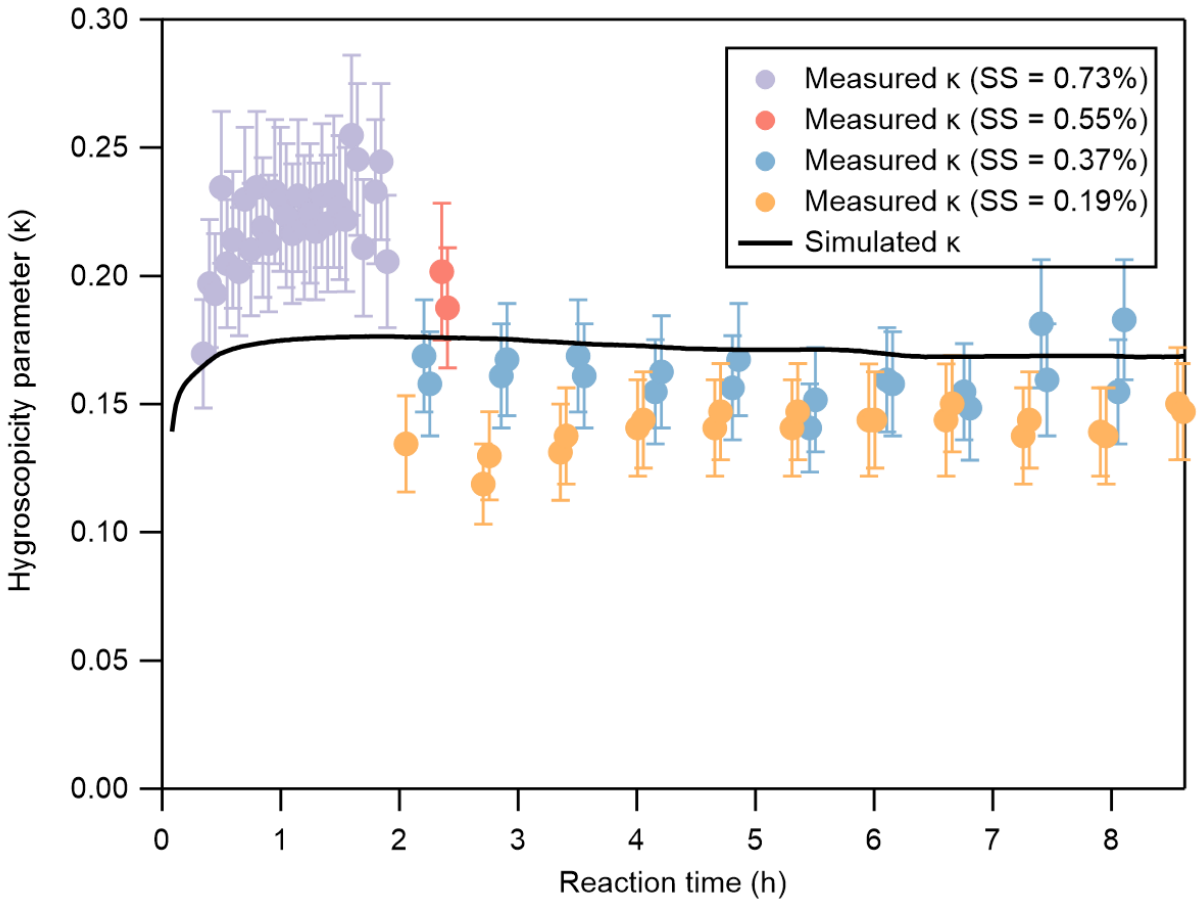

Figure 6: ~~The hygroscopicity~~Hygroscopicity parameter (κ) of simulated SOA (line) and measured SOA (solid circles~~) SOA~~ with standard ~~–~~deviation (~~error bar~~bars) at different supersaturation (SS). After ~2 h, κ values were showed only for SS = 0.19% and 0.37%, because the D_{crit} derived from fitting CCN/CN activation fraction curves at SS = 0.73% and 0.55% had too large uncertainties as almost all particles were activated.

CCN number concentrations at different SS levels were derived using κ ~~and particle size distribution~~ from the nucleation scheme and PSD from the seed scheme (Fig. 7). Figure S18 presents the PSD and D_{crit} at four SS levels corresponding to time points before and after 2 h, providing additional context for interpreting the discrepancies between simulated and measured CCN. At the higher SS levels ~~(~~of 0.73% and 0.55~~%),~~%, the simulated CCN number ~~concentration~~ concentrations closely matched the measurements throughout the reaction ~~time~~ (R^2 = 0.88 ~~–~~0.99), ~~with the exception of~~except for a more rapid increase during the initial period at SS = 0.73%. Although ~~the simulated κ were significantly~~ κ was underestimated ~~compared to the corresponding measured κ at~~ at these ~~two~~ SS ~~levels~~, leading to ~~an overestimation of the CCN critical activated dry particle size ($D_{p,dry}$), the close agreement between~~ slightly overestimated D_{crit}, the simulated and measured ~~geometric mean diameter of SOA (Fig. 4) resulted in a compensatory effect. Specifically, the wider and flatter size distribution patterns~~ D_{crit} were still very similar and both positioned to the left of the PSD peak (Fig. S18c and d). Under these conditions, the broader and flatter simulated PSD introduced a compensating effect, resulting in simulated CCN concentrations that were very close to the measurements. The slight overestimation of CCN before 0.6 h at SS = 0.73% was primarily attributable to the low bias in ~~the simulation compensated the impact of the lower~~ simulated κ, ~~coincidentally yielding a good agreement in CCN number concentrations at these two SS.~~ since the simulated and measured PSD were identical during this period.

At SS = 0.37%, the simulated CCN number ~~concentration showed close agreement~~concentrations also agreed closely with ~~the~~ measured CCN (R^2 = 0.98~~),~~) with a mean bias of -3.9% ± 1.9%. ~~This consistency in CCN concentration corresponded~~This good agreement corresponds to the smallest discrepancy ~~in~~ between simulated and measured κ at this SS. Although ~~the simulated~~ κ was slightly ~~higher, a concurrently slightly lower simulated particle size resulted in a comparable CCN value.~~overestimated at SS = 0.37%, the simulated and measured D_{crit} remained very similar and both lay to the left of the PSD peak (Fig. S18b). As ~~for SS = 0.19%,~~a result, the broader and flatter PSD did not introduce a noticeable bias in simulated CCN ~~number concentration exhibited the largest discrepancy among all SS levels, consistently overestimating the measured values~~ .

In contrast, at SS = 0.19%, the simulated CCN number concentrations were obviously overestimated by a factor of >4 throughout the reaction. ~~This overestimation was primarily attributed to the excessively wider and flatter simulated particle size distribution and a~~ At this lowest SS, the required D_{crit} is largest, and both simulated and measured D_{crit} were located to the right of the PSD peak (Fig. S18a). The high bias in simulated κ at this SS further reduced the simulated D_{crit}, and this underestimation, combined with the broader and flatter simulated PSD, resulted in pronounced ~~overestimation of κ at this lowest SS which led to an underestimation~~overprediction of ~~$D_{p,dry}$~~CCN relative to the measurements.

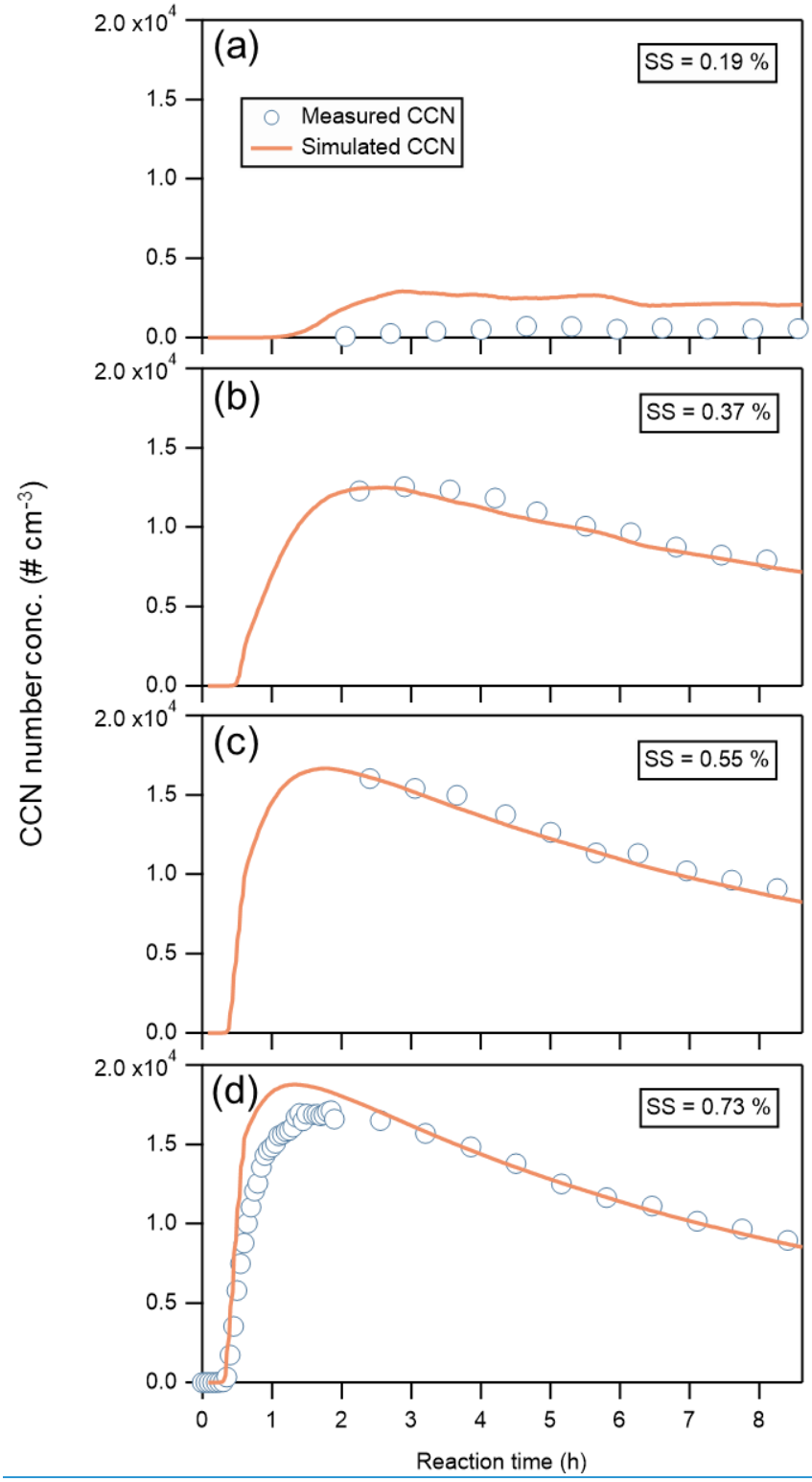

Figure 7: (a-d) Measured (circles) and simulated (lines) CCN number concentrations (# cm^{-3}) at different SS.

To further investigate the influence of κ values and ~~particle size distribution~~PSD on CCN simulation results, we systematically examined different scenarios by either:

(1) ~~maintaining~~keeping κ fixed while varying the ~~κ, and adopting the number particle~~ PSD using SMPS measurements or an 8-bin size distribution ~~of SMPS measurement or the 8-bin particle size scheme simulation which is generally~~commonly used in ~~conventional 3D~~chemical transport models (~~such as~~e.g., WRF-Chem), or

(2) ~~maintaining~~keeping the ~~number particle size distribution, and~~PSD fixed while applying ~~the~~different κ values, including κ derived ~~by~~from measurements or a fixed κ ~~of~~= 0.1 ~~generally~~, which is frequently used in ~~3D~~chemical transport models.

~~Through separate modifications of κ values and particle size distribution, we calculated the corresponding~~For each scenario, CCN number concentrations were recalculated based on the modified κ or PSD. As shown in Fig. ~~S12~~S19, when the ~~particle size distribution~~PSD was varied while ~~maintaining a~~κ remained constant ~~κ~~, the 106-bin particle size ~~scheme~~resolution employed in this study ~~demonstrated superior performance to~~substantially outperformed the conventional 8-bin ~~approach~~setting across ~~various~~all SS levels. The 106-bin results showed much closer agreement with CCN number concentrations derived from SMPS-measured ~~size distributions~~PSDs, particularly during the ~~initial growth~~early phase of CCN activation. At higher SS levels (0.73% and 0.55%), however, ~~CCN number concentrations exhibited~~ the influence of bin resolution became less significant, reflecting the reduced sensitivity ~~to the bin numbers option, indicating negligible dependence on the number size distribution, which is partly due to the $D_{p,dry}$ became~~ of CCN activation to PSD when D_{crit} is sufficiently ~~low at higher SS~~small such that most particles can act as CCN.

When κ was varied while ~~maintaining~~ the ~~number size distribution~~PSD was held constant (Fig. ~~S13~~S20), CCN number concentrations calculated using κ from UManSysProp ~~showed excellent agreement~~agreed very well with those derived from observationally inferred κ across all SS levels, except for an overestimation at the lowest SS. In contrast, the fixed κ = 0.1 ~~scheme systematically~~approach consistently underestimated CCN number concentrations, with the ~~discrepancy~~discrepancies increasing at lower SS~~. These findings indicate that the simulation of CCN concentration acted by SOA relies on the accurate representations of κ and particle size distribution, particularly for lower SS levels~~.

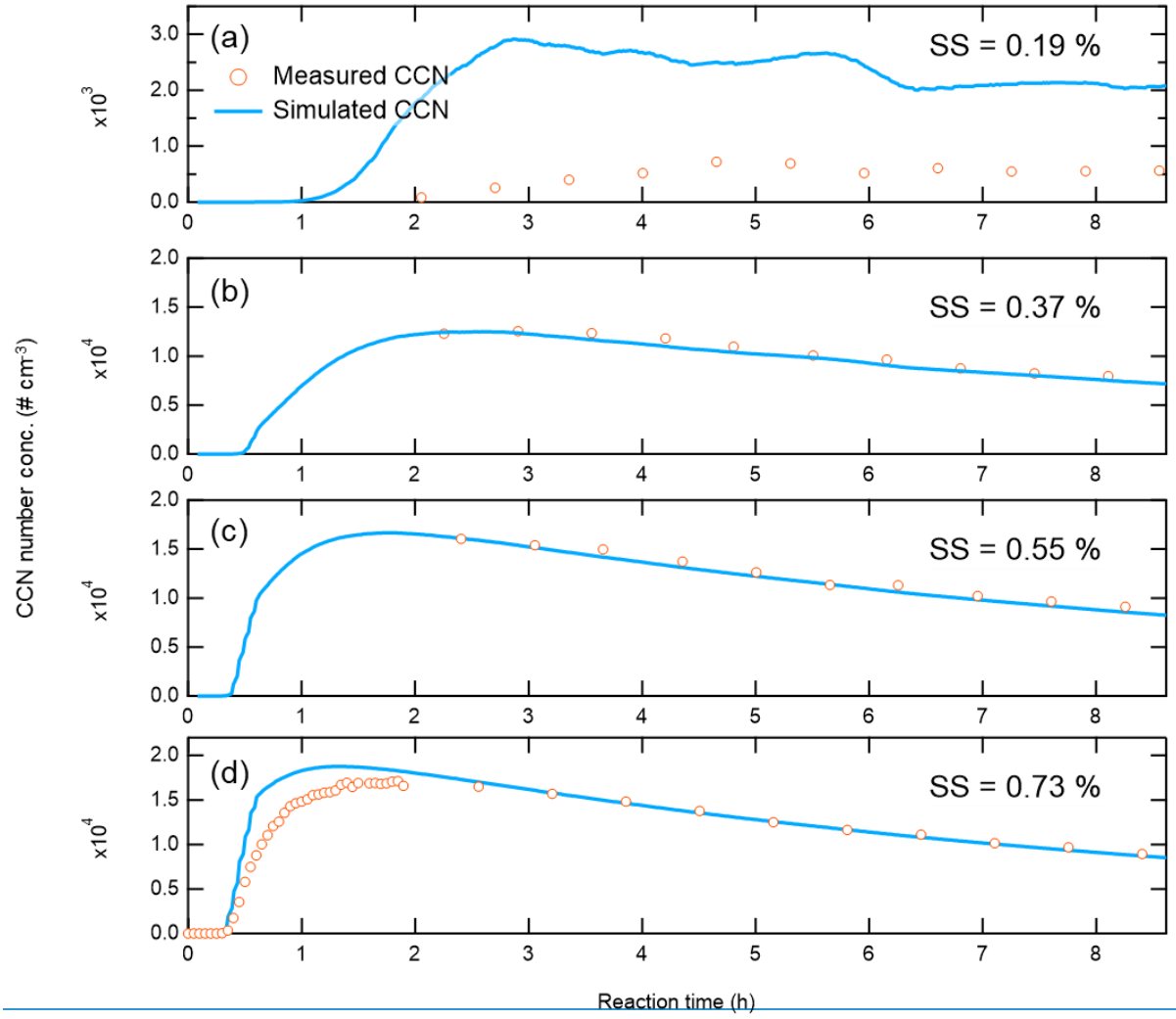

~~Figure 7: (a–d) The measured (circles)~~These findings indicate that accurate CCN simulation for SOA requires realistic representations of both κ and PSD, with their importance becoming particularly pronounced at low SS.

3.4 Discussion of the influence of individual schemes (nucleation vs. seed) on CCN predictions

To demonstrate the rationale for the combined approach - using κ from the nucleation scheme together with PSD from the seed scheme - a detailed analysis of the effect of applying each scheme independently on the CCN simulations is implemented.

As shown in Fig. S21, CCN calculated using the κ by the nucleation scheme (Fig. 6) and PSD by the same scheme (Fig. S4) at SS = 0.55% and 0.73% were comparable to those from the combined-scheme approach. However, at SS = 0.37%, CCN was moderately overestimated, and at SS = 0.19% the predicted CCN was initially higher than the measurements and then decreased toward zero. In contrast, CCN calculated using the κ from the seed scheme (Fig. S22) combined with its PSD (Fig. 5) produced lower CCN across all four SS (Fig. S23), leading to a worse performance than that of the combined-scheme approach.

Overall, if the nucleation scheme was applied alone, the simulated ~~(lines) CCN number~~PSD performed worse than that obtained with the combined approach, resulting in deviations of CCN concentrations ~~(# cm^{-3}) at different SS~~at the two lower SS. In contrast, applying the seed scheme alone led to worse simulations of initial SOA mass concentration, chemical composition, and κ due to the assumed composition of seed species. However, because the PSD remained relatively accurate, the resulting CCN concentrations were similar to those from the combined approach.

4 Conclusions and implications

In this study, we simulated mass concentration, number concentration, chemical composition (O:C and H:C ratios) and size distribution of SOA from α-pinene ozonolysis by coupling MCM and PRAM near-explicit chemical mechanisms in a process-level box model PyCHAM. We further simulated CCN number concentrations at a series of SS using hygroscopicity parameter (κ) of SOA calculated by UManSysProp according to κ-Köhler theory~~, and particle size distribution.~~ together with PSD. Compared to chamber experimental ~~measurement~~measurements, the SOA mass concentration was well reproduced with an underestimation of 19.1% ± 10.4%. O:C and H:C ratios were overestimated by 32.4% ± 2.2% and 21.2% ± 2.1%, respectively~~. Besides, the~~, and their time evolution ~~of elemental ratios~~ was inconsistent with ~~measurement~~measurements. These discrepancies were ~~likely~~possibly attributed to the ~~missing~~absence of particle-phase reactions during the simulation, as gas-phase chemistry including α-pinene decay and HOMs composition were generally well ~~represented~~reproduced. Moreover, ~~the contribution of~~ simulated particle-phase HOMs contributed substantially (~43%) to SOA mass concentration ~~was significant (~43%),~~ underscoring ~~the~~their critical role ~~of HOMs~~ in SOA production.

~~By constraining SMPS particle size distribution~~With PSD and number concentration constrained by SMPS measurement during the initial reaction ~~time~~period, the simulated SOA number concentration exhibited ~~a~~ good agreement with measurement (R^2 = 0.99). ~~The~~However, the simulated ~~particle size distribution, however,~~PSD showed ~~wider~~broader and flatter patterns than measured one, suggesting the ~~necessity to better represent~~ need for improving representation of size evolution in ~~the~~future PyCHAM ~~model in the future.~~development. Moreover, ~~the~~ simulated κ showed overestimation (18.6% ± 5.9%) at the lowest SS (0.19%) and underestimation (20.7% ± 4.9%) at higher SS levels (0.73% & 0.55%), with the closest agreement at SS = 0.37%. ~~Correspondingly, the simulated CCN number concentrations had varying levels of bias across different SS levels. Notably, at higher SS levels (0.73% and 0.55%), the~~ At SS = 0.19%, CCN activation requires larger particle sizes; under this condition, both simulated and measured D_{crit} lie to the right of the PSD peak. The combination of an underestimated ~~κ values led to an overprediction of $D_{p,dry}$, yet this bias was compensated by the wider~~simulated D_{crit} and a broader and flatter ~~particle size distribution in the simulations. As a result, the CCN number concentrations at these two SS levels exhibited excellent consistency with measurements (R^2 = 0.88–99). At SS = 0.37%, the slightly overestimated κ was balanced by the slightly lower simulated particle size, yielding closely matched CCN values (R^2 = 0.98). In contrast, at SS = 0.19%, the~~ simulated PSD leads to a substantial overestimation of ~~κ and the resulted underestimated $D_{p,dry}$, coupled with the excessively wider~~CCN. In contrast, at the other SS levels, despite the broader and flatter ~~particle size distribution, collectively led~~simulated PSD, the

simulated and measured D_{crit} are very similar and lie to ~~a significant overestimation of CCN number concentrations.~~the left of the PSD peak. Consequently, the broader and flatter simulated PSD partially compensate for the small differences in D_{crit}, resulting in CCN number concentrations that differ only slightly from the measurements (R^2 = 0.88–99).

To further quantify the individual contributions of κ and ~~size distribution~~PSD on CCN, we conducted comparison analyses ~~by~~ using different κ schemes and different ~~number~~numbers of particle size bins ~~to represent the number size distribution. It is~~. We found that accurate representation of both κ and ~~particle size distribution is critical~~PSD is essential for reliable CCN simulations ~~acted~~activated by SOA, particularly at ~~lower~~low SS ~~levels~~ (<0.4%). At higher SS ~~levels~~ (>0.4%), ~~however,~~ the sensitivity of CCN predictions to these parameters ~~decreases as SS increases, as the smaller $D_{p,dry}$ at higher SS render~~decreased, because the reduced D_{crit} allows most particles to ~~act~~activate as CCN regardless of variations in κ or ~~size distribution~~PSD.

~~This study advances previous research by simulating CCN number concentrations from SOA using explicit chemical mechanisms (MCM + PRAM) for the first time to our knowledge. We comprehensively examined how SOA mass concentration, chemical composition, hygroscopicity, and size distribution collectively influence CCN formation. Although our simulation, like earlier studies, exhibits biases chemical composition, we highlight the importance of missing particle-phase processes in SOA production. Crucially, the simulated size distribution and hygroscopicity impact the CCN predictions especially at lower supersaturations. This study highlights that accurately representing SOA hygroscopicity and size distribution is key to reducing modelled CCN uncertainties.~~

This study advances previous research by simulating CCN formation from SOA using a near-explicit and process-level model for the first time to our knowledge, and demonstrates the potential of this approach to inform the development of parameterizations in chemical transport models. Although current model still has some limitations, such as the absence of particle-phase chemistry, lack of explicit treatment of activity coefficients, and the inability to prescribe physically based nucleation and initial PSD, the model reproduces key features of the measured SOA and CCN reasonably well. Our findings further indicate that simplified representations of PSD and κ are insufficient for accurately describing CCN. These results suggest that HOMs chemistry, finer PSD resolution and improved κ parameterizations in chemical transport models are warranted. Improvement in process-level model e.g. including particle-phase chemistry, explicit treatment of activity coefficients, and allowing prescribing physically based nucleation and initial PSD are warranted in future work to provide a benchmark model to evaluate various parameterizations related to SOA formation and CCN concentrations. And future work could also extend this analysis to a range of biogenic and anthropogenic VOCs oxidation systems to develop generalized PSD and κ parameterization modules, potentially through training AI-based methods capable of learning sophisticated and process-informed parameterizations, which may be used to improve chemical transport models.

Data availability

~~All~~The input files including model variables setting and chemical mechanism files used in PyCHAM are available on Zenodo at https://doi.org/10.5281/zenodo.17539325. And all the data in the figures of this study are available upon request to the corresponding author (dfzhao@fudan.edu.cn).

Supplement

Author contributions

DZ conceptualized the study. ZS performed the model simulation. CZ analyzed the measured CCN data and calculated the hygroscopicity parameter. HM analyzed the mass spectra data of gas-phase HOMs. ZS wrote the manuscript. ZS and DZ edited the manuscript with the input from all co-authors. All the co-authors discussed the results and commented on the manuscript.

Competing interests

The authors declare that they have no conflict of interest.

Acknowledgements

Zhen Song, Chenqi Zhang, Hongru Shen, Hao Ma, and Defeng Zhao would like to thank the funding support of Shanghai Pilot Program for Basic Research-Fudan University 21TQ1400100 (22TQ010) and the National Natural Science Foundation of China (No. 42575109). We thank Thomas F. Mentel for the support of this study. We gratefully acknowledge Simon Patrick O'Meara for updating the code and function of PyCHAM and the support of the xml file in simulation.

We gratefully thank Simon Patrick O'Meara and the anonymous reviewer for their constructive comments and valuable suggestions, which have significantly improved the quality of our manuscript.

Financial support

This research has been supported by Shanghai Pilot Program for Basic Research-Fudan University 21TQ1400100 (22TQ010) and the National Natural Science Foundation of China (No. 42575109).

References

Aumont, B., Szopa, S., and Madronich, S.: Modelling the evolution of organic carbon during its gas-phase tropospheric oxidation: development of an explicit model based on a self generating approach, Atmos. Chem. Phys., 5, 2497–2517, https://doi.org/10.5194/acp-5-2497-2005, 2005.

Bianchi, F., Kurtén, T., Riva, M., Mohr, C., Rissanen, M. P., Roldin, P., Berndt, T., Crounse, J. D., Wennberg, P. O., Mentel, T. F., Wildt, J., Junninen, H., Jokinen, T., Kulmala, M., Worsnop, D. R., Thornton, J. A., Donahue, N., Kjaergaard, H. G., and Ehn, M.: Highly oxygenated organic molecules (HOM) from gas-phase autoxidation involving peroxy radicals: a key contributor to atmospheric aerosol, Chem. Rev., 119, 3472–3509, https://doi.org/10.1021/acs.chemrev.8b00395, 2019.

Camredon, M., Aumont, B., Lee-Taylor, J., and Madronich, S.: The SOA/VOC/NO_x system: an explicit model of secondary organic aerosol formation, Atmos. Chem. Phys., 7, 5599–5610, https://doi.org/10.5194/acp-7-5599-2007, 2007.

Capouet, M., Mueller, J. F., Ceulemans, K., Compernolle, S., Vereecken, L., and Peeters, J.: Modeling aerosol formation in alpha-pinene photo-oxidation experiments, J. Geophys. Res.-Atmos., 113, D02308, https://doi.org/10.1029/2007jd008995, 2008.

Capouet, M., Peeters, J., Nozi`ere, B., and Müller, J.-F.: Alpha-pinene oxidation by OH: simulations of laboratory experiments, Atmos. Chem. Phys., 4, 2285–2311, https://doi.org/10.5194/acp-4-2285-2004, 2004.

Ceulemans, K., Compernolle, S., Peeters, J., and M¨ uller, J.-F.: Evaluation of a detailed model of secondary organic aerosol formation from α-pinene against dark ozonolysis experiments, Atmos. Environ., 44, 5434–5442, https://doi.org/10.1016/j.atmosenv.2010.05.001, 2010.

Chen, Q., Liu, Y. D., Donahue, N. M., Shilling, J. E., and Martin, S. T.: Particle-phase chemistry of secondary organic material: modeled compared to measured O:C and H:C elemental ratios provide constraints., Environ. Sci. Technol., 45, 4763–4770, https://doi.org/10.1021/es104398s, 2011.

DeCarlo, P. F., Kimmel, J. R., Trimborn, A., Northway, M. J., Jayne, J. T., Aiken, A. C., Gonin, M., Fuhrer, K., Horvath, T., Docherty, K. S., Worsnop, D. R., and Jimenez, J. L.: Field-deployable, high-resolution, time-of-flight aerosol mass spectrometer, Anal. Chem., 78, 8281–8289, https://doi.org/10.1021/ac061249n, 2006.

Donahue, N. M., Robinson, A. L., Stanier, C. O., and Pandis, S. N.: Coupling partitioning, dilution, and chemical aging of semivolatile organics, Environ. Sci. Technol., 40, 2635–2643, https://doi.org/10.1021/es052297c, 2006.

Ehn, M., Thornton, J. A., Kleist, E., Sipilä, M., Junninen, H., Pullinen, I., Springer, M., Rubach, F., Tillmann, R., Lee, B., Lopez-Hilfiker, F., Andres, S., Acir, I. H., Rissanen, M., Jokinen, T., Schobesberger, S., Kangasluoma, J., Kontkanen, J., Nieminen, T., Kurtén, T., Nielsen, L. B., Jørgensen, S., Kjaergaard, H. G., Canagaratna, M., Dal Maso, M., Berndt, T., Petäjä, T., Wahner, A., Kerminen, V. M., Kulmala, M., Worsnop, D. R., Wildt, J., and Mentel, T. F.: A large source of low-volatility secondary organic aerosol, Nature, 506, 476–485, https://doi.org/10.1038/nature13032, 2014.

Fanourgakis, G. S., Kanakidou, M., Nenes, A., Bauer, S. E., Bergman, T., Carslaw, K. S., Grini, A., Hamilton, D. S., Johnson, J. S., Karydis, V. A., Kirkevåg, A., Kodros, J. K., Lohmann, U., Luo, G., Makkonen, R., Matsui, H., Neubauer, D., Pierce, J. R., Schmale, J., Stier, P., Tsigaridis, K., van Noije, T., Wang, H., Watson-Parris, D., Westervelt, D. M., Yang, Y., Yoshioka, M., Daskalakis, N., Decesari, S., Gysel-Beer, M., Kalivitis, N., Liu, X., Mahowald, N. M., Myriokefalitakis, S., Schrödner, R., Sfakianaki, M., Tsimpidi, A. P., Wu, M., and Yu, F.: Evaluation of global simulations of aerosol particle and cloud condensation nuclei number, with implications for cloud droplet formation, Atmos. Chem. Phys., 19, 8591–8617, https://doi.org/10.5194/acp-19-8591-2019, 2019.

Farmer, D. K., Cappa, C. D., and Kreidenweis, S. M.: Atmospheric processes and their controlling influence on cloud condensation nuclei activity, Chem. Rev., 115, 4199–4217, https://doi.org/10.1021/cr5006292, 2015.

Fuchs, H., Dorn, H.-P., Bachner, M., Bohn, B., Brauers, T., Gomm, S., Hofzumahaus, A., Holland, F., Nehr, S., Rohrer, F., Tillmann, R., and Wahner, A.: Comparison of OH concentration measurements by DOAS and LIF during SAPHIR chamber experiments at high OH reactivity and low NO concentration, Atmos. Meas. Tech., 5, 1611–1626, https://doi.org/10.5194/amt-5-1611-2012, 2012.

Fuchs, N. and Sutugin, A.: Highly dispersed aerosols, Butterworth Heinemann, Woburn, MA, USA, 1971.

Galeazzo, T., Valorso, R., Li, Y., Camredon, M., Aumont, B., and Shiraiwa, M.: Estimation of secondary organic aerosol viscosity from explicit modeling of gas-phase oxidation of isoprene and α-pinene, Atmos. Chem. Phys., 21, 10199–10213, https://doi.org/10.5194/acp-21-10199-2021, 2021.

Gatzsche, K., Iinuma, Y., Tilgner, A., Mutzel, A., Berndt, T., and Wolke, R.: Kinetic modeling studies of SOA formation from α-pinene ozonolysis, Atmos. Chem. Phys., 17, 13187–13211, https://doi.org/10.5194/acp-17-13187-2017, 2017.

Girolami, G. S.: A simple “back of the envelope” method for estimating the densities and molecular volumes of liquids and solids, J. Chem. Educ., 71, 962–964, https://doi.org/10.1021/ed071p962, 1994.

Griffin, R. J., Dabdub, D., and Seinfeld, J. H.: Secondary organic aerosol 1. Atmospheric chemical mechanism for production of molecular constituents, J. Geophys. Res., 107, 4332, https://doi.org/10.1029/2001JD000541, 2002.

Guo, Y., Shen, H., Pullinen, I., Luo, H., Kang, S., Vereecken, L., Fuchs, H., Hallquist, M., Acir, I.-H., Tillmann, R., Rohrer, F., Wildt, J., Kiendler-Scharr, A., Wahner, A., Zhao, D., and Mentel, T. F.: Identification of highly oxygenated organic molecules and their role in aerosol formation in the reaction of limonene with nitrate radical, Atmos. Chem. Phys., 22, 11323–11346, https://doi.org/10.5194/acp-22-11323-2022, 2022.

Hallquist, M., Wenger, J. C., Baltensperger, U., Rudich, Y., Simpson, D., Claeys, M., Dommen, J., Donahue, N. M., George, C., Goldstein, A. H., Hamilton, J. F., Herrmann, H., Hoffmann, T., Iinuma, Y., Jang, M., Jenkin, M. E., Jimenez, J. L., Kiendler-Scharr, A., Maenhaut, W., McFiggans, G., Mentel, Th. F., Monod, A., Prévôt, A. S. H., Seinfeld, J. H., Surratt, J. D., Szmigielski, R., and Wildt, J.: The formation, properties and impact of secondary organic aerosol: current and emerging issues, Atmos. Chem. Phys., 9, 5155–5236, https://doi.org/10.5194/acp-9-5155-2009, 2009.

Hodzic, A. and Jimenez, J. L.: Modeling anthropogenically controlled secondary organic aerosols in a megacity: a simplified framework for global and climate models, Geosci. Model Dev., 4, 901–917, https://doi.org/10.5194/gmd-4-901-2011, 2011.

Hu, D., Tolocka, M., Li, Q., and Kamens, R. M.: A kinetic mechanism for predicting secondary organic aerosol formation from toluene oxidation in the presence of NO_x and natural sunlight, Atmos. Environ., 41, 6478–6496, https://doi.org/10.1016/j.atmosenv.2007.04.025, 2007.

Huang, RJ., Zhang, Y., Bozzetti, C. et al.: High secondary aerosol contribution to particulate pollution during haze events in China, Nature, 514, 218–222, https://doi.org/10.1038/nature13774, 2014.

IPCC.: Climate change 2021: The physical science basis. Contribution of working group I to the sixth assessment report of the Intergovernmental Panel on Climate Change, Cambridge University Press, https://doi.org/10.1017/9781009157896, 2021.

Jacobson, M.: Fundamentals of atmospheric modeling, Cambridge University Press, https://doi.org/10.1017/CBO9781139165389, 2005.

Jenkin, M. E., Saunders, S. M., and Pilling, M. J.: The tropospheric degradation of volatile organic compounds: A protocol for mechanism development, Atmos. Environ., 31, 81–104, https://doi.org/10.1016/S1352-2310(96)00105-7, 1997.

Jenkin, M. E., Saunders, S. M., Wagner, V., and Pilling, M. J.: Protocol for the development of the Master Chemical Mechanism, MCM v3 (Part B): tropospheric degradation of aromatic volatile organic compounds, Atmos. Chem. Phys., 3, 181–193, https://doi.org/10.5194/acp-3-181-2003, 2003.

Jenkin, M. E.: Modelling the formation and composition of secondary organic aerosol from α- and β-pinene ozonolysis using MCM v3, Atmos. Chem. Phys., 4, 1741–1757, https://doi.org/10.5194/acp-4-1741-2004, 2004.

Jia, L. and Xu, Y. F.: A core-shell box model for simulating viscosity dependent secondary organic aerosol (CSVA) and its application, Sci. Total Environ., 789, 147954, https://doi.org/10.1016/j.scitotenv.2021.147954, 2021.

Jimenez, J. L., Canagaratna, M. R., Donahue, N. M., Prevot, A. S. H., Zhang, Q., Kroll, J. H., DeCarlo, P. F., Allan, J. D., Coe, H., Ng, N. L., Aiken, A. C., Docherty, K. S., Ulbrich, I. M., Grieshop, A. P., Robinson, A. L., Duplissy, J., Smith, J. D., Wilson, K. R., Lanz, V. A., Hueglin, C., Sun, Y. L., Tian, J., Laaksonen, A., Raatikainen, T., Rautiainen, J., Vaattovaara, P., Ehn, M., Kulmala, M., Tomlinson, J. M., Collins, D. R., Cubison, M. J., Dunlea, E. J., Huffman, J. A., Onasch, T. B., Alfarra, M. R., Williams, P. I., Bower, K., Kondo, Y., Schneider, J., Drewnick, F., Borrmann, S., Weimer, S., Demerjian, K., Salcedo, D., Cottrell, L., Griffin, R., Takami, A., Miyoshi, T., Hatakeyama, S., Shimono, A., Sun, J. Y., Zhang, Y. M., Dzepina, K., Kimmel, J. R., Sueper, D., Jayne, J. T., Herndon, S. C., Trimborn, A. M., Williams, L. R., Wood, E. C., Middlebrook, A. M., Kolb, C. E., Baltensperger, U., and Worsnop, D. R.: Evolution of organic aerosols in the atmosphere, Science, 326, 1525–1529, DOI: 10.1126/science.118035, 2009.

Johnson David, Jenkin Michael E., Wirtz Klaus, Martin-Reviejo Montserrat.: Simulating the formation of secondary organic aerosol from the photooxidation of toluene, Environmental Chemistry, 1, 150–165, https://doi.org/10.1071/EN04069, 2004.

Johnson, D., Jenkin, M.E., Wirtz, K., & Martín-Reviejo, M.: Simulating the formation of secondary organic aerosol from the photooxidation of aromatic hydrocarbons, Environmental Chemistry, 2, 35–48, https://doi.org/10.1071/EN04079, 2005.

Kanakidou, M., Seinfeld, J. H., Pandis, S. N., Barnes, I., Dentener, F. J., Facchini, M. C., Van Dingenen, R., Ervens, B., Nenes, A., Nielsen, C. J., Swietlicki, E., Putaud, J. P., Balkanski, Y., Fuzzi, S., Horth, J., Moortgat, G. K., Winterhalter, R., Myhre, C. E. L., Tsigaridis, K., Vignati, E., Stephanou, E. G., and Wilson, J.: Organic aerosol and global climate modelling: a review, Atmos. Chem. Phys., 5, 1053–1123, https://doi.org/10.5194/acp-5-1053-2005, 2005.

Kelly, Janya L., Michelangeli, Diane V., Makar, Paul A., Hastie, Donald R., Mozurkewich, Michael, Auld, Janeen.: Aerosol speciation and mass prediction from toluene oxidation under high NO_x conditions, Atmos. Environ., 44, 361–369, https://doi.org/10.1016/j.atmosenv.2009.10.035, 2010.

Kreidenweis, S. M., Koehler, K., DeMott, P. J., Prenni, A. J., Carrico, C., and Ervens, B.: Water activity and activation diameters from hygroscopicity data - Part I: Theory and application to inorganic salts, Atmos. Chem. Phys., 5, 1357–1370, https://doi.org/10.5194/acp-5-1357-2005, 2005.

Kroll, J. H., and Seinfeld., J. H.: Chemistry of secondary organic aerosol: Formation and evolution of low-volatility organics in the atmosphere, Atmos. Environ., 42, 3593–3624, https://doi.org/10.1016/j.atmosenv.2008.01.003, 2008.

Kuang, Y., Xu, W., Tao, J. et al.: A review on laboratory studies and field measurements of atmospheric organic aerosol hygroscopicity and its parameterization based on oxidation levels, Curr Pollution Rep 6, 410–424, https://doi.org/10.1007/s40726-020-00164-2, 2020.

Kuwata, M., Shao, W., Lebouteiller, R., and Martin, S. T.: Classifying organic materials by oxygen-to-carbon elemental ratio to predict the activation regime of Cloud Condensation Nuclei (CCN), Atmos. Chem. Phys., 13, 5309–5324, https://doi.org/10.5194/acp-13-5309-2013, 2013.

La, Y. S., Camredon, M., Ziemann, P. J., Valorso, R., Matsunaga, A., Lannuque, V., Lee-Taylor, J., Hodzic, A., Madronich, S., and Aumont, B.: Impact of chamber wall loss of gaseous organic compounds on secondary organic aerosol formation: explicit modeling of SOA formation from alkane and alkene oxidation, Atmos. Chem. Phys., 16, 1417–1431, https://doi.org/10.5194/acp-16-1417-2016, 2016.

Lannuque, V., D'Anna, B., Kostenidou, E., Couvidat, F., Martinez-Valiente, A., Eichler, P., Wisthaler, A., Müller, M., Temime-Roussel, B., Valorso, R., and Sartelet, K.: Gas–particle partitioning of toluene oxidation products: an experimental and modeling study, Atmos. Chem. Phys., 23, 15537–15560, https://doi.org/10.5194/acp-23-15537-2023, 2023.

Liu, X. H. and Wang, J.: How important is organic aerosol hygroscopicity to aerosol indirect forcing? Environ. Res. Lett, 5, 044010, doi:10.1088/1748-9326/5/4/044010, 2010.

Lopez, B., Nirvan Bhattacharyya, Jenna DeVivo, Mingyi Wang, Lucia Caudillo-Plath, Mihnea Surdu, Federico Bianchi, Zoé Brasseur, Angela Buchholz, Dexian Chen, Jonathan Duplissy, Xu-Cheng He, Victoria Hofbauer, Naser Mahfouz, Vladimir Makhmutov, Ruby Marten, Bernhard Mentler, Maxim Philippov, Meredith Schervish, Dongyu S. Wang, Stefan K. Weber, André Welti, Imad El Haddad, Katrianne Lehtipalo, Markku Kulmala, Douglas Worsnop, Jasper Kirkby, Roy L. Mauldin, Dominik Stolzenburg, Siegfried Schobesberger, Richard Flagan and Neil M. Donahue.: A diagonal volatility basis set to assess the condensation of organic vapors onto particles, Environ. Sci.: Atmos., 5, 1035-1061, https://doi.org/10.1039/D5EA00062A, 2025.

Lowe, D., Topping, D., and McFiggans, G.: Modelling multi-phase halogen chemistry in the remote marine boundary layer: investigation of the influence of aerosol size resolution on predicted gas- and condensed-phase chemistry, Atmos. Chem. Phys., 9, 4559–4573, https://doi.org/10.5194/acp-9-4559-2009, 2009.

Luo, G. and Yu, F.: Simulation of particle formation and number concentration over the Eastern United States with the WRF-Chem + APM model, Atmos. Chem. Phys., 11, 11521–11533, https://doi.org/10.5194/acp-11-11521-2011, 2011.

Luo, Y., Thomsen, D., Iversen, E. M., Roldin, P., Skønager, J. T., Li, L., Priestley, M., Pedersen, H. B., Hallquist, M., Bilde, M., Glasius, M., and Ehn, M.: Formation and temperature dependence of highly oxygenated organic molecules (HOMs) from Δ^3-carene ozonolysis, Atmos. Chem. Phys., 24, 9459–9473, https://doi.org/10.5194/acp-24-9459-2024, 2024.

Matsunaga, A., and Ziemann, P. J. Gas-wall partitioning of organic compounds in a teflon film chamber and potential effects on reaction product and aerosol yield measurements. Aerosol Science and Technology, 44(10), 881–892. https://doi.org/10.1080/02786826.2010.501044, 2010.

McFiggans, G., Artaxo, P., Baltensperger, U., Coe, H., Facchini, M. C., Feingold, G., Fuzzi, S., Gysel, M., Laaksonen, A., Lohmann, U., Mentel, T. F., Murphy, D. M., O'Dowd, C. D., Snider, J. R., and Weingartner, E.: The effect of physical and chemical aerosol properties on warm cloud droplet activation, Atmos. Chem. Phys., 6, 2593–2649, https://doi.org/10.5194/acp-6-2593-2006, 2006.

McMurry, P. and Rader, D.: Aerosol wall losses in electrically charged chambers, Aerosol Sci. Tech., 4, 249–268, https://doi.org/10.1080/02786828508959054, 1985.

Mei, F., Setyan, A., Zhang, Q., and Wang, J.: CCN activity of organic aerosols observed downwind of urban emissions during CARES, Atmos. Chem. Phys., 13, 12155–12169, https://doi.org/10.5194/acp-13-12155-2013, 2013.

Moore, R., Nenes, A., and Medina, J.: Scanning Mobility CCN Analysis– A method for fast measurements of size resolved CCN distributions and activation kinetics, Aerosol Sci. Tech., 44, 861–871, DOI:10.1080/02786826.2010.498715, 2010.

Nannoolal, Y., Rarey, J., and Ramjugernath, D.: Estimation of pure component properties Part 3. Estimation of the vapour pressure of non-electrolyte organic compounds via group contributions and group interactions, Fluid Phase Equilibr., 269, 117–133, https://doi.org/10.1016/j.fluid.2008.04.020, 2008.

O'Meara, S. P., Xu, S., Topping, D., Alfarra, M. R., Capes, G., Lowe, D., Shao, Y., and McFiggans, G.: PyCHAM (v2.1.1): a Python box model for simulating aerosol chambers, Geosci. Model Dev., 14, 675–702, https://doi.org/10.5194/gmd-14-675-2021, 2021.

Pankow, J. F.: An absorption model of gas/particle partitioning involved in the formation of secondary organic aerosol, Atmos. Env., 28, 189–193, https://doi.org/10.1016/j.atmosenv.2007.10.060, 1994.

Peeters, J., L. Vereecken, and G. Fantechi.: The detailed mechanism of the OH-initiated atmospheric oxidation of α-pinene: A theoretical study, Phys. Chem. Chem. Phys., 3, 5489–5504, https://doi.org/10.1039/B106555F, 2001.

Petters, M. D. and Kreidenweis, S. M.: A single parameter representation of hygroscopic growth and cloud condensation nucleus activity, Atmos. Chem. Phys., 7, 1961–1971, https://doi.org/10.5194/acp-7-1961-2007, 2007.

Pichelstorfer, L., Pontus Roldin, Matti Rissanen, Noora Hyttinen, Olga Garmash, Carlton Xavier, Putian Zhou, Petri Clusius, Benjamin Foreback, Thomas Golin Almeida, Chenjuan Deng, Metin Baykara, Theo Kurten and Michael Boy.: Towards automated inclusion of autoxidation chemistry in models: from precursors to atmospheric implications, Environ. Sci.: Atmos., 4, 879-896, https://doi.org/10.1039/D4EA00054D, 2024.

Pun, B. K. and Seigneur, C.: Investigative modeling of new pathways for secondary organic aerosol formation, Atmos. Chem. Phys., 7, 2199–2216, https://doi.org/10.5194/acp-7-2199-2007, 2007.

Rohrer, F., Bohn, B., Brauers, T., Brüning, D., Johnen, F.-J., Wahner, A., and Kleffmann, J.: Characterisation of the photolytic HONO-source in the atmosphere simulation chamber SAPHIR, Atmos. Chem. Phys., 5, 2189–2201, https://doi.org/10.5194/acp-5-2189-2005, 2005.

Roldin, P., Ehn, M., Kurtén, T. et al.: The role of highly oxygenated organic molecules in the Boreal aerosol-cloud-climate system, Nat Commun, 10, 4370, https://doi.org/10.1038/s41467-019-12338-8, 2019.

Saunders, S. M., Jenkin, M. E., Derwent, R. G., and Pilling, M. J.: Protocol for the development of the Master Chemical Mechanism, MCM v3 (Part A): tropospheric degradation of non-aromatic volatile organic compounds, Atmos. Chem. Phys., 3, 161–180, https://doi.org/10.5194/acp-3-161-2003, 2003.

Seinfeld, J. H., & Pandis, S. N.: Atmospheric chemistry and physics: From air pollution to climate change (3rd ed.), Wiley, ISBN: 978-1-118-94740-1, 2016.

Shrivastava, M., Cappa, C. D., Fan, J., Goldstein, A. H., Guenther, A. B., Jimenez, J. L., Kuang, C., Laskin, A., Martin, S. T., Ng, N. L., Petaja, T., Pierce, J. R., Rasch, P. J., Roldin, P., Seinfeld, J. H., Shilling, J., Smith, J. N., Thornton, J. A., Volkamer, R., Wang, J., Worsnop, D. R., Zaveri, R. A., Zelenyuk, A., and Zhang, Q.: Recent advances in understanding secondary organic aerosol: Implications for global climate forcing, Rev. Geophys., 55, 509–559, https://doi.org/10.1002/2016RG000540, 2017.

Thomsen, D., Iversen, E. M., Skønager, J. T., Luo, Y., Li, L., Roldin, P., Priestley, M., Pedersen, H. B., Hallquist, M., and Ehn, M.: The effect of temperature and relative humidity on secondary organic aerosol formation from ozonolysis of Δ^3-carene, Environmental Science: Atmospheres, 4, 88–103, https://doi.org/10.1039/D3EA00128H, 2024.

Topping, D., and Bane, M.: Introduction to aerosol modelling: From theory to code, Wiley, DOI:10.1002/9781119625728, 2022.

Topping, D., Barley, M., Bane, M. K., Higham, N., Aumont, B., Dingle, N., and McFiggans, G.: UManSysProp v1.0: an online and open-source facility for molecular property prediction and atmospheric aerosol calculations, Geosci. Model Dev., 9, 899–914, https://doi.org/10.5194/gmd-9-899-2016, 2016.

Topping, D., Connolly, P., and Reid, J.: PyBOX: An automated box-model generator for atmospheric chemistry and aerosol simulations, J. Open Source Software, 3, 28, https://doi.org/10.21105/joss.00755, 2018.

Valorso, R., Aumont, B., Camredon, M., Raventos-Duran, T., Mouchel-Vallon, C., Ng, N. L., Seinfeld, J. H., Lee-Taylor, J., and Madronich, S.: Explicit modelling of SOA formation from α-pinene photooxidation: sensitivity to vapour pressure estimation, Atmos. Chem. Phys., 11, 6895–6910, https://doi.org/10.5194/acp-11-6895-2011, 2011.

Wang, J., Shilling, J. E., Liu, J., Zelenyuk, A., Bell, D. M., Petters, M. D., Thalman, R., Mei, F., Zaveri, R. A., and Zheng, G.: Cloud droplet activation of secondary organic aerosol is mainly controlled by molecular weight, not water solubility, Atmos. Chem. Phys., 19, 941–954, https://doi.org/10.5194/acp-19-941-2019, 2019.

Xia, A. G., D. V. Michelangeli, and P. A. Makar.: Box model studies of the secondary organic aerosol formation under different HC/NO_x conditions using the subset of the Master Chemical Mechanism for α-pinene oxidation, J. Geophys. Res., 113, D10301, doi:10.1029/2007JD008726, 2008.

Xia, Z., Zhao, C., Yang, Z., Du, Q., Feng, J., Jin, C., Shi, J., and An, H.: Toward a learnable Artificial Intelligence Model for Aerosol Chemistry and Interactions (AIMACI) based on the Multi-Head Self-Attention algorithm, Atmos. Chem. Phys., 25, 6197–6218, https://doi.org/10.5194/acp-25-6197-2025, 2025.

Xu, J. L.: Simulated impact of NO_x on SOA formation from oxidation of toluene and m-xylene, M.S. thesis, Rice University, USA, 2014.

Xu, S. X.: Investigating the role of highly oxygenated molecules (HOM) in aerosol using a newly developed box model PyCHAM, Ph.D. thesis, University of Manchester, UK, 2021.

Yu, F. and Luo, G.: Simulation of particle size distribution with a global aerosol model: contribution of nucleation to aerosol and CCN number concentrations, Atmos. Chem. Phys., 9, 7691–7710, https://doi.org/10.5194/acp-9-7691-2009, 2009.

Zaveri, R., Easter, R., Fast, J., and Peters, L.: Model for Simulating Aerosol Interactions and Chemistry (MOSAIC), J. Geophys. Res., 113, D13204, https://doi.org/10.1029/2007JD008782, 2008.

Zhang, C., Guo, Y., Shen, H., Luo, H., Pullinen, I., Schmitt, S. H., et al.: Contrasting influence of nitrogen oxides on the cloud condensation nuclei activity of monoterpene-derived secondary organic aerosol in daytime and nighttime oxidation, Geophys. Res. Lett., 50, e2022GL102110, https://doi.org/10.1029/2022GL102110, 2023.

Zhang, X., Cappa, C.D., Jathar, S.H., McVay, R.C., Ensberg, J.J., Kleeman, M.J., and Seinfeld, J.H. Influence of vapor wall loss in laboratory chambers on yields of secondary organic aerosol, Proc. Natl. Acad. Sci. U.S.A. 111 (16) 5802-5807, https://doi.org/10.1073/pnas.1404727111, 2014.

Zhao, D. F., A. Buchholz, B. Kortner, P. Schlag, F. Rubach, A. Kiendler-Scharr, R. Tillmann, A. Wahner, J. M. Flores, Y. Rudich, et al.: Size-dependent hygroscopicity parameter (κ) and chemical composition of secondary organic cloud condensation nuclei, Geophys. Res. Lett., 42, 10,920–10,928, https://doi:10.1002/2015GL066497, 2015a.

Zhao, D. F., Buchholz, A., Kortner, B., Schlag, P., Rubach, F., Fuchs, H., Kiendler-Scharr, A., Tillmann, R., Wahner, A., Watne, Å. K., Hallquist, M., Flores, J. M., Rudich, Y., Kristensen, K., Hansen, A. M. K., Glasius, M., Kourtchev, I., Kalberer, M., and Mentel, Th. F.: Cloud condensation nuclei activity, droplet growth kinetics, and hygroscopicity of biogenic and anthropogenic secondary organic aerosol (SOA), Atmos. Chem. Phys., 16, 1105–1121, https://doi.org/10.5194/acp-16-1105-2016, 2016.

Zhao, D. F., Kaminski, M., Schlag, P., Fuchs, H., Acir, I.-H., Bohn, B., Häseler, R., Kiendler-Scharr, A., Rohrer, F., Tillmann, R., Wang, M. J., Wegener, R., Wildt, J., Wahner, A., and Mentel, Th. F.: Secondary organic aerosol formation from hydroxyl radical oxidation and ozonolysis of monoterpenes, Atmos. Chem. Phys., 15, 991–1012, https://doi.org/10.5194/acp-15-991-2015, 2015b.

Zhao, J., Häkkinen, E., Graeffe, F., Krechmer, J. E., Canagaratna, M. R., Worsnop, D. R., Kangasluoma, J., and Ehn, M.: A combined gas- and particle-phase analysis of highly oxygenated organic molecules (HOMs) from α-pinene ozonolysis, Atmos. Chem. Phys., 23, 3707–3730, https://doi.org/10.5194/acp-23-3707-2023, 2023.

Zuend, A. and Seinfeld, J. H.: Modeling the gas-particle partitioning of secondary organic aerosol: the importance of liquid-liquid phase separation, Atmos. Chem. Phys., 12, 3857–3882, https://doi.org/10.5194/acp-12-3857-2012, 2012.

Supplement of

~~Explicit~~Process-level simulation of chemical composition, size distribution and cloud condensation nuclei of secondary organic aerosol from α-pinene ozonolysis

Zhen Song[1,2,3,4], Chenqi Zhang[1], Hongru Shen[1,†], Hao Ma[1], Iida Pullinen[6,‡], Defeng Zhao[1,3,4,5]

[1]Department of Atmospheric and Oceanic Sciences & Institute of Atmospheric Sciences, Fudan University, Shanghai, China

[2]Shanghai Frontiers Science Center of Atmosphere-Ocean Interaction, Fudan University, Shanghai, 200438, China

[3]Shanghai Key Laboratory of Ocean-land-atmosphere Boundary Dynamics and Climate Change, Fudan University, Shanghai, 200438, China

[4]National Observations and Research Station for Wetland Ecosystems of the Yangtze Estuary, Fudan University, Shanghai, 200438, China

[5]Institute of Eco-Chongming (IEC), 1050 Baozhen, Lühua Town, Chongming District, Shanghai 202151, China

[6]Institute of Energy and Climate Research, IEK-8: Troposphere, Forschungszentrum Jülich, Jülich, Germany

[†]Present address: Department of Chemical Engineering and Applied Chemistry/Department of Chemistry, University of Toronto, Toronto, Ontario M5S 3E5, Canada

[‡] Present address: Department of Applied Physics, University of Eastern Finland, Kuopio, 70210, Finland

Correspondence to: Defeng Zhao (dfzhao@fudan.edu.cn)

Contents of this file

~~**Table S1: The simulated hygroscopicity parameter (κ) of SOA calculated by different chemical composition and corresponding particle size (nm).**~~

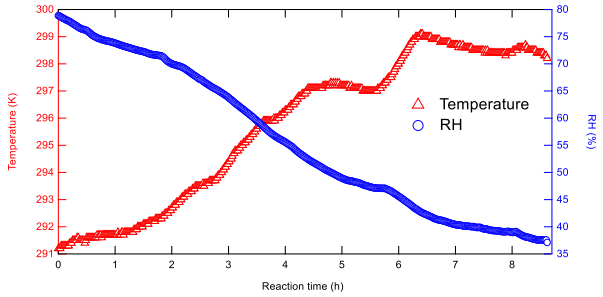

In the Supplement, additional figures (S1-S23) and tables (S1-S2) are provided.

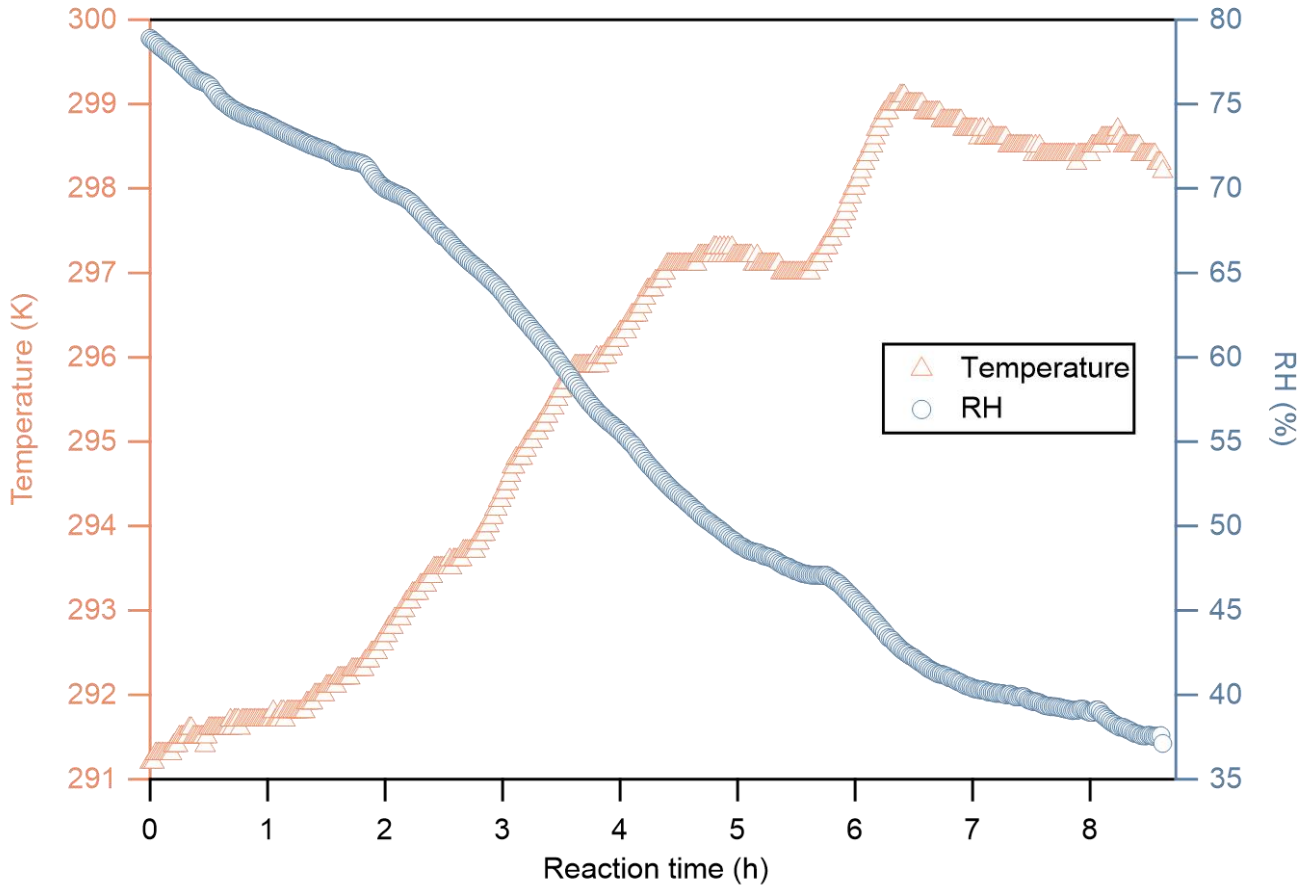

Figure S1: ~~The time~~Time evolution of measured temperature (~~Unit:~~ K) and relative humidity (RH; %) during the ~~experiment of~~dark α-pinene ozonolysis ~~in the dark~~experiment.

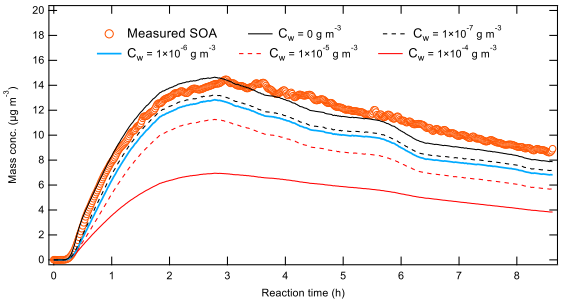

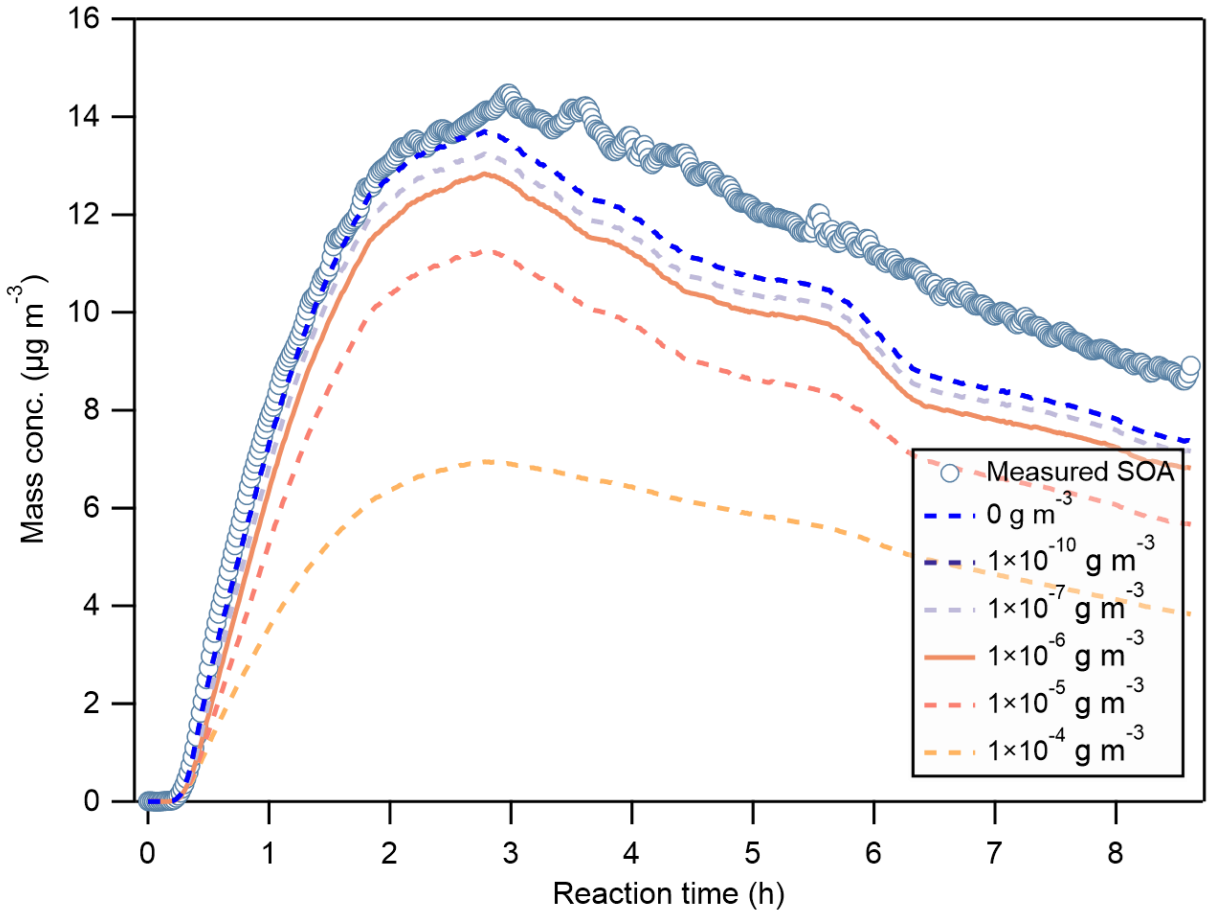

Figure S2: ~~The sensitivity~~Sensitivity of SOA mass concentration to the parameter C_w, which represents the effective absorbing wall mass concentration (g m^{-3}). This study adopts $C_w = 1 \times 10^{-6}$ g m^{-3}.

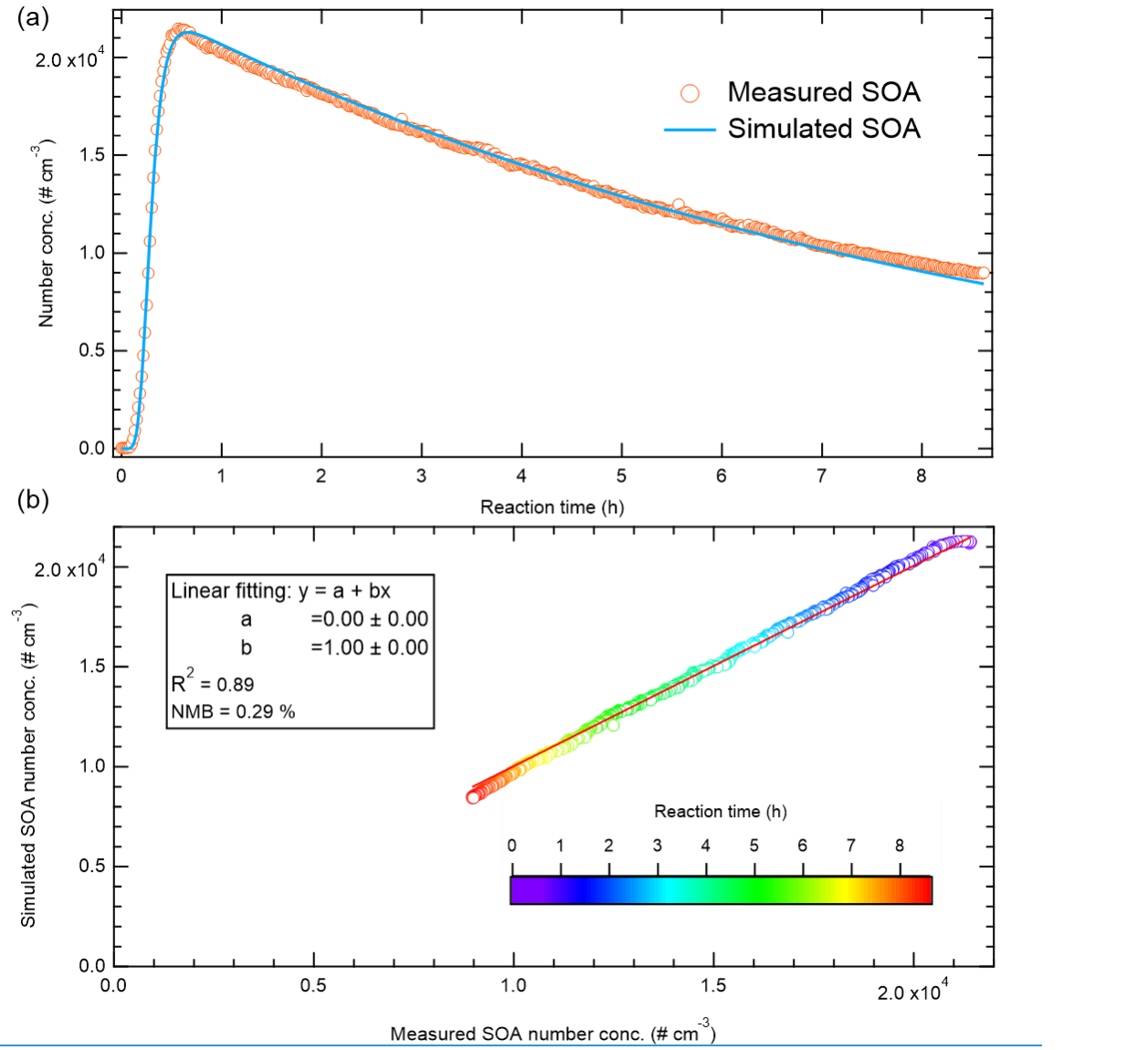

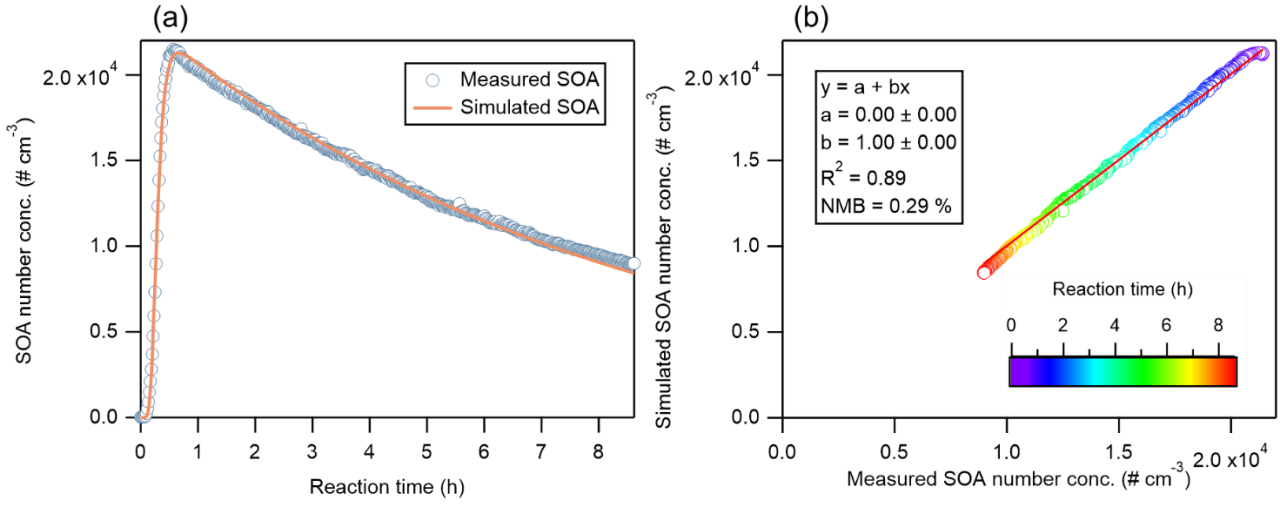

Figure S3: (a) Simulated (line) and measured (circles) SOA number concentrations (# cm^{-3}) ~~when setting~~using the nucleation parameters. (b) ~~Scatter plot~~Scatterplot of measured versus simulated SOA number concentrations, with a linear fit (red line). The coefficients a and b represent the intercept and slope, respectively, and R^2 denotes the correlation coefficient. Colors indicate the reaction time ~~of~~during the experiment. Note that the linear ~~fitting~~regression is constrained through the origin~~, and.~~ NMB refers to normalized mean bias. ~~Scatters~~Data points from the initial 0.57 ~~hours were~~h are excluded~~, as~~ because the number concentration during this period was fitted to CPC measurements and therefore assumed to match measurements ~~perfectly. Note that the coagulation~~exactly. Coagulation is excluded from the simulation.

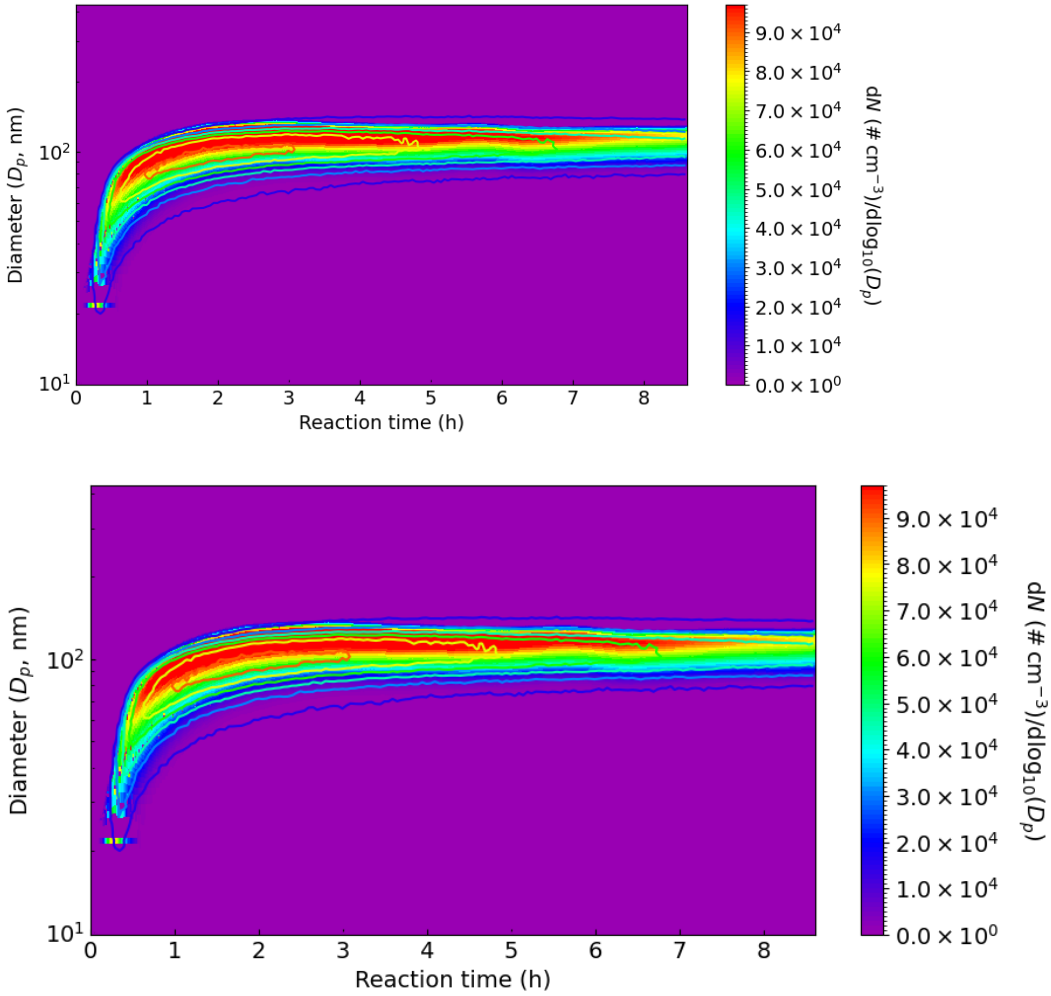

Figure S4: ~~The time~~Time evolution of the number size distributions (dN/dlog$_{10}$D$_p$) ~~of~~for measured (contour lines) and simulated (shaded areas) SOA ~~when setting~~using the nucleation parameters. ~~Note that the coagulation~~Coagulation is excluded from the simulation.

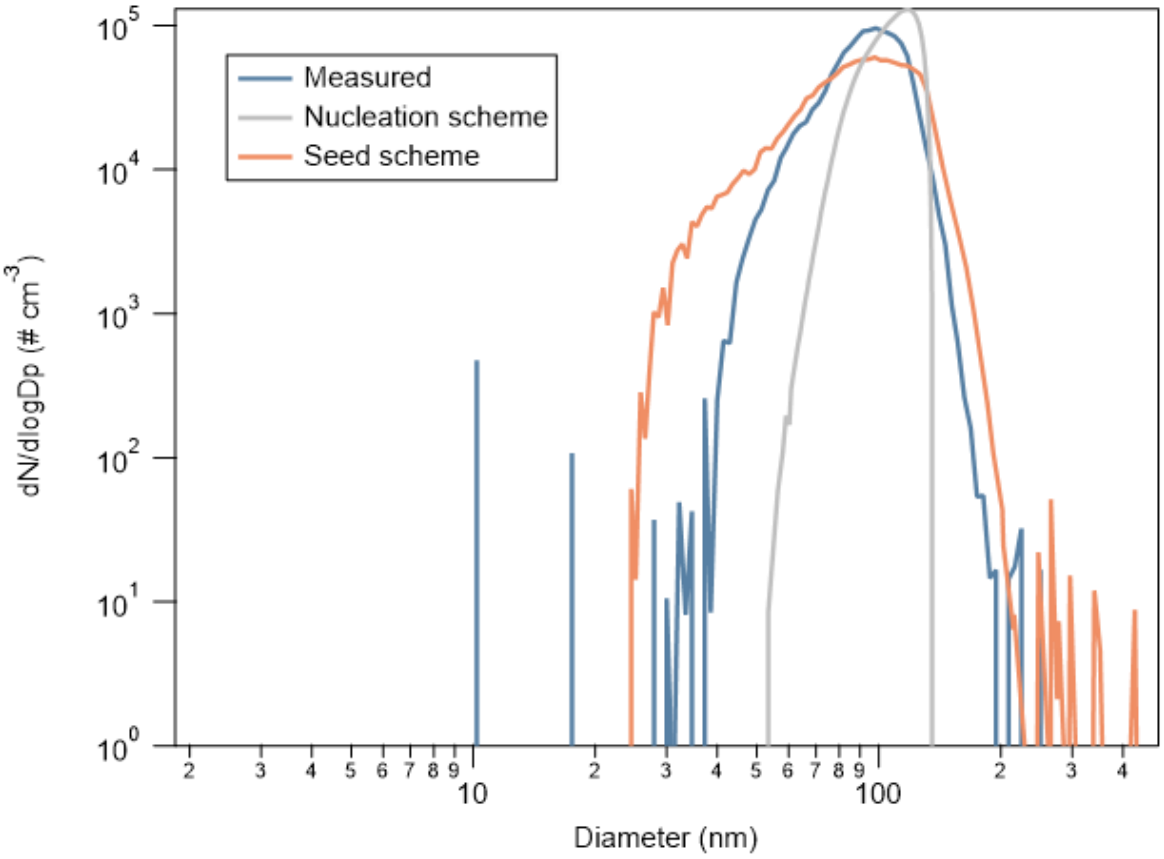

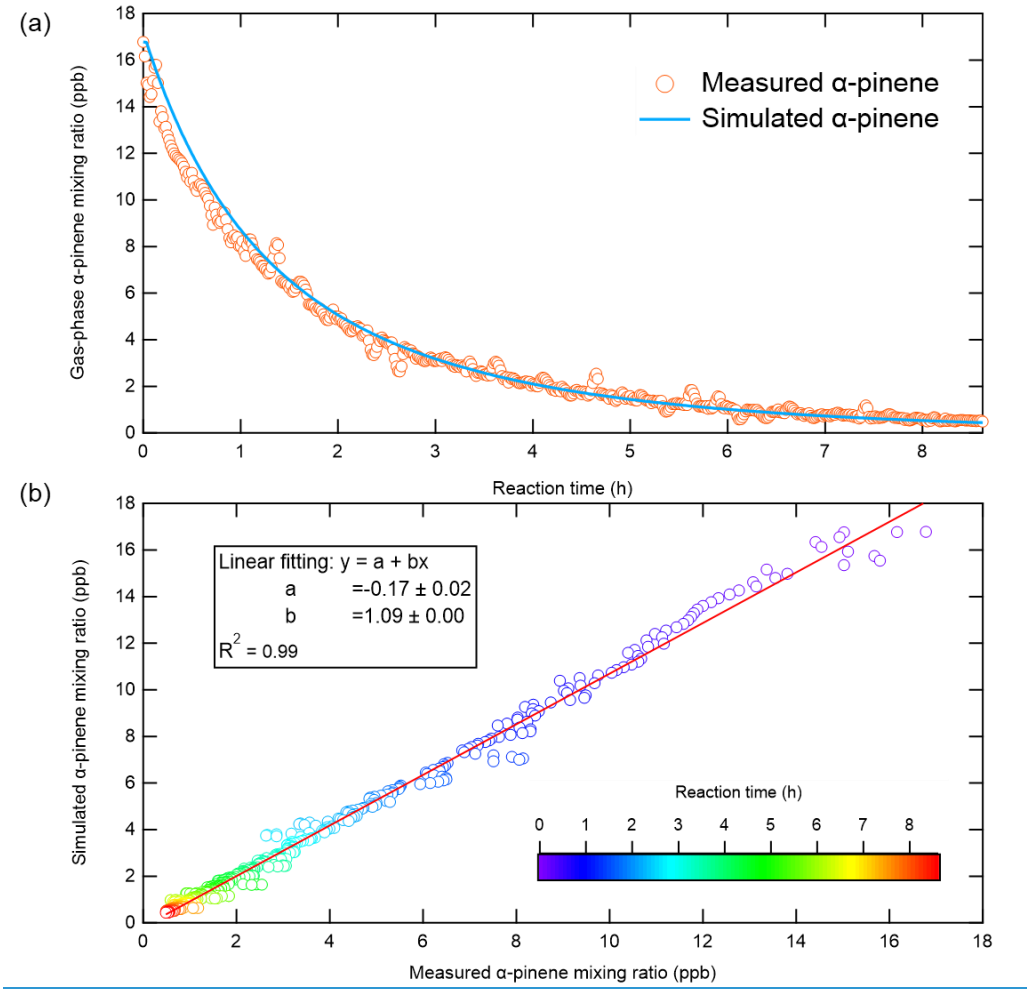

~~Figure S5: (a) The time~~

Fig. S5: Measured and simulated (by nucleation or seed schemes) particle size distribution ($dN/dlogD_p$) at the reaction time of 2 h.

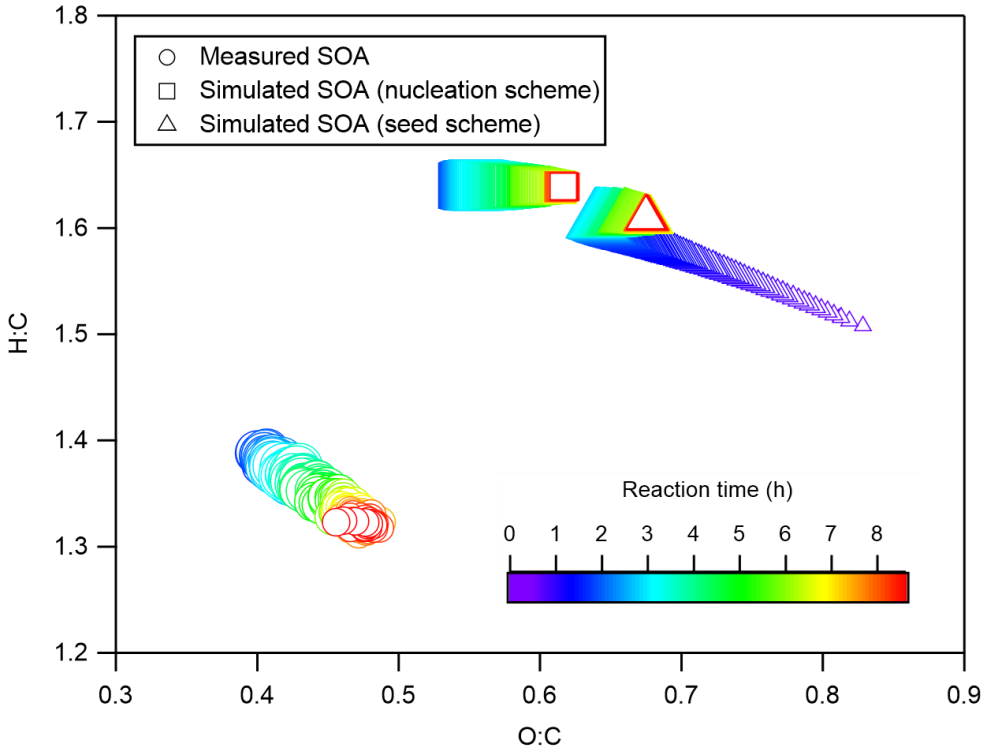

Figure S6: O:C and H:C ratios for measured (circles) and simulated SOA using the nucleation scheme (squares) or seed scheme (triangles).

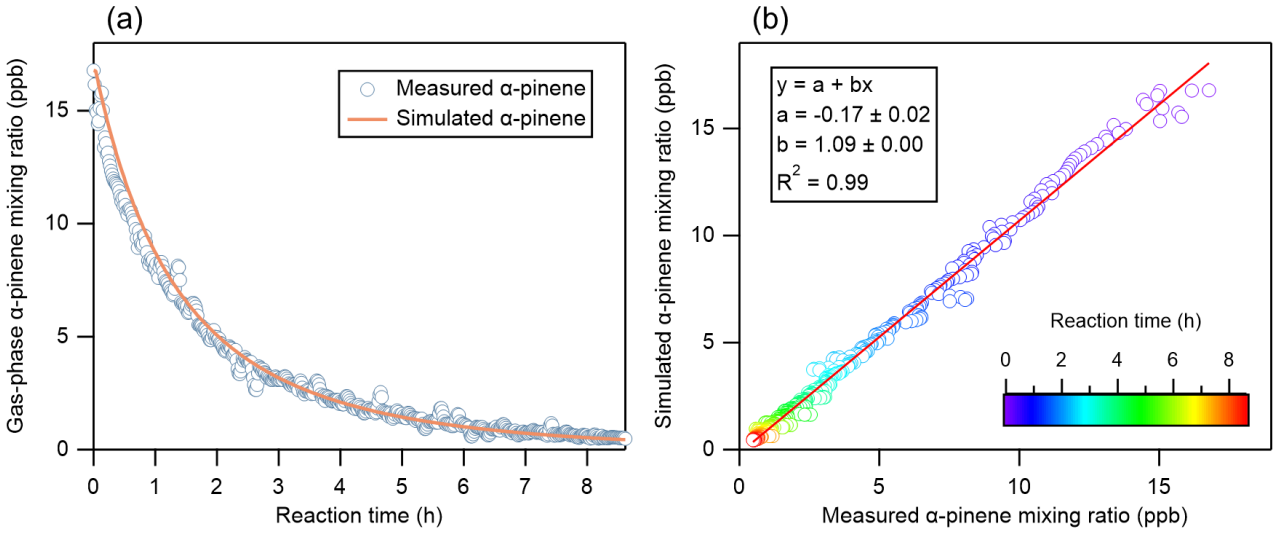

Figure S7: (a) Time evolution of the measured (circles) and simulated (line) gas-phase α-pinene mixing ratio (ppb). (b) ~~Scatter plot~~Scatterplot of measured versus simulated α-pinene concentrations, with a linear fit (red line). The coefficients a and b represent the intercept and slope, respectively, and R^2 denotes the correlation coefficient. Colors indicate the reaction time ~~of~~during the experiment.

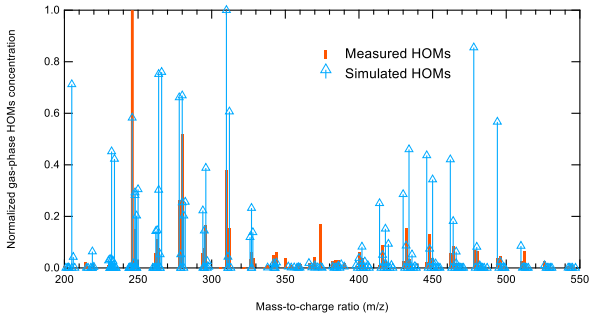

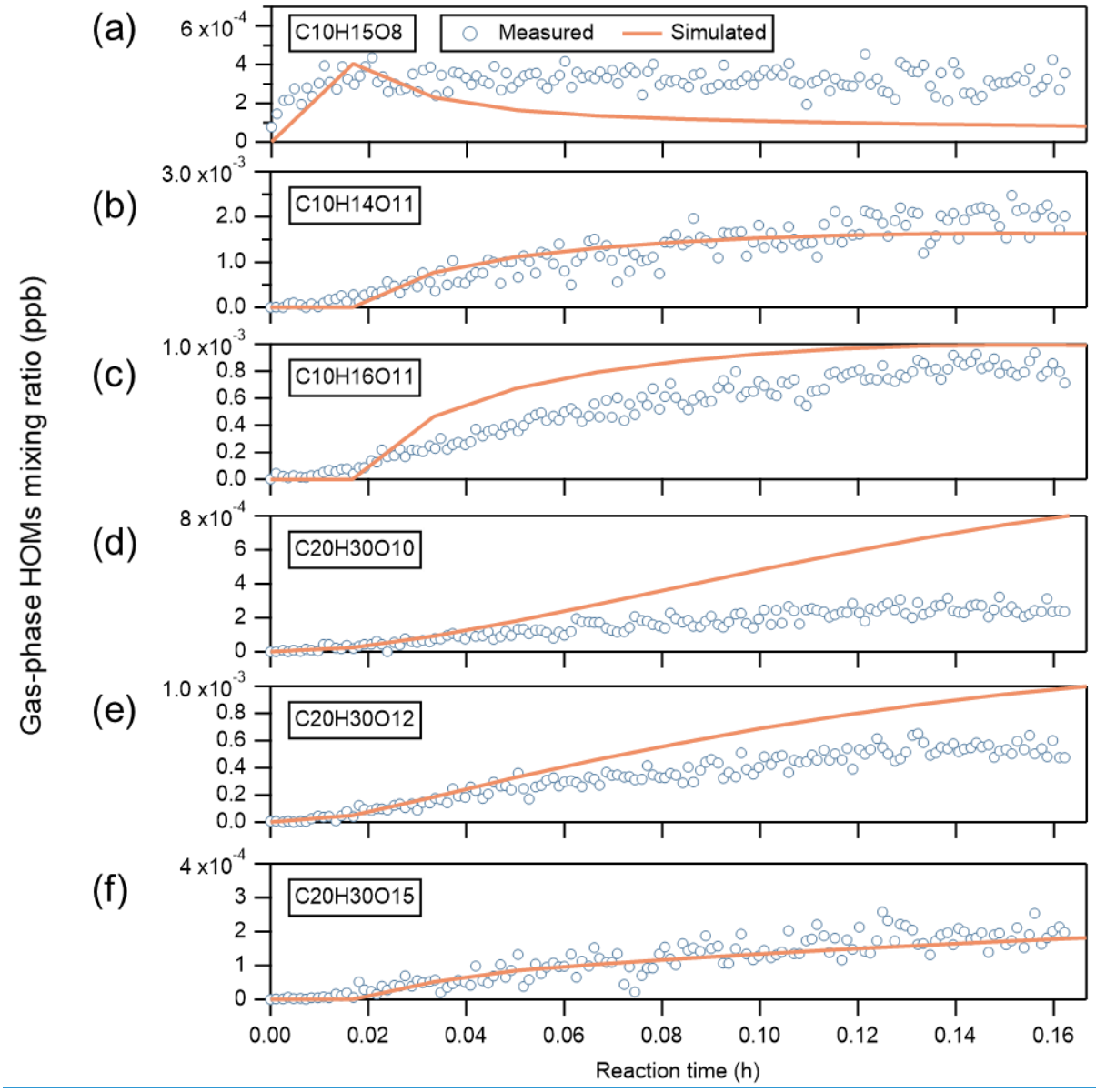

Figure ~~S6~~S8: (a-f) Time evolution of the measured (circles) and simulated (lines) gas-phase HOMs mixing ratio (ppb) during the initial 10 min of reaction.

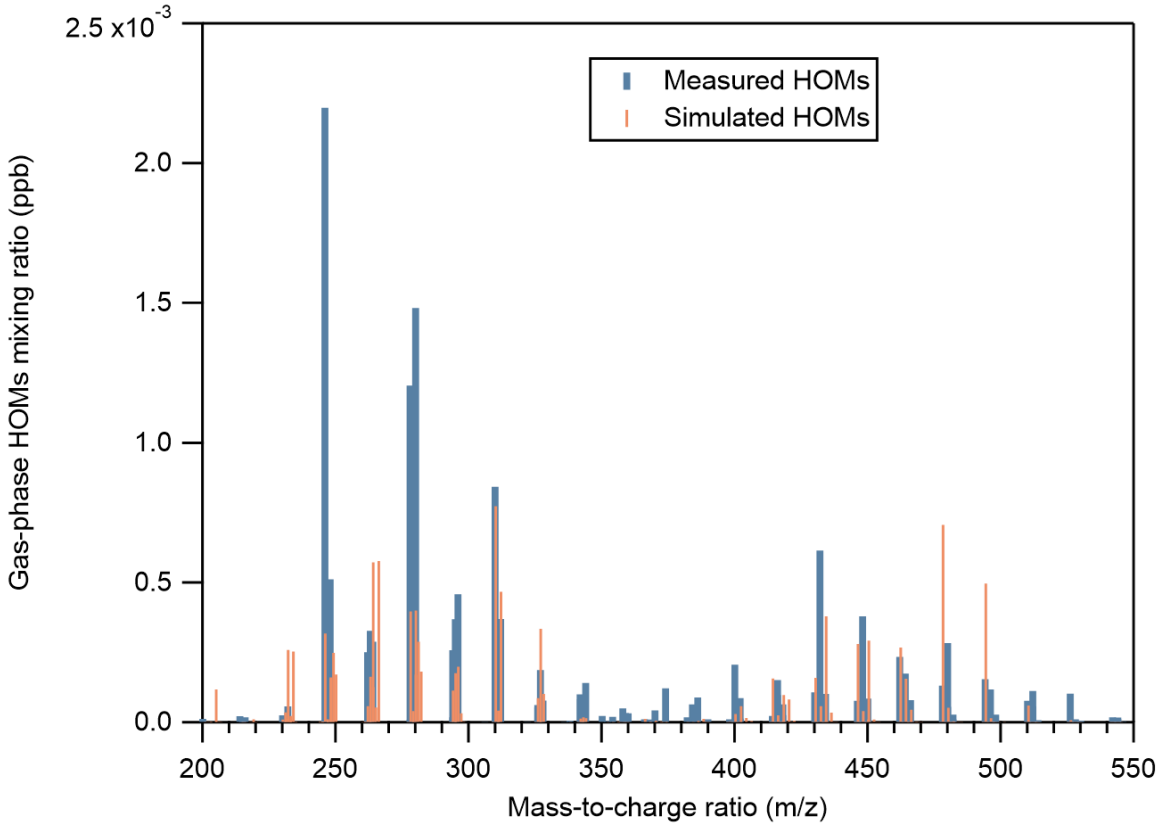

Figure S9: Measured and simulated gas-phase HOMs mass spectra averaged over the first ~~10 minutes~~5 min of experiment, during which gas-phase HOMs ~~were rapidly~~ accumulated rapidly and particle-phase concentrations ~~were~~remained low.

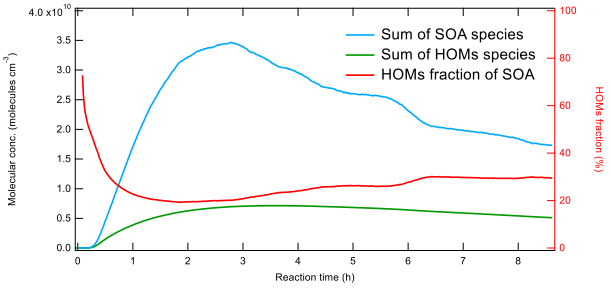

~~Figure S7: The time~~

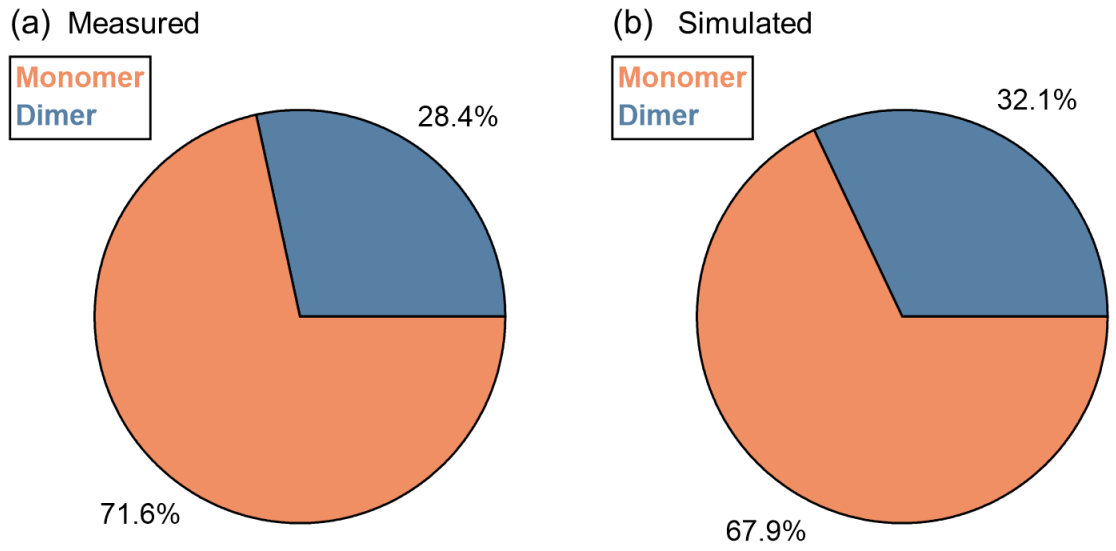

Figure S10: (a) Measured and (b) simulated fractions of HOMs monomers and dimers averaged over the first 5 min of experiment.

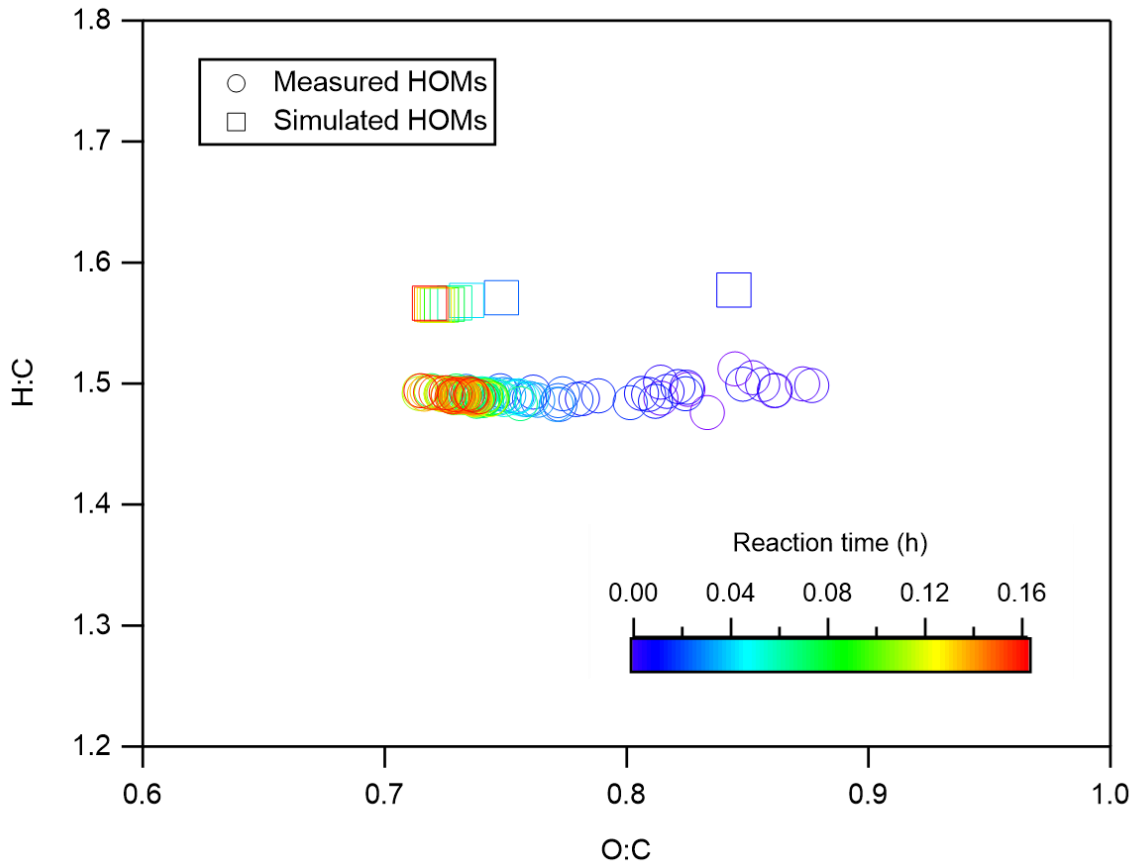

Figure S11: O:C and H:C ratios for measured (circles) and simulated (squares) gas-phase HOMs within the first 10 min of the experiment.

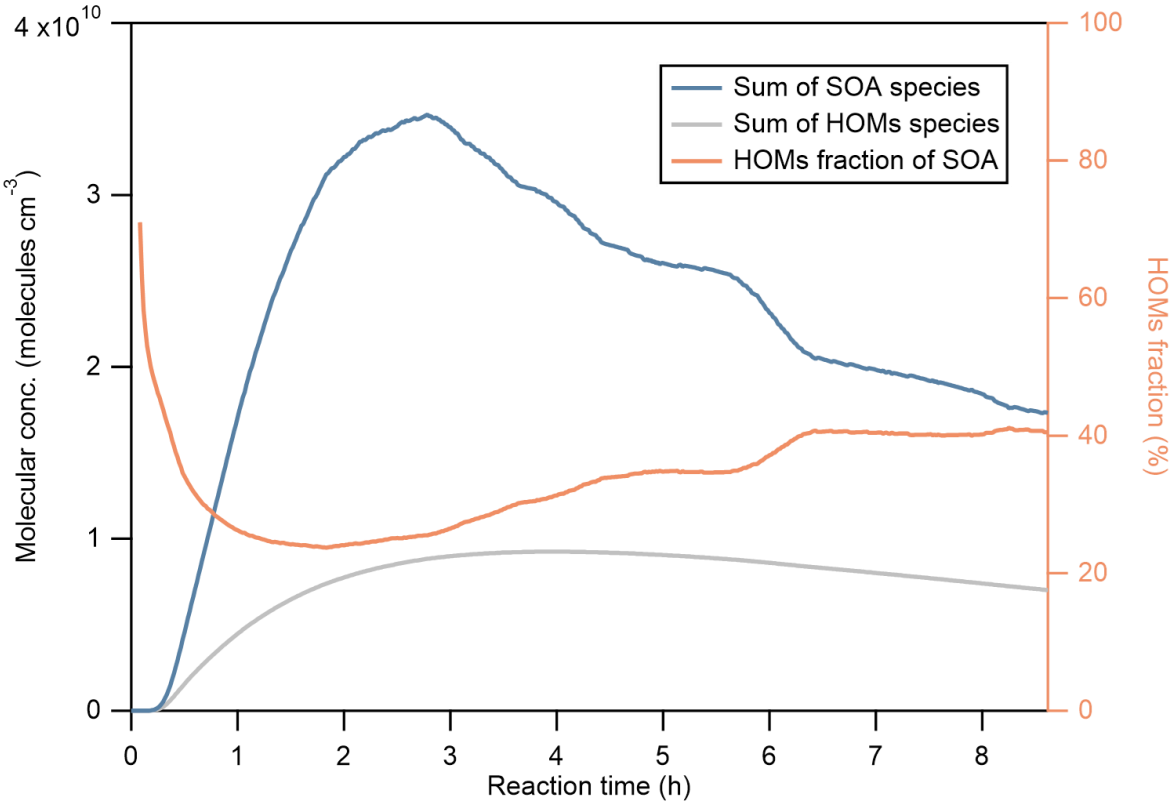

Figure S12: Time evolution of total molecular concentrations (molecules cm^{-3}) of simulated SOA and HOMs species, ~~and~~along with the HOMs fraction (%) of total SOA.

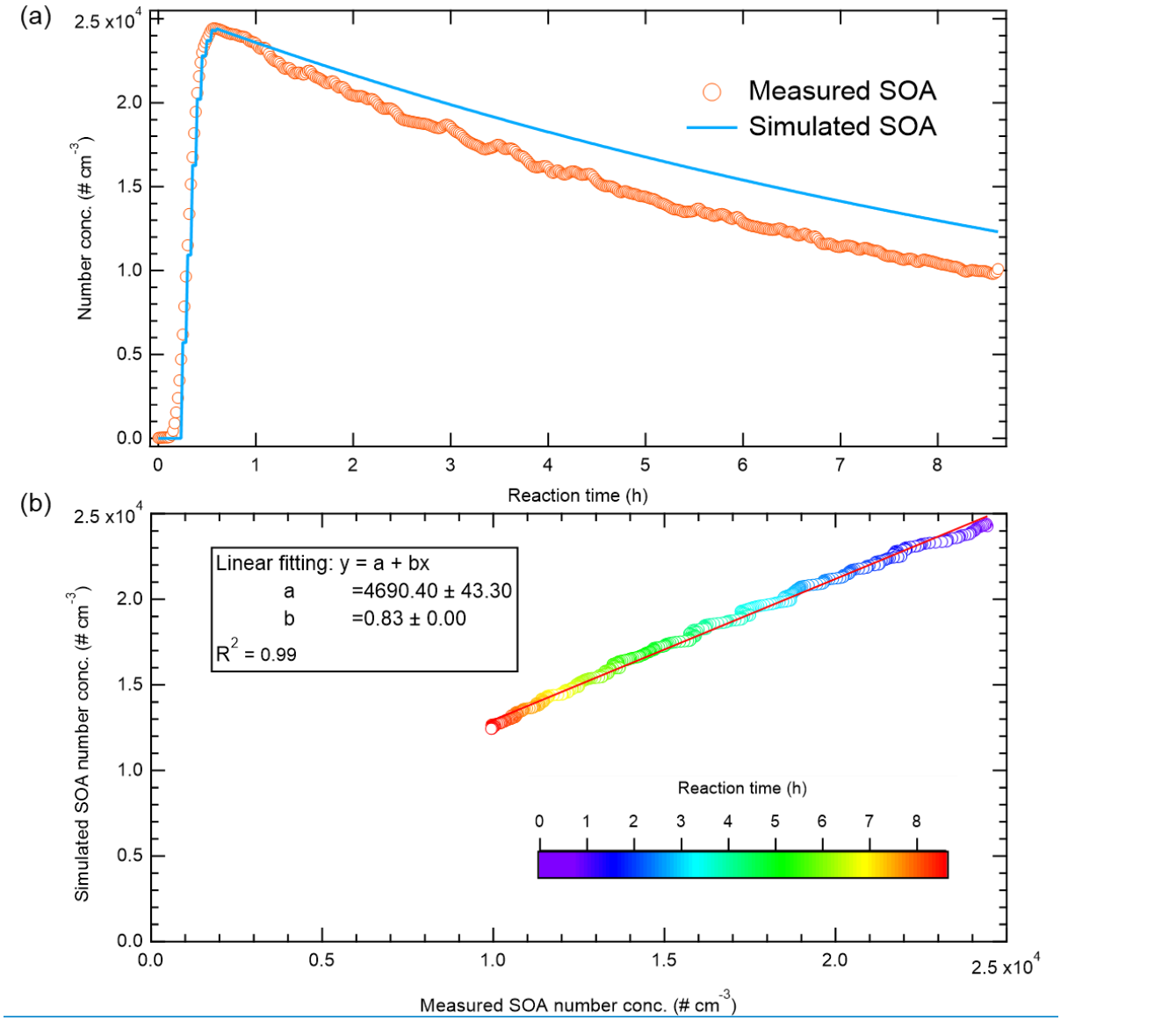

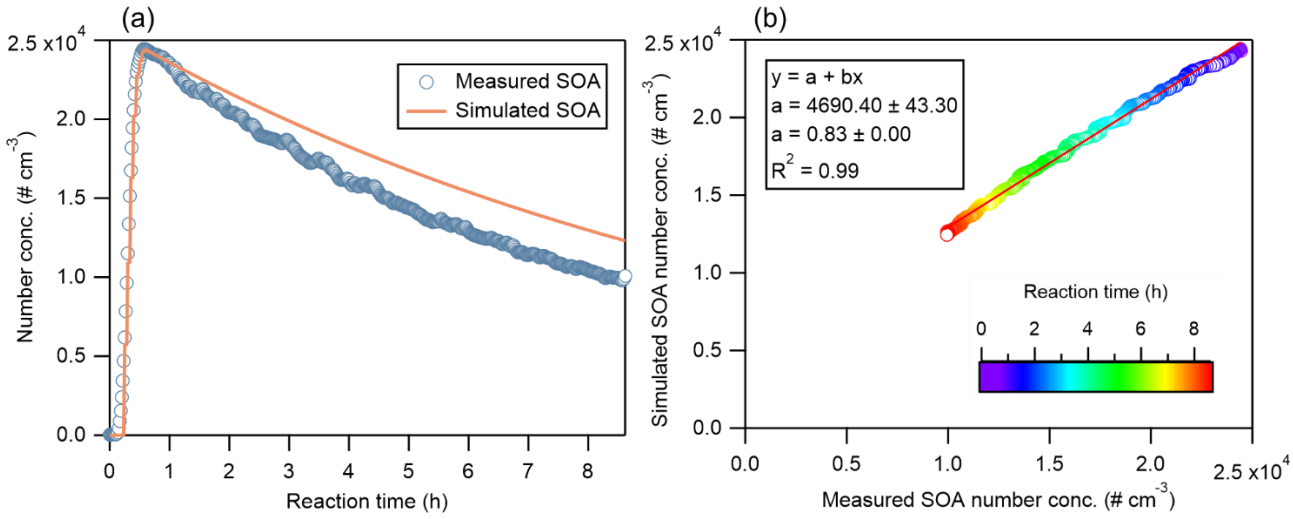

Figure ~~S8~~S13: (a) Simulated (line) and measured (circles) SOA number concentrations (# cm^{-3}) ~~when constraining size distribution of~~using the SMPS-constrained seed ~~particle~~scheme and ~~not considering~~excluding coagulation. (b) ~~Scatter plot~~Scatterplot of measured versus simulated SOA number concentrations, with a linear fit (red line). ~~Scatters~~Data points from the initial 0.6 ~~hours were~~h are excluded~~, as~~ because the number concentration during this period was fitted to the SMPS measurements.

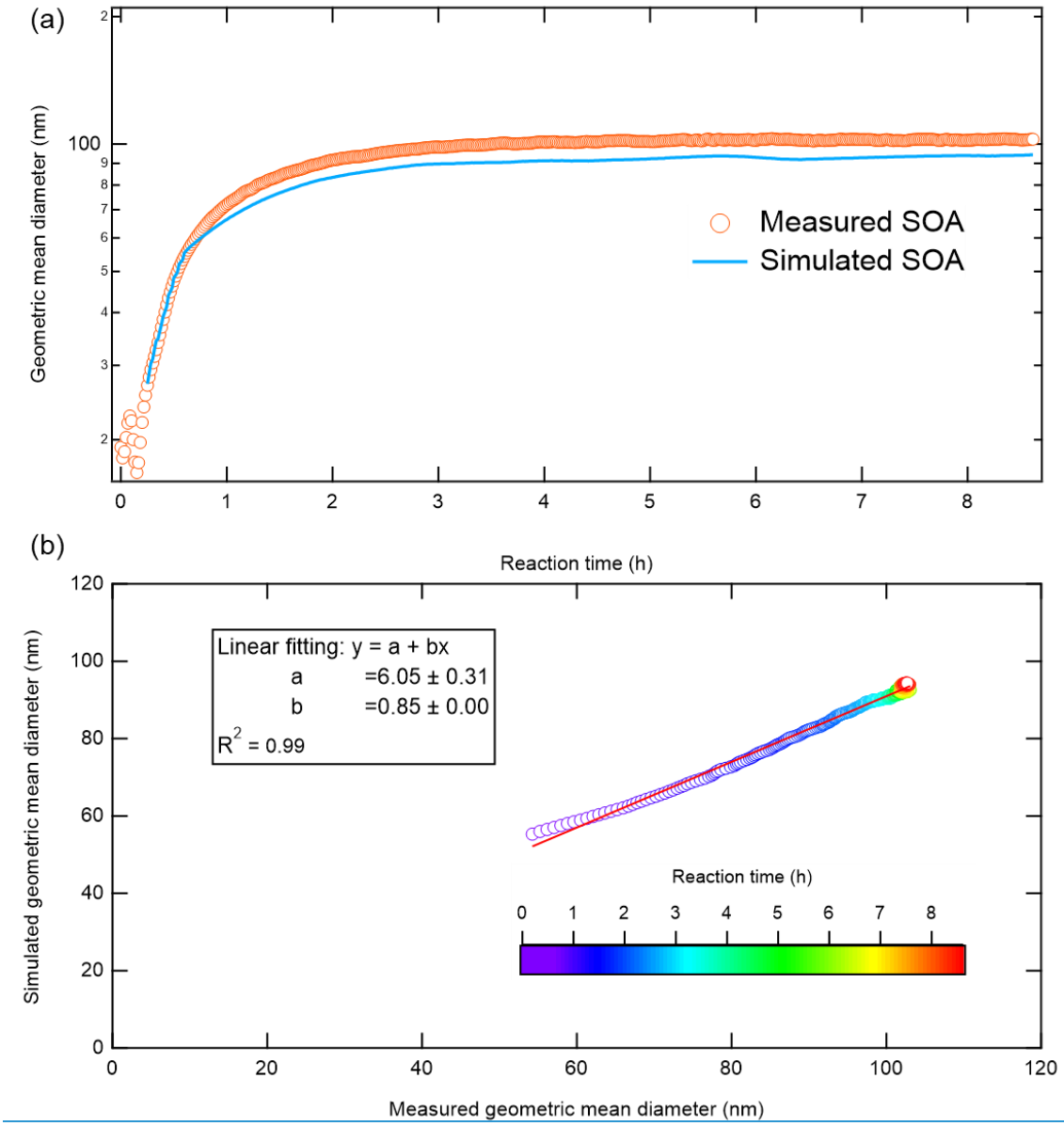

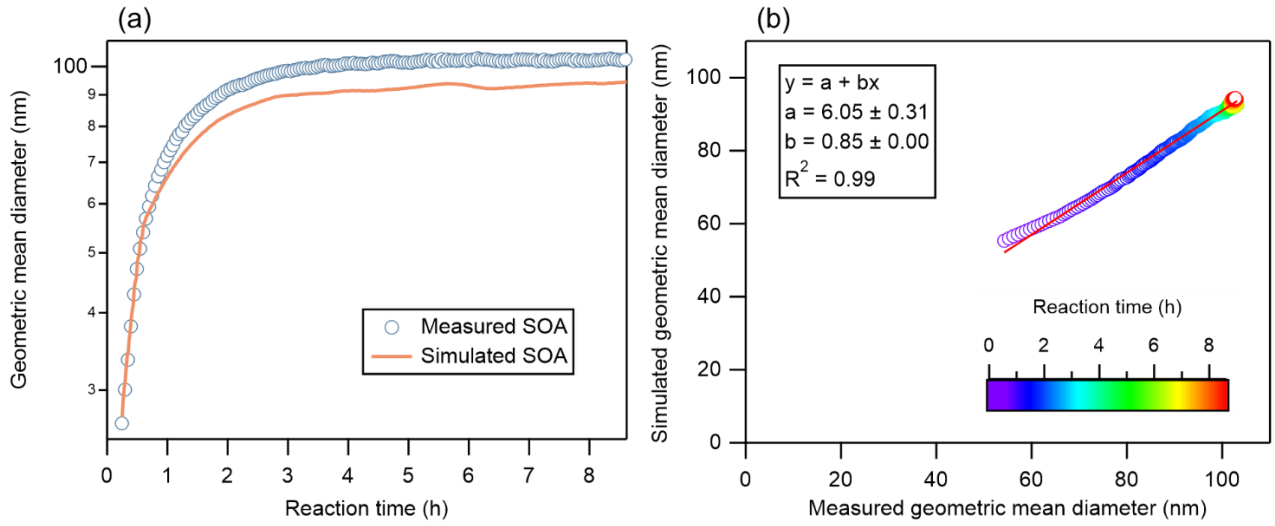

85 **Figure ~~S9~~S14: (a-b) Same as Fig. ~~S8~~S13, but for the geometric mean diameter (nm) of SOA. ~~Note that the coagulation~~Coagulation is ~~not considered, and scatters~~excluded. Data points from the initial 0.6 ~~hours were~~h are excluded ~~as particle size distribution~~because PSD during this period was fitted to the SMPS measurements.**

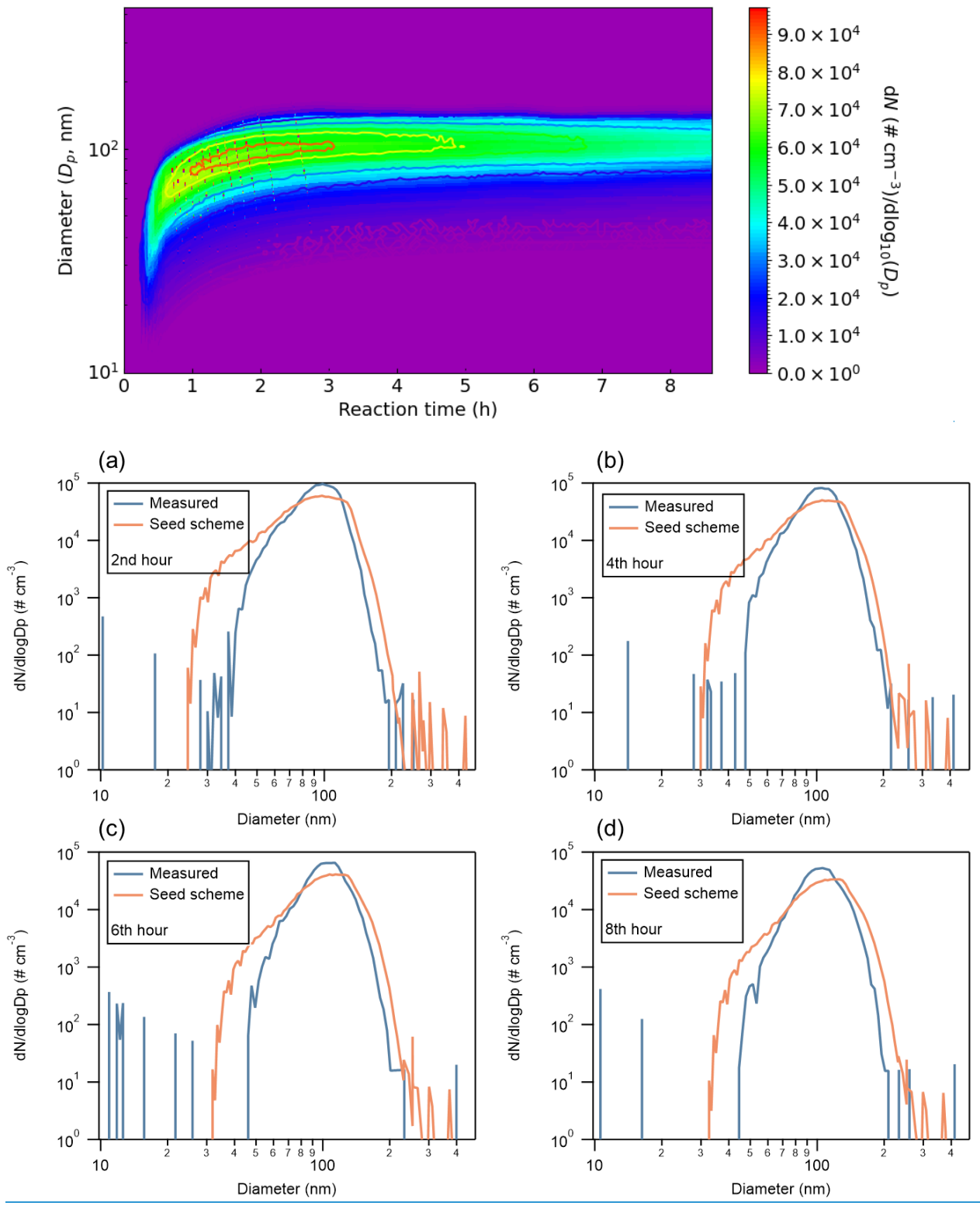

90 **Figure ~~S10: The time~~ S15: (a-d) Number particle size distribution (dN/dlog$_{10}$D$_p$) at reaction hours 2, 4, 6, and 8.**

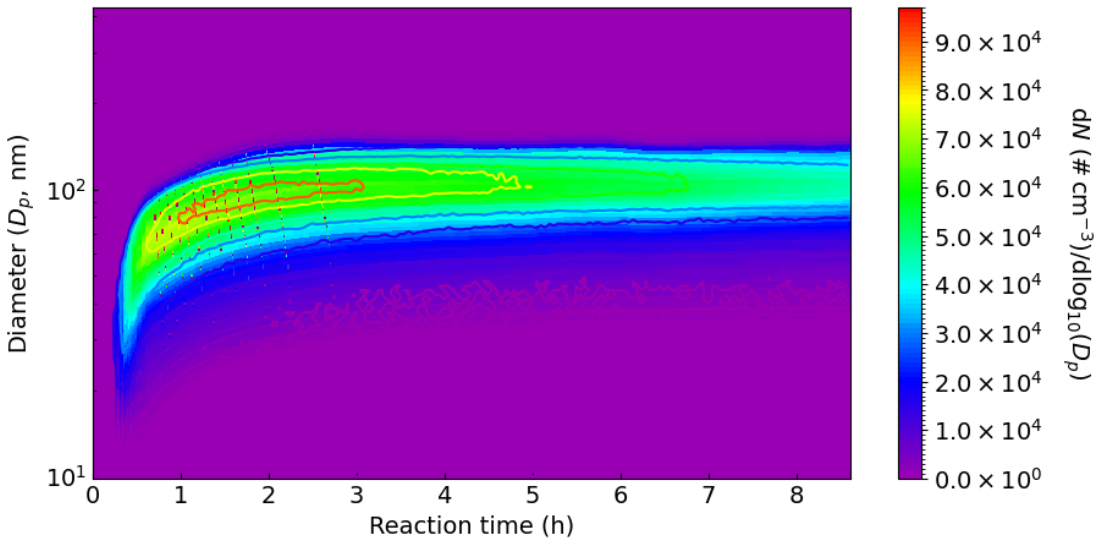

Figure S16: Time evolution of the number size distributions ($dN/dlog_{10}D_p$) ~~of~~for measured (contour lines) and simulated (shaded areas) SOA. Coagulation is excluded in the ~~case of not considering coagulations~~simulation.

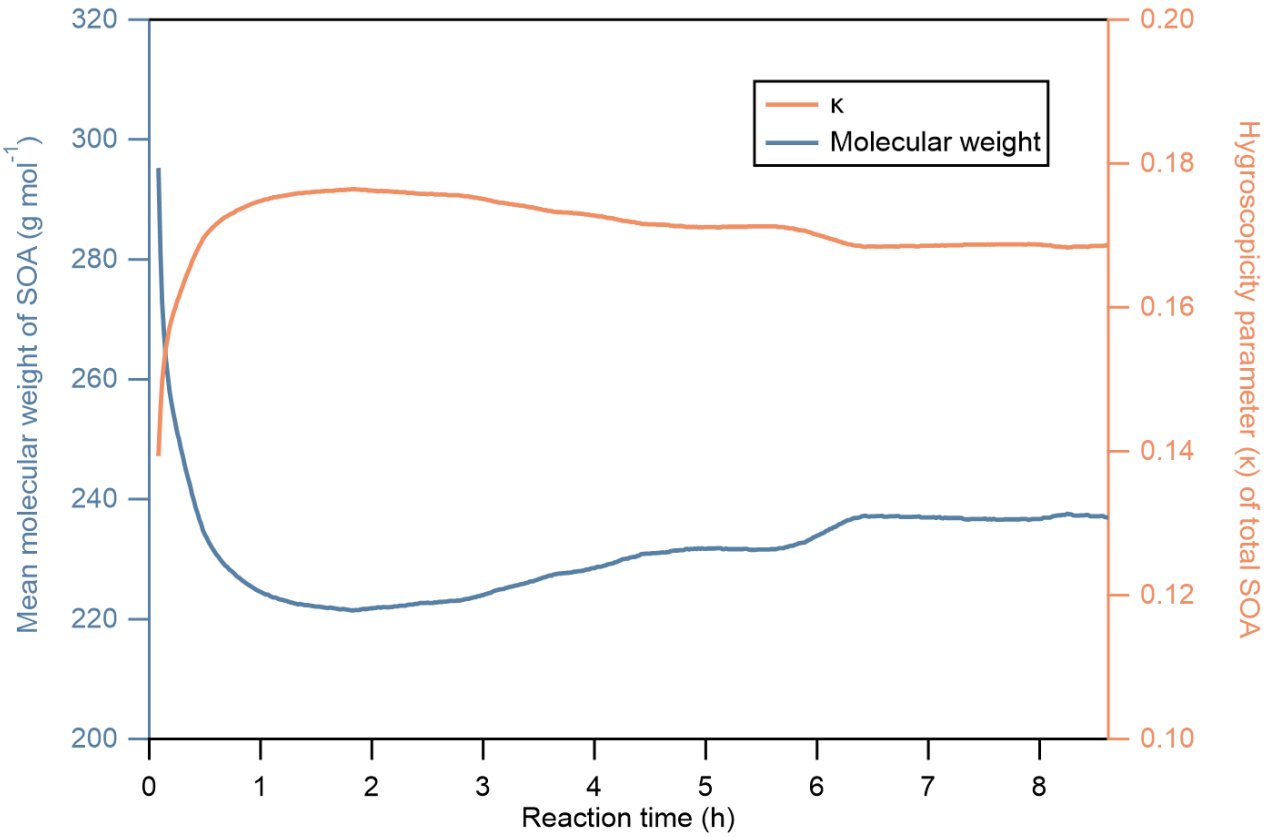

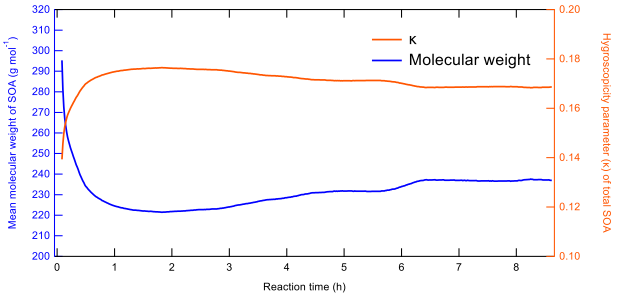

95

Figure ~~S11: The time~~S17: Time evolution of the mean molecular weight and hygroscopicity parameter (κ) of simulated SOA.

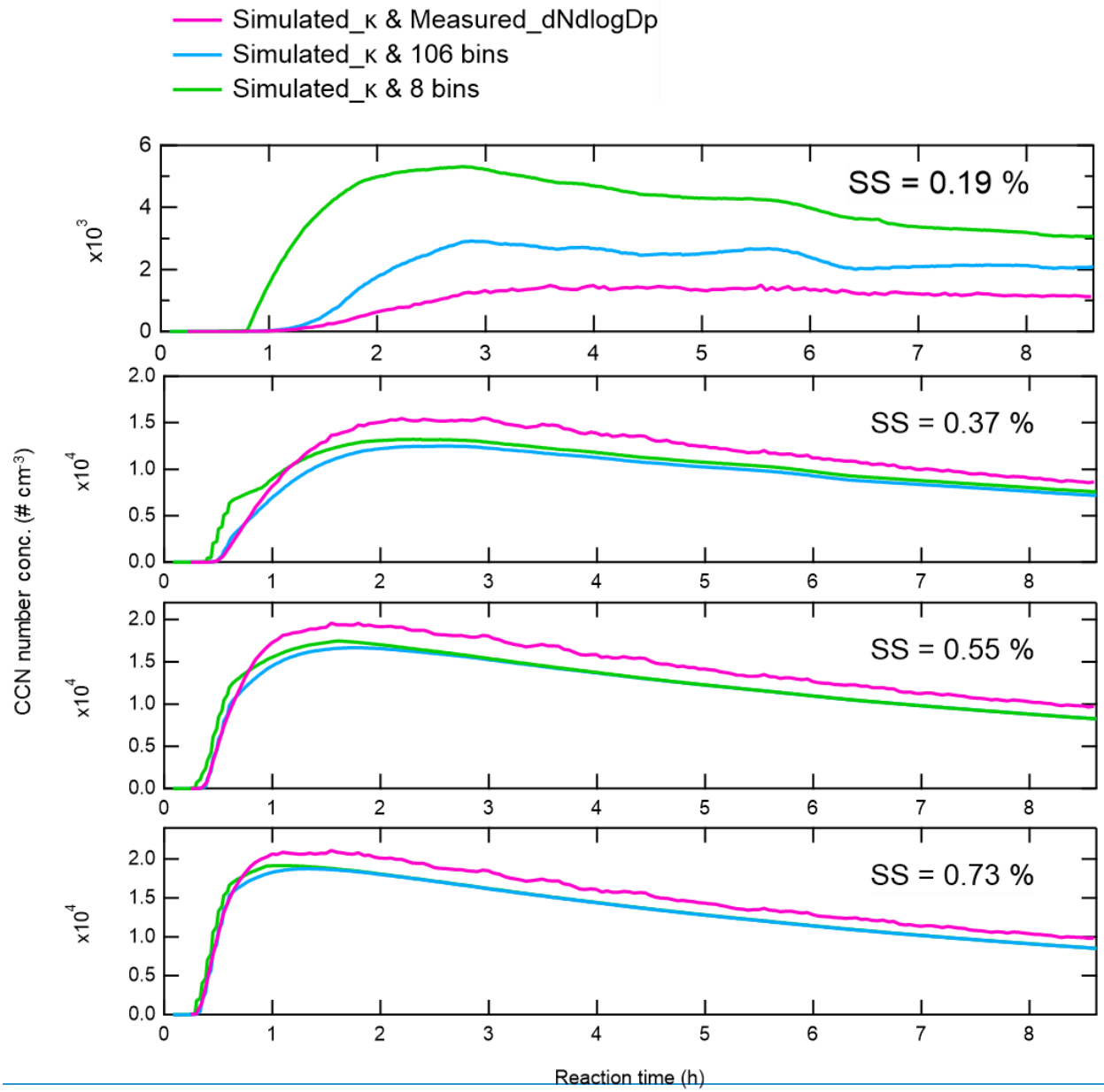
Simulated_κ & Measured_dNdlogDp
Simulated_κ & 106 bins
Simulated_κ & 8 bins
SS = 0.19 %
SS = 0.37 %
SS = 0.55 %
SS = 0.73 %
x10^3
x10^4
CCN number conc. (# cm^-3)
Reaction time (h)

~~Figure S12: (a-d) The~~

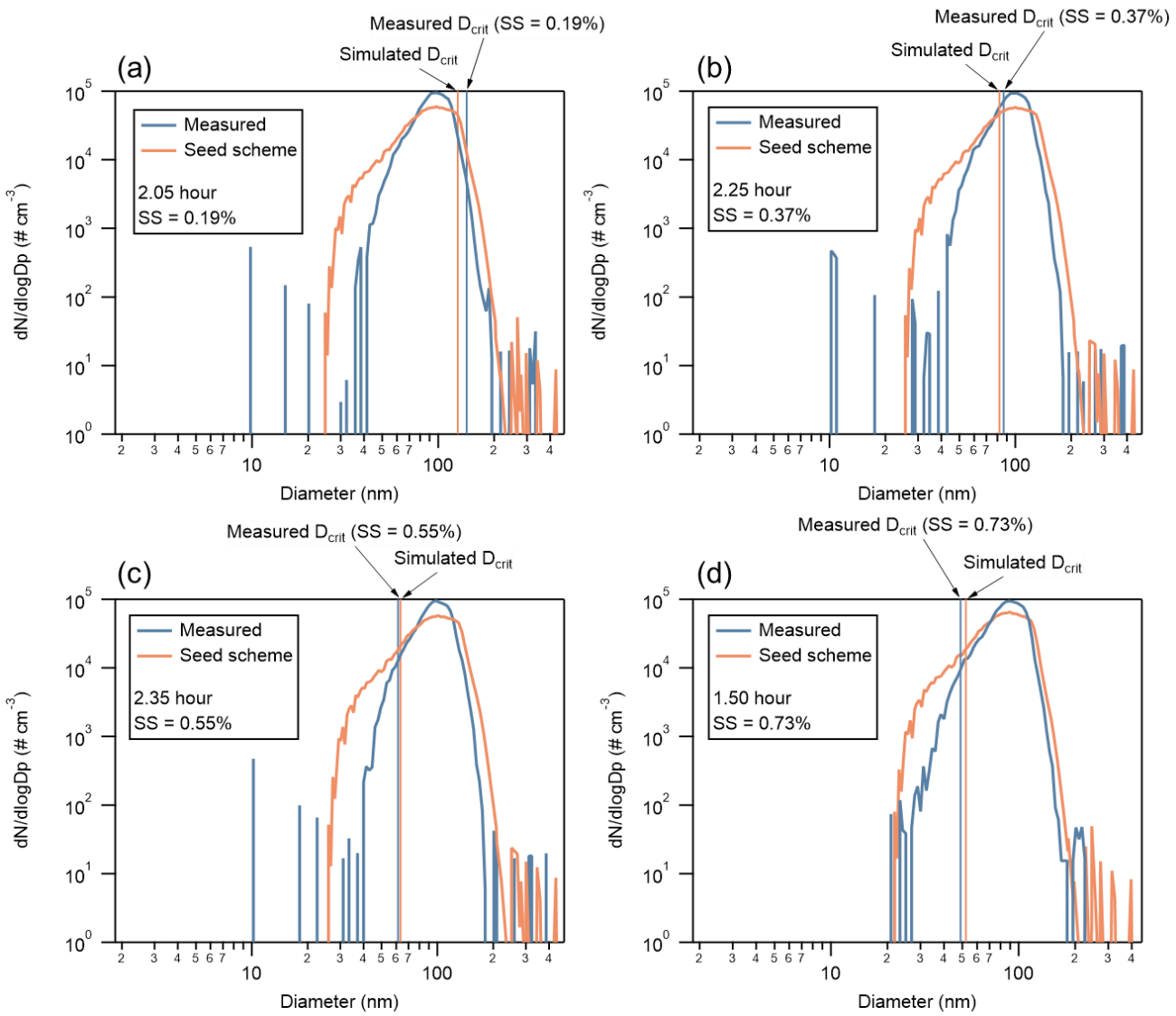

Figure S18: (a-d) Measured PSD and D_{crit}, together with those simulated using the seed scheme, at four SS corresponding to time points before and after 2 h.

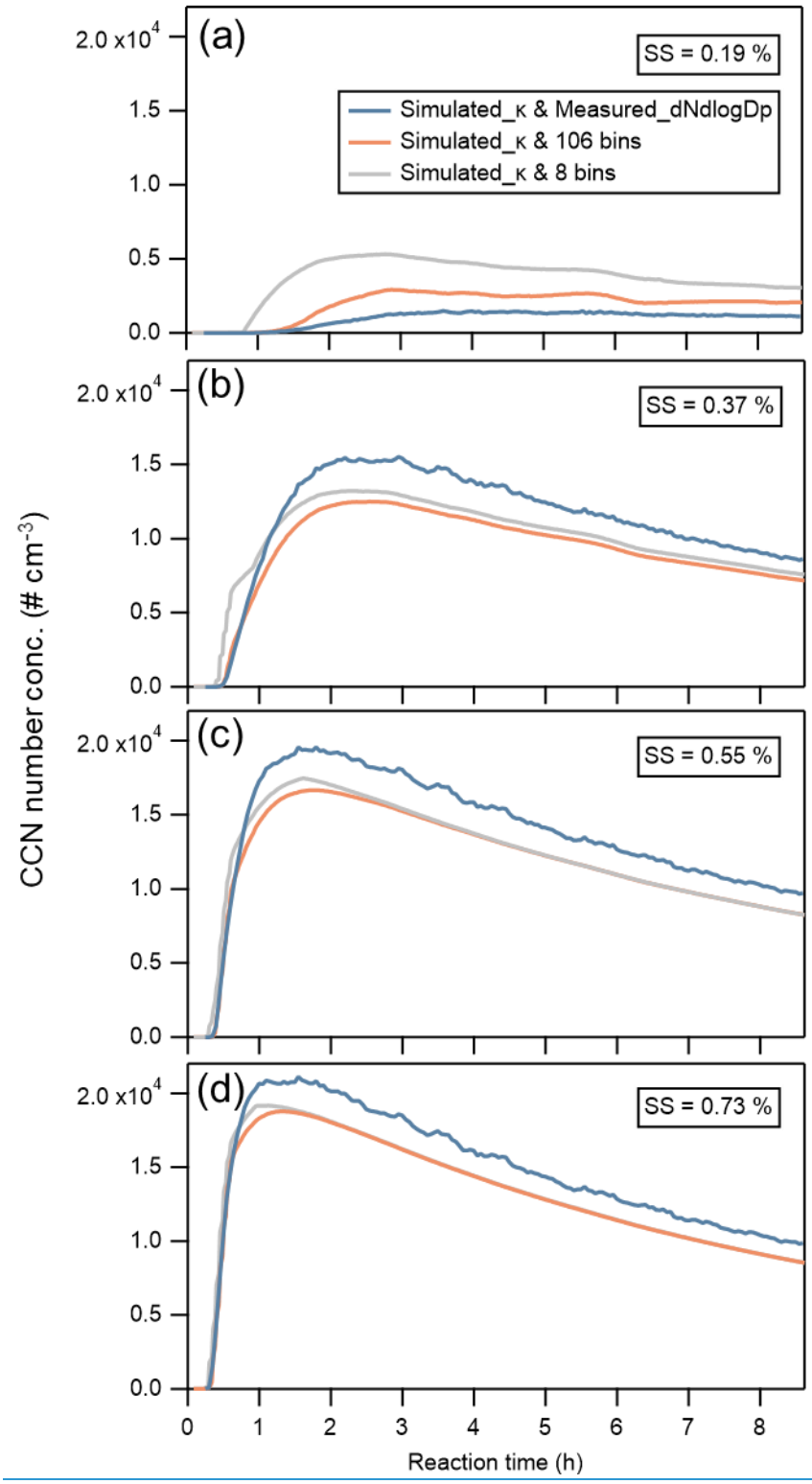

Figure S19: (a-d) CCN number concentrations (# cm^{-3}) at different SS ~~based on simulated~~, calculated using κ simulated by UManSysProp and three ~~kinds~~types of ~~particle~~ number ~~size distributions, including measurement (purple line), and simulation of 106 (blue line) and 8 (green line) size bins~~PSDs: the measured PSD, and simulated PSD using the 106-bin and 8-bin size-resolution settings.

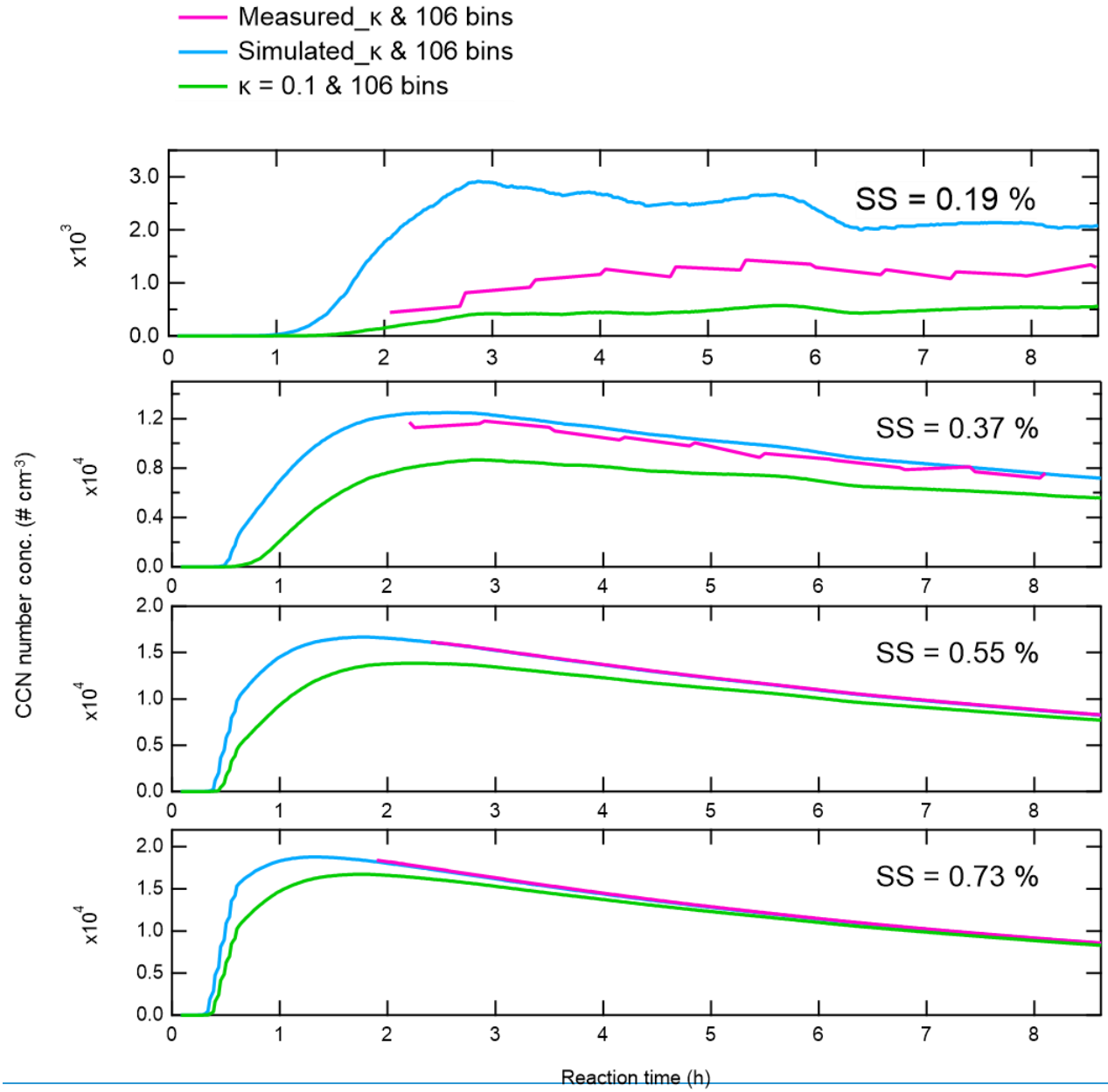
Measured_κ & 106 bins
Simulated_κ & 106 bins
κ = 0.1 & 106 bins
SS = 0.19 %
SS = 0.37 %
SS = 0.55 %
SS = 0.73 %
x10^3
x10^4
CCN number conc. (# cm^-3)
Reaction time (h)

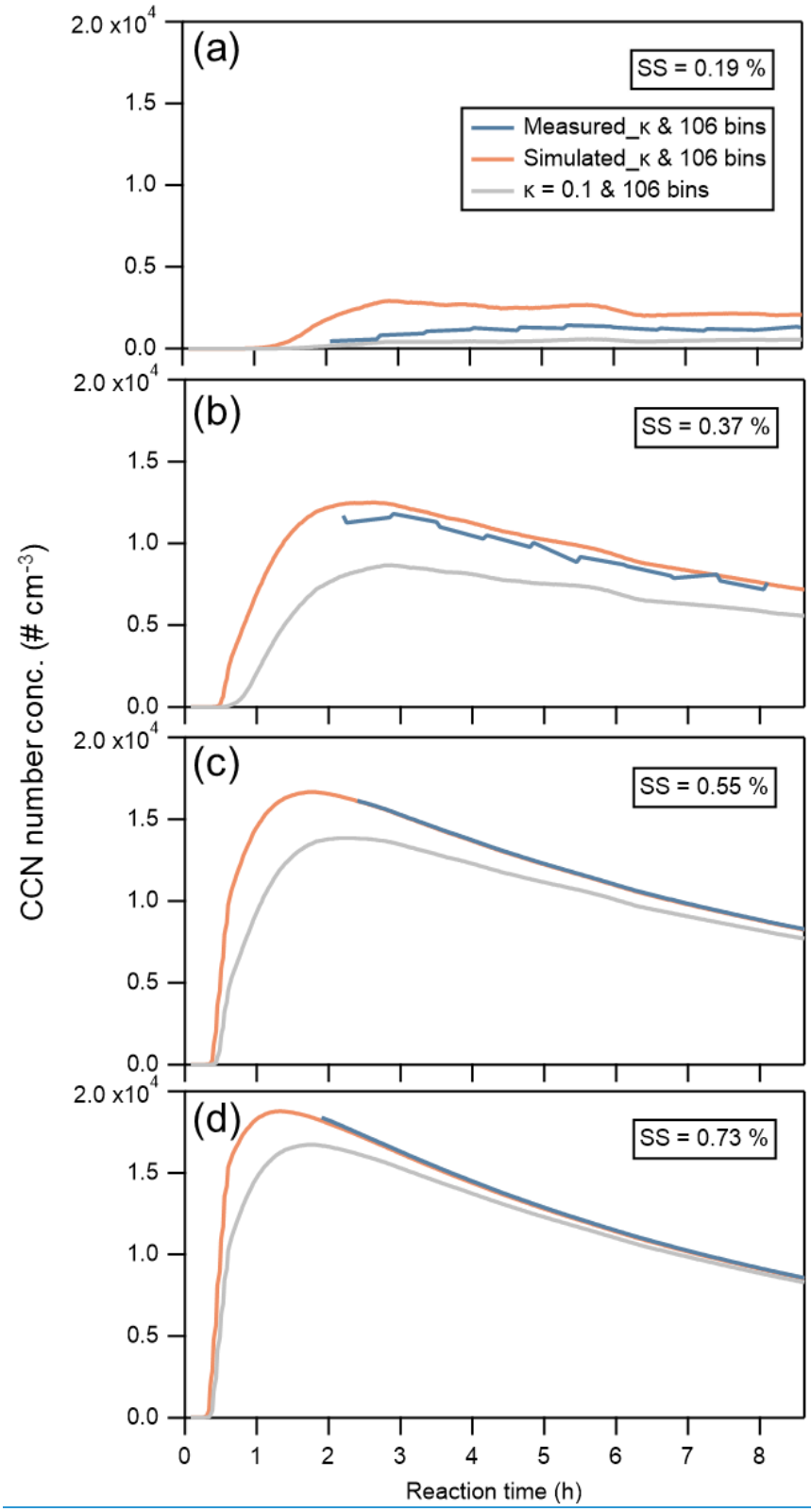

110 **Figure ~~S13~~S20: (a-d) ~~The~~ CCN number concentrations (# cm^{-3}) at different SS ~~based on~~, calculated using the simulated ~~particle number size distribution of~~PSD with 106 size bins ~~setting~~ and three ~~kinds of~~ κ~~, including measurement (purple line), calculation of~~ representations: measured κ, κ calculated using UManSysProp ~~(blue line),~~ and a fixed κ value ~~(~~of 0.1~~) (green line).~~**

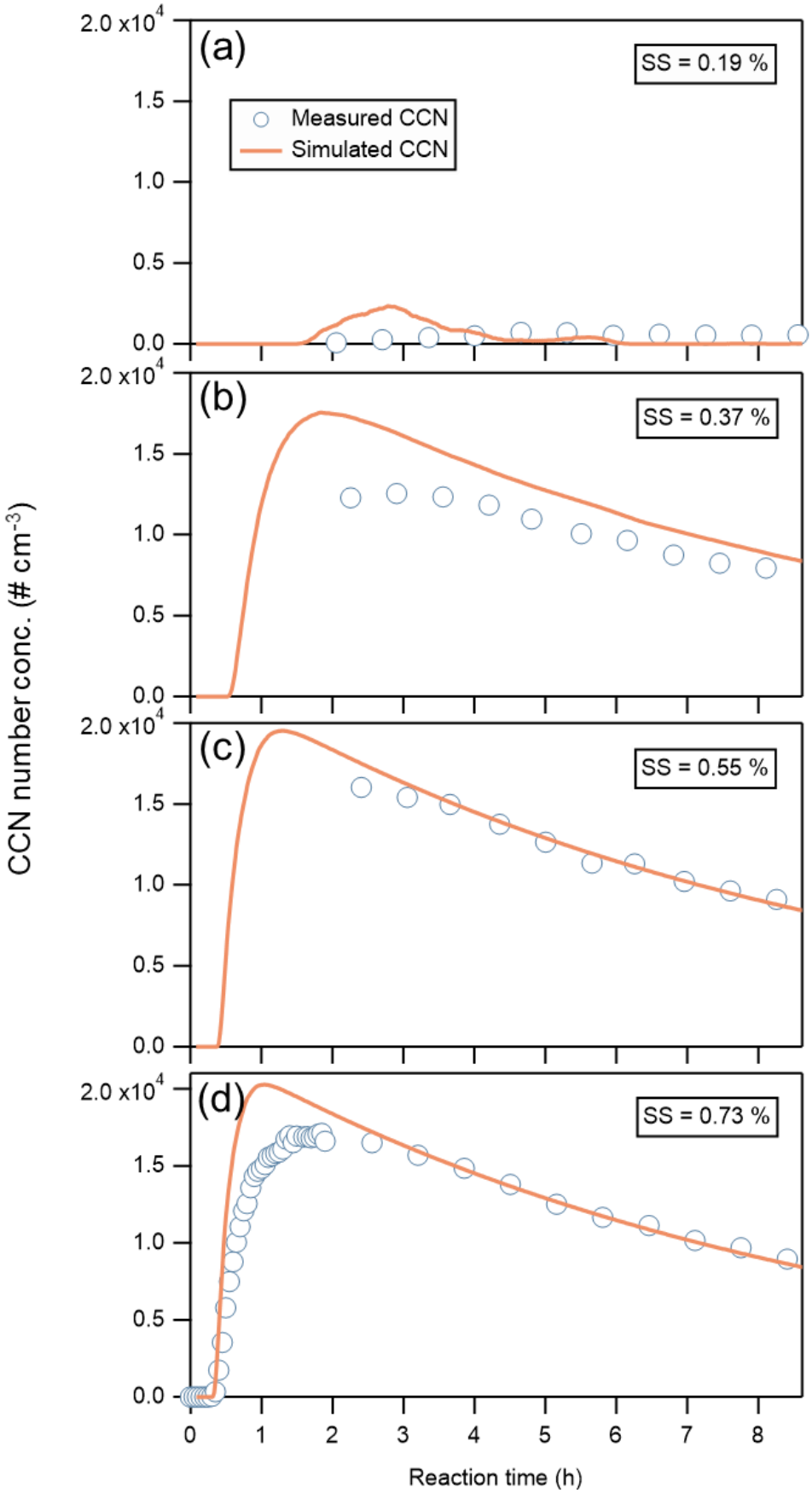

Fig. S21: (a-d) Measured CCN number concentrations (circles; # cm^{-3}) and simulated CCN (lines) using κ and PSD from nucleation scheme.

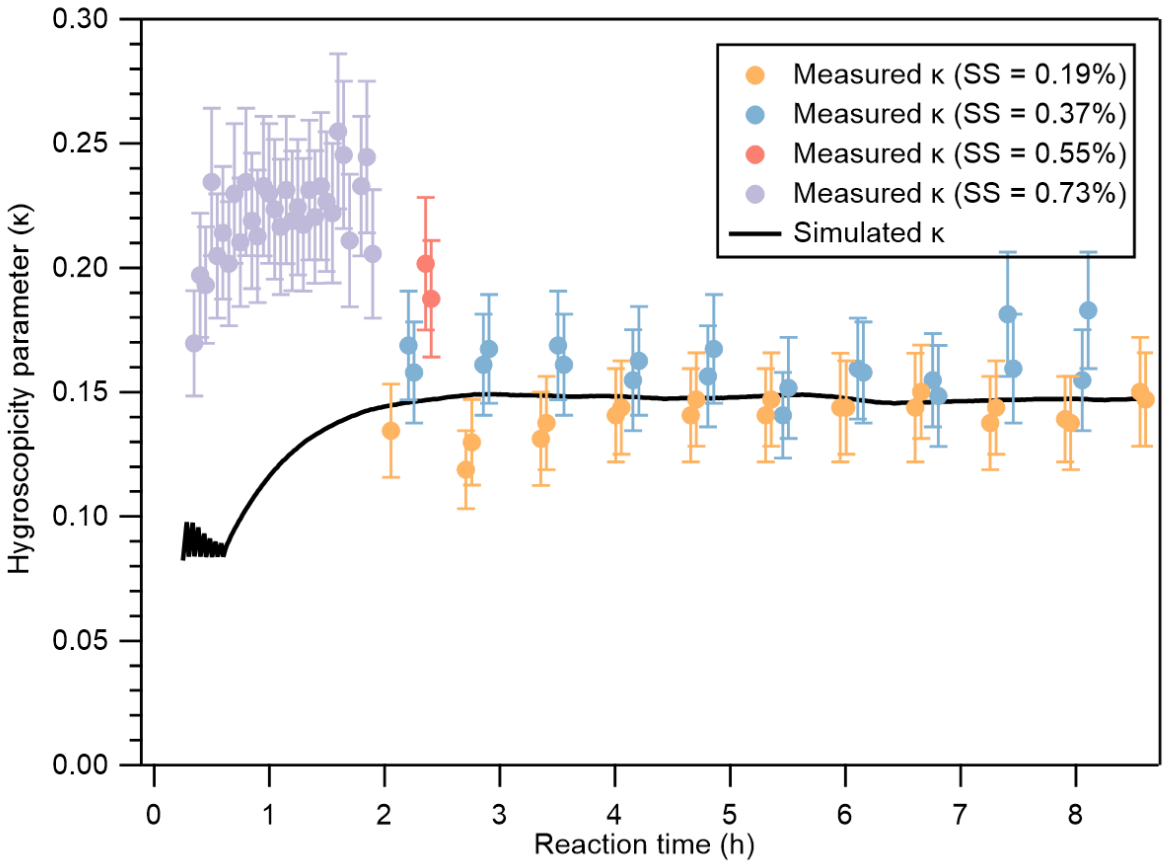

Fig. S22: Hygroscopicity parameter (κ) of simulated SOA using the seed scheme (line) and measured SOA (solid circles with standard-deviation error bars) at different supersaturation (SS).

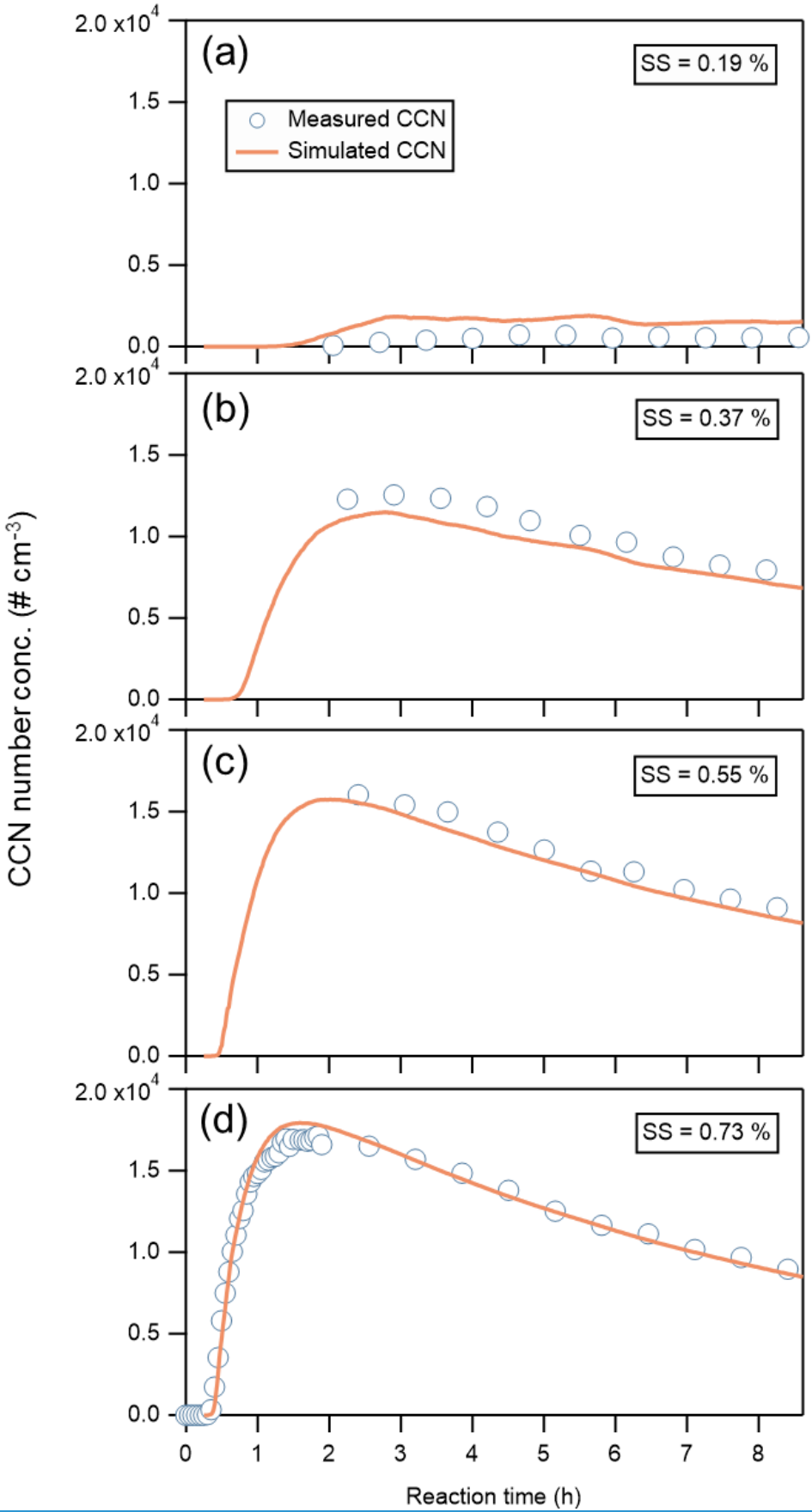

Fig. S23: (a-d) Same as Fig. S21, but for CCN simulated by κ and PSD from the seed scheme.

Table S1: The chemical formulas of all organic species, including HOMs, formed during dark α-pinene ozonolysis.

Chemical species in MCM and PRAM			
CH3O2	C9PAN2	C721PAN	C18H26O4
CH3O	C85CO3H	C721CO3H	C88O2
CH3NO3	C85OOH	NORPINIC	C718CO3
HCHO	C86OOH	C721OOH	C87O2
CH3O2NO2	C511OOH	C722OOH	NC826O2
CH3OOH	C7PAN3	C44OOH	C18H27O6NO3
CH3OH	C235C6CO3H	C811NO3	C20H30O8
CO23C4CHO	CO235C6OOH	C516O	C20H31O6NO3
BIACETO2	APINBO	C516OOH	C19H28O9
CH3CO3	APINBNO3	C10H15O2O2	C19H29O6NO3
HCOCH2CO3	APINBOOH	LIMOOA	C18H26O9
CO23C4CO3	APINBCO	LIMALAO2	C18H27O7NO3
C5PAN9	NAPINAO2	LIMALBO2	C20H30O9
CO23C4CO3H	NAPINBO2	C10H17O3O2	C20H31O7NO3
CO23C3CHO	NAPINAO	BPINENE	C19H28O10
HCOCH2CHO	NAPINAOOH	LIMONENE	C19H29O7NO3
HCOCH2O2	NAPINBO	CARENE	C18H26O10
C3PAN2	NC101CO	C10H15O4O2	C18H27O8NO3
HCOCH2CO3H	NAPINBOOH	C10H15O3O2	C20H30O10
HCOCH2CO2H	NC101O2	C10H15O5O2	C20H31O8NO3
GLYOX	NC101O	C10H15O6O2	C19H28O11
BIACETO	NC102O2	C10H15O7O2	C19H29O8NO3
BIACETOOH	NC102O	C10H15O8O2	C18H26O11
BIACETOH	NC71O2	C10H15O9O2	C18H27O9NO3
HOCH2CO3	NC71O	C10H15O10O2	C20H30O11
HOCH2CHO	NC71CO	C10H15O11O2	C20H31O9NO3
PHAN	NC101OOH	C10H15O12O2	C19H28O12
HOCH2CO3H	NC102OOH	C10H15O2O	C19H29O9NO3
HOCH2CO2H	NC71OOH	C10H15O3O	C18H26O12
ACETOL	NC72O2	C10H15O4O	C18H27O10NO3
MGLYOX	NC72O	C10H15O5O	C20H30O12
CH3COCH2O2	NC61CO3	C10H15O6O	C20H31O10NO3
CH3COCH2O	NC72OOH	C10H15O7O	C19H28O13
HCOCO	NC6PAN1	C10H15O8O	C19H29O10NO3
HCOCO3	NC61CO3H	C10H15O9O	C18H26O13
HCOCO3H	APINCO	C10H15O10O	C18H27O11NO3
HCOCO2H	APINCNO3	C10H15O11O	C20H30O13
HMVKAO2	C720O2	C10H15O12O	C20H31O11NO3
HMVKAO	APINCOOH	C10H14O3	C19H28O14

HMVKANO3	APINCOH	C10H14O4	C19H29O11NO3
HMVKAOOH	HCC7CO	C10H14O5	C18H26O14
HO12CO3C4	C720O	C10H14O6	C18H27O12NO3
CO2H3CHO	C720NO3	C10H14O7	C20H30O14
CO2H3CO3	C720OOH	C10H14O8	C20H31O12NO3
C4PAN6	C720OH	C10H14O9	C19H28O15
CO2H3CO3H	C719O2	C10H14O10	C19H29O12NO3
PAN	C719O	C10H14O11	C18H26O15
CH3CO3H	C719NO3	C10H14O12	C18H27O13NO3
CH3CO2H	C719OOH	C10H14O13	C20H30O15
HCOCH2O	C719OH	C10H15O2NO3	C20H31O13NO3
HCOCH2OOH	APINOOA	C10H15O3NO3	C19H28O16
CH3COCH3	APINOOB	C10H15O4NO3	C19H29O13NO3
HYPERACET	C107O2	C10H15O5NO3	C18H26O16
CHOC3COCO3	C109O2	C10H15O6NO3	C18H27O14NO3
CHOC3COO2	C107O	C10H15O7NO3	C20H30O16
CHOC3COO	C108O2	C10H15O8NO3	C20H31O14NO3
CHOC3COPAN	C108O	C10H15O9NO3	C19H28O17
CHOC3COOOH	C108NO3	C10H15O10NO3	C19H29O14NO3
C413COOOH	C717O2	C10H15O11NO3	C18H26O17
C4CODIAL	C717O	C10H15O12NO3	C18H27O15NO3
C312COCO3	C717NO3	C10H16O4iso1	C20H30O17
CHOCOCH2O2	C107OOH	C10H16O5iso1	C20H31O15NO3
CHOCOCH2O	C107OH	C10H16O6iso1	C19H28O18
C312COPAN	C108OOH	C10H16O7iso1	C19H29O15NO3
C312COCO3H	C108OH	C10H16O8iso1	C18H26O18
ALCOCH2OOH	C717OOH	C10H16O9iso1	C18H27O16NO3
C33CO	C717OH	C10H16O10	C10H16O3
H1CO23CHO	C109O	C10H16O11	C10H17O5O2
APINENE	C89CO3	C10H16O12	C10H17O4O2
APINAO2	C920CO3	C10H16O13	C10H17O6O2
APINBO2	C109OOH	C10H16O14	C10H17O7O2
APINCO2	C109OH	C20H30O5	C10H17O8O2
APINAO	C109CO	C20H30O6	C10H17O3O
APINANO3	C920O2	C20H30O7	C10H17O4O
PINAL	C920O	C923CO3	C10H17O5O
APINAOOH	C921O2	LIMAO2	C10H17O6O
APINBOH	C921O	LIMCO2	C10H17O7O
C96O2	C922O2	LIMALO2	C10H16O4iso2
C96CO3	C922O	LIMBO2	C10H16O5iso2
PINALO2	C621O2	C20H31O4NO3	C10H16O6iso2
C96O	C621O	BPINAO2	C10H16O7iso2

C96NO3	H1C23C4CHO	BPINBO2	C10H16O8iso2
C97O2	H1C23C4O2	BPINCO2	C10H16O9iso2
C97O	H1C23C4CO3	C918CO3	C10H17O3NO3
C98O2	H1C23C4O	C20H31O5NO3	C10H17O4NO3
C98O	H1C23C4PAN	NLIMO2	C10H17O5NO3
C98NO3	HC23C4CO3H	NLIMALO2	C10H17O6NO3
C614O2	H1C23C4OOH	NC91CO3	C10H17O7NO3
C614O	C920PAN	NBPINAO2	C10H17O8NO3
C614NO3	C920CO3H	NBPINBO2	C10H18O5
PINALO	HOPINONIC	C19H28O5	C10H18O6
PINALNO3	C920OOH	C19H28O6	C10H18O7
C106O2	C921OOH	C19H28O7	C10H18O8
C106O	C922OOH	C19H28O8	C10H18O9
C106NO3	C621OOH	C923O2	C10H18O10
C716O2	APINBOO	C924O2	C20H34O6
C716O	C89CO2	C816CO3	C20H34O7
CO13C4CHO	C89O2	NORLIMO2	C20H34O8
C10PAN2	C89O	LMKAO2	C20H35O5NO3
PERPINONIC	C89NO3	LMKBO2	C20H35O6NO3
PINONIC	C810O2	C926O2	C19H32O6
C96OOH	C810O	C817CO3	C19H32O7
C96OH	C810NO3	LMLKAO2	C19H32O8
NORPINAL	C514O2	LMLKBO2	C19H32O9
C97OOH	C514O	C823CO3	C19H33O6NO3
C97OH	C514NO3	C925O2	C18H30O6
C98OOH	C89PAN	NOPINAO2	C18H30O7
C98OH	C89CO3H	NOPINBO2	C18H30O8
C614OOH	C89CO2H	NOPINCO2	C18H30O9
C614OH	C89OOH	NOPINDO2	C18H30O5
C614CO	C89OH	C918O2	C18H31O7NO3
PINALOOH	C810OOH	C9DCO2	C20H34O9
PINALOH	C810OH	C915O2	C20H35O7NO3
C106OOH	C514OOH	C917O2	C19H32O10
C106OH	C514OH	C919O2	C19H33O7NO3
C716OOH	C811CO3	C914O2	C18H30O10
C716OH	C811O2	C916O2	C18H31O8NO3
CO235C6CHO	C811O	C88CO3	C20H34O10
H3C25C6O2	C812O2	C87CO3	C20H35O8NO3
H3C25C6CO3	C812O	C822CO3	C19H32O11
H3C25C6O	C813O2	NLMKAO2	C19H33O8NO3
H3C2C4CO3	C813O	C19H29O5NO3	C18H30O11
H3C2C4PAN	C813NO3	C18H26O5	C18H31O9NO3

H3C2C4CO3H	C516O2	C18H26O6	C20H34O11
H3C2C4CO2H	C811CO3H	C18H26O7	C20H35O9NO3
H3C25C6PAN	PINIC	C729CO3	C19H32O12
H3C25C5CHO	C811PAN	C816O2	C19H33O9NO3
H3C25CCO3H	C811OOH	C817O2	C18H30O12
H3C25CCO2H	C811OH	C826O2	C18H31O10NO3
H3C25C6OOH	C721CHO	C822O2	C20H34O12
H3C25C6OH	C812OOH	C818O2	C20H35O10NO3
C85O2	C812OH	C823O2	C19H32O13
C85CO3	C813OOH	C819O2	C19H33O10NO3
C85O	C813OH	C727CO3	C18H30O13
C86O2	CO13C3CO2H	C731CO3	C18H31O11NO3
C86O	C721O2	C824O2	C20H34O13
C511O2	C721CO3	C820O2	C20H35O11NO3
C511O	C721O	C18H26O8	C19H32O14
CO235C5CHO	C722O2	C825O2	C19H33O11NO3
CO235C6CO3	C722O	C821O2	C18H30O14
CO235C6O2	C44O2	C732CO3	C18H31O12NO3
CO235C6O	C44O	C8BCO2	C10H18O4

Table S2: Simulated hygroscopicity parameter (κ) of SOA calculated from different chemical compositions and the corresponding particle sizes (nm).

Particle size (nm)	κ
50.6	0.179
63.0	0.178
84.8	0.177